

POLITECNICO DI MILANO

Facoltà di Ingegneria Industriale

Corso di Laurea in
Ingegneria Energetica



Best aiming strategy definition for off-design conditions due to passage of
clouds in a Solar Tower

Relatore: Prof. Giampaolo MANZOLINI

Co-relatore: Prof. David SÁNCHEZ
(*Universidad de Sevilla*)

Tesi di Laurea di:

Francesco CRESPI
Paolo ZANI

Matr. 783167
Matr. 801811

Anno Accademico 2013 – 2014

Ringraziamenti

Innanzitutto desideriamo ringraziare il nostro relatore, il professor Giampaolo Manzolini, per la disponibilità dimostrataci durante questo progetto e per la capacità di stimolarci continuamente con nuovi spunti di riflessione.

En segundo lugar, queremos dar las gracias al profesor David Sánchez por todas las preciosas indicaciones y sugerencias, por su amabilidad, hospitalidad y su continua contribución al desarrollo de nuestro proyecto.

Gracias también a Benjamín, Jose María, Mario y a todo el Grupo de Máquinas y Motores Térmicos de Sevilla por la ayuda y el apoyo constante, tanto en el tiempo compartido en la oficina cuanto en los inolvidables almuerzos en la mejor Tasca del mundo, obviamente situada en Utrera!

Un enorme ringraziamento va alle nostre famiglie, per il sostegno offertoci in tutti questi lunghi anni di Università, in special modo per averci appoggiato sempre e comunque in tutte le scelte della nostra vita, passata e futura.

Ringraziamo vivamente anche tutti i compagni di avventure di sempre, sempre pronti al nostro fianco, e agli amici del Poli, con cui abbiamo condiviso i nostri anni di studio.

Por último, pero no menos importante, queremos dar un enorme abrazo a todos los nuevos amigos (Sevillanos y no): María, Juan, Mariño, Jesus, Paolo, Francesco, Armenta, Josefina, Isa, Camille, Dana, Carlo, Farola, Vito, Reyes, la chicca, Misael, Batano, Elio, GECAJP, el Puma, el tanguillo de Cádiz y todos los que nos estamos olvidando sin querer!

Boniti, belli tutti!

Riassunto

Lo scopo del presente elaborato è effettuare un'analisi delle prestazioni di due impianti solari a ricevitore centrale a torre in condizioni di funzionamento off-design. Nella fattispecie, sono stati scelti gli impianti PS10 e Gemasolar, entrambi situati nelle vicinanze di Siviglia. Il primo è caratterizzato da un campo solare di tipo north-field, con ricevitore a cavità, ed entrò in funzione nel 2007 (primo impianto commerciale al mondo) erogando una potenza di 10 MW_{el}. Il secondo invece presenta un campo solare di tipo surrounding-field, un ricevitore esterno cilindrico ed una potenza elettrica di 19.9 MW_{el}. Questi due impianti, inoltre, differiscono per un altro sostanziale elemento: nella PS10 il fluido di lavoro è costituito da acqua, che esce dal ricevitore in condizioni di vapore saturo e viene in seguito espanso in una turbina; nella Gemasolar, invece, un fluido di lavoro composto da sali fusi permette il funzionamento quasi continuo dell'impianto. La presenza di un sistema di accumulo termico permette la produzione di vapore tramite uno scambiatore di calore intermedio e garantisce una autonomia di funzionamento di circa 15 ore in assenza di radiazione solare.

In particolare, due elementi sono stati presi in considerazione in questo studio: il campo solare ed il ricevitore. Analizzando le prestazioni ottiche degli eliostati sottoposti ad una radiazione solare variabile a causa del passaggio di nuvole, si possono determinare delle mappe di flusso termico incidente sulla superficie del ricevitore stesso. Quest'ultimo è uno degli elementi più critici dell'impianto, a causa del grande carico termico a cui è soggetto. Durante i transitori presi in considerazione il flusso termico incidente cambia sensibilmente, causando repentine variazioni del gradiente di temperatura che possono portare ad elevati stress termici nel ricevitore.

Il presente lavoro di tesi è partito con l'utilizzo di un codice Matlab, precedentemente scritto da un altro laureando del Politecnico di Milano, che permette di studiare le prestazioni degli impianti in questione in condizioni di progetto. A tal scopo era stato scelto Delsol3, un software sviluppato da SANDIA National Laboratories in grado di simulare le performance di impianti solari a torre. La finalità di questa tesi era di individuare una strategia di puntamento in grado di diminuire i picchi di flusso termico incidente, senza ridurre la potenza complessivamente incidente. Lo scopo finale consisteva in una riduzione dei costi globali dell'impianto, una delle sfide più ambiziose di questa tecnologia. Mantenendone la struttura generale, questo codice è stato ampliato e diverse nuove funzionalità sono state aggiunte per poter raggiungere l'obiettivo preposto all'inizio del presente percorso di tesi. La idea principale di questo studio è infatti quella di trovare la strategia di puntamento che meglio possa affrontare i problemi creati dal passaggio di nuvole sul campo solare, verificando se quest'ultima risulti essere uguale a quella proposta per le condizioni nominali di funzionamento. Inoltre, con lo scopo di valutare gli stress termici effettivamente prodotti nel ricevitore, un ulteriore codice Matlab è stato sviluppato, per modellare lo scambio termico nella PS10 ed ottenere il profilo di temperatura della superficie esterna del ricevitore.

La prima tappa di questo percorso è quindi stata uno studio preliminare sulle condizioni meteorologiche che contraddistinguono l'area di Siviglia, per poter identificare le avverse condizioni che potrebbero interessare gli impianti in questione. Per prima cosa, è stato

individuato il tipo di nuvola che con maggiore probabilità potrebbe essere causa di rapide variazioni della DNI. Per questo scopo è stata selezionata la *cumulus humilis*, detta anche “nuvola del bel tempo”. Quest’ultima presenta dimensioni molto variabili (può coprire totalmente o solo in piccola parte i campi solari considerati) e porta a cambi di radiazione solare incidente molto netti e bruschi. Per quanto riguarda invece il vento, degli studi sulla direzione e sulla intensità media nella provincia di Siviglia portano ad individuare valori tipici, considerati per modellare il transito delle nuvole. È stato possibile discretizzare temporalmente il passaggio delle nubi in diversi istanti temporali, 10 per PS10 e 20 per Gemasolar: considerando la direzione principale del vento (S-W, 220°) i due campi solari vengono coperti progressivamente considerando istanti temporali successivi. Il numero di istanti, è frutto del compromesso tra discretizzazione spaziale, temporale e onere computazionale del programma. In seguito a queste ossevizioni, un insieme di sei nuvole è stato preso in considerazione e modellato per ogni impianto. In entrambi casi si è deciso di simulare una copertura sia parziale che totale del campo. Diverse zone sono state oscurate separatamente, per valutare se la condizione più problematica sia data solo dalla quantità di eliostati oscurati, indipendentemente dalla loro ubicazione, oppure se quest’ultima e quindi la efficienza ottica degli stessi influisca fortemente sul risultato.

In seguito sono state analizzate varie strategie di puntamento proposte in studi precedenti, con lo scopo di individuare quella che riduce il flusso termico incidente e del gradiente di quest’ultimo. Partendo da una strategia di base in cui tutti gli eliostati puntano al centro del ricevitore (minimizzando così le perdite di “spillage” dovute alla mancata intercettazione della radiazione da parte del ricevitore stesso), queste alternative cercavano di distribuire più omogeneamente il flusso termico incidente. Sei delle migliori strategie proposte sono state utilizzate nel presente elaborato per verificare quale fra queste potesse far fronte alle condizioni imposte dal transito delle nuvole. Per poter definire le suddette strategie, nel presente lavoro il campo solare della PS10 è stato suddiviso in 64 zone (seguendo una divisione radiale-azimutale 8x8), mentre quello della Gemasolar in 128 zone (8x16). Il motivo di questa differenza risiede nelle diverse dimensioni del campo solare e nel diverso numero di istanti temporali: la discretizzazione spaziale del campo della Gemasolar, molto più grande di quello della PS10, dovrà infatti essere più fitta. Un totale di 20 istanti temporali assicurano una ottima qualità della simulazione, non incidendo eccessivamente sul costo computazionale. Una volta fatta la divisione in zone, si è provveduto a definire nove punti di fuoco, disposti sulla superficie del ricevitore seguendo un pattern rettangolare. La superficie del ricevitore della PS10 è stata divisa in quattro pannelli, seguendo la vera configurazione fisica dell’impianto, mentre quella di Gemasolar in tre, per meglio analizzare la superficie cilindrica di quest’ultimo. Attraverso il programma, è stato possibile associare ad ogni zona un corrispettivo punto, in maniera tale che tutti gli eliostati appartenenti a quella zona puntassero esattamente in quella porzione di ricevitore, riuscendo a ridistribuire il flusso incidente. Questa caratteristica del programma può rivelarsi estremamente utile, in quanto consente all’utente esterno di editare nuove strategie di puntamento o di modificare quelle già esistenti, permettendo una più profonda comprensione del funzionamento dell’impianto.

Una volta eseguita una simulazione (per l’impianto, la strategia di puntamento e il tipo di nuvola scelti) il programma produce una serie di risultati, tanto grafici quanto numerici, per ogni istante temporale. In primis, è fornita la mappa di flusso termico del ricevitore, rappresentata attraverso un grafico *surf* (3-D) e *contourf* (2-D), assieme alla mappa del gradiente del flusso termico. Queste mappe forniscono preziose indicazioni sul profilo del

flusso incidente e permettono un primo approccio visuale al problema. In secondo luogo, le prestazioni del campo solare vengono mostrate attraverso due tipi di grafici: nel primo vengono rappresentati tutti gli eliostati, assegnando un colore dal blu al rosso in funzione del loro rendimento ottico; nel secondo, viene mostrata la divisione in zone del campo, ed ogni zona presenta un colore in funzione della quantità di flusso termico inviato al ricevitore, calcolata come la somma dei contributi di ogni singolo eliostato. Il primo grafico risulta essere di grande importanza per l'analisi dei due impianti, in quanto fornisce un elevato numero di informazioni sulle perdite ottiche presentate da ogni eliostato, in diversi momenti del giorno e dell'anno. Nella fattispecie, possono essere facilmente individuati e rappresentati i contributi dell'effetto coseno, le perdite di ombreggiamento e bloccaggio, di "spillage" e quelle dovute alla interazione tra la radiazione diretta al ricevitore e l'atmosfera. Inoltre, il secondo grafico consente di individuare l'eventuale presenza nel campo solare di fasce a rendimento maggiore: ciò risulta particolarmente utile per valutare quale sia la situazione di oscuramento più problematica. Tutte queste rappresentazioni mostrano qualitativamente le prestazioni del campo e possono essere utilizzate quindi come strumenti ausiliari nell'analisi oggetto del presente elaborato. Tuttavia, per poter effettuare uno studio quantitativo, risulta necessario un approccio numerico. Per questo motivo, sono state scelte tre variabili di interesse, in grado di fornire una prima rappresentazione delle prestazioni e dei possibili stress sofferti dal ricevitore: i valori picco, la variazione temporale istante per istante e il massimo gradiente del flusso termico. Inoltre, per non perdere di significato fisico, si è provveduto ad analizzare le suddette variabili per ogni pannello. Di conseguenza, i valori dei parametri presi in considerazione vengono calcolati per ogni istante temporale e per ogni pannello e per poter analizzare la grande mole di dati numerici ottenuti, una serie di grafici vengono prodotti in *excel*.

Pertanto, per ogni impianto tutte le possibili combinazioni tra strategie di puntamento e nuvole sono state analizzate, in maniera tale da poter individuare la condizione off-design più estrema e la migliore strategia in grado di affrontarla. I risultati ottenuti da questo primo studio ottico mostrano come la strategia di puntamento che si era rivelata essere la migliore in condizioni nominali (studi precedenti), continui ad essere la migliore anche per condizioni off-design. Quest'ultima infatti, paragonata con le altre cinque, può portare ad una riduzione del flusso picco dell'ordine del 14÷33%, del gradiente massimo del flusso termico del 13÷19% e della variazione temporale del medesimo del 8.5÷28%. Per quanto riguarda invece la condizione meteorologica più avversa, una nuvola grande in grado di coprire interamente il campo risulta essere la più problematica per entrambi gli impianti. Un altro risultato molto rilevante è ottenuto analizzando le nuvole che coprono solo parzialmente il campo solare: si può osservare come delle nuvole in grado di oscurare interamente solo una metà del campo in alcuni casi portino a risultati prossimi a quelli ottenuti con nuvole di dimensioni decisamente inferiori che transitano sopra le zone di maggiore efficienza. Ciò risponde al quesito posto all'inizio dello studio, e si può affermare che in un oscuramento parziale il parametro di maggiore rilevanza non è solo la dimensione della nuvola, ma bensì la zona da essa oscurata.

Nella seconda parte del lavoro, le mappe di flusso precedentemente ottenute sono state utilizzate come input per il modello semplificato del ricevitore della PS10, che permette di studiare lo scambio termico in questo elemento in condizioni statiche (non prende in considerazione effetti dinamici). Come prima cosa è stata ipotizzata una geometria di questo componente, scegliendo un layout con tubi verticali. Si è supposto per semplicità

che l'acqua entri nel ricevitore in condizioni di liquido saturo alla temperatura e alla pressione imposte dal separatore di vapore (250 °C, 40 bar) e con una portata massica uguale per ogni tubo, scelta in maniera da ottenere un titolo di vapore finale di 0.2 (all'entrata del separatore). Inoltre, vengono trascurate le perdite di carica nei downcomers e uprisers. Il secondo passo è stato quello di dividere la superficie del ricevitore in diversi elementi, in seguito chiamati *unità di flusso*. Questa divisione è stata fatta in modo tale che ad ogni unità di flusso corrispondesse un valore costante di flusso termico incidente, seguendo la discretizzazione spaziale imposta dai risultati di Delsol3. Per ogni unità di flusso è stato impostato un bilancio termico globale. La potenza termica proveniente dal campo (q_{field}) supera la superficie esterna del ricevitore e viene diviso nei tubi corrispondenti (q_{trans}), dopo aver dissipato parte dell'energia nelle seguenti perdite termiche:

- *perdita per irraggiamento* verso l'ambiente esterno, in parte verso la volta celeste e in parte verso terra ($q_{lossrad}$). Per calcolare questo contributo si utilizza la legge di Stefan-Boltzmann, considerando una $T_{sky-ground}$ media, una emissività di 0.4 e valori diversi per i fattori di vista dei pannelli più interni e più esterni del ricevitore (rispettivamente 0.45 e 0.3);
- *perdita per convezione* ($q_{lossconv}$), dovuta alla formazione di fenomeni di convezione naturale tra la superficie del ricevitore e l'aria contenuta nella cavità di quest'ultimo. E' stato deciso di considerare convezione naturale e non convezione forzata per via della configurazione della torre solare: l'apertura del ricevitore è diretta verso nord, mentre la direzione preferenziale da cui proviene il vento è sud-ovest, quindi il contributo di quest'ultimo sarà minimo. Per calcolare questa perdita il modello utilizza la correlazione di Churchill & Chu;
- *perdita per riflessione* ($q_{lossrefl}$), dovuta alle caratteristiche ottiche della superficie del ricevitore. Viene utilizzato un valore della riflettanza di 0.02;
- si è deciso di trascurare le perdite di conduzione, convezione ed irraggiamento verso l'interno della torre solare perché notevolmente più basse delle precedenti.

Il bilancio termico globale di una singola unità di flusso risulta quindi essere:

$$q_{trans} = q_{field} - q_{lossrad} - q_{lossconv} - q_{lossrefl}$$

Una volta calcolata la potenza termica effettivamente trasmessa ad ogni tubo è quindi stato possibile impostare un procedimento iterativo per calcolare la temperatura della superficie del ricevitore. Per fare questo è stato sufficiente considerare la q_{trans} come la potenza termica scambiata tra la superficie esterna e la corrente interna di fluido di lavoro, e tramite questa formula arrivare al valore di $T_{wallExt}$. Come coefficiente globale di scambio termico è stato considerato la somma del contributo conduttivo della parete del tubo e di quello convettivo dell'acqua in transizione di fase. Per il calcolo di quest'ultimo, è stata utilizzata la correlazione di Kandlikar, in condizioni di ebollizione nucleata.

Il modello appena descritto è in grado di produrre un'ampia serie di risultati per ogni istante temporale, sulla falsa riga del primo codice studiato: in primo luogo, la mappa di temperatura dell'intero ricevitore (unità di flusso per unità di flusso) e la rappresentazione del gradiente di temperatura; in secondo luogo, un insieme di dati numerici che permettono lo studio quantitativo delle prestazioni del ricevitore. I parametri presi in considerazione sono i valori picco di temperatura, le sue variazioni temporali istante per istante e il

gradiente della stessa; per semplificare la lettura dei risultati è stata adottata una serie di diagrammi *excel*.

Per prima cosa è stato impostato un controllo incrociato tra strategie di puntamento e i tipi di nuvole, che confermano le conclusioni precedentemente ottenute con lo studio ottico. Considerando una nuvola che oscura interamente il campo solare, si sono determinate le mappe di temperatura del ricevitore con le diverse strategie di puntamento, e viceversa con la migliore strategia ottenuta in precedenza e le sei tipologie di nubi. In conclusione, i risultati dello studio termico verificano le conclusioni ottenute con lo studio ottico. La strategia di puntamento trovata in precedenza è in grado di migliorare la performance termica del ricevitore, riducendo sia i picchi di flusso che i gradienti di temperatura. I risultati ottenuti evidenziano una riduzione dell' 8% dei valori picco della temperatura, del 29% della variazione temporale della temperatura picco e fino a un 35% per il massimo gradiente di quest'ultima. Per quanto riguarda invece le nubi, si può affermare che la nuvola descritta in precedenza porta alle condizioni off-design più problematiche, anche se vengono riscontrate delle piccole deviazioni dagli andamenti medi del gradiente di temperatura. Benché queste irregolarità non abbiano una importanza sufficientemente grande da poter confutare le ipotesi di partenza, una analisi più dettagliata delle stesse, assieme ad uno studio più approfondito sui reali stress termici prodotti, potrebbe risultare utile per comprendere più a fondo le prestazioni ed i rischi corsi dal ricevitore.

Summary

The goal of this project work is to analyze the performance of two commercial solar tower power plants, working in off-design conditions. The considered systems are PS10 and Gemasolar plants, both located in the Seville province. The first one presents a north-field layout, with cavity receiver and was started up in 2007 (first commercial plant in the world), providing 10 MW_{el} of electrical power. The second one is characterized by a surrounding field, an external cylindrical receiver and guarantees 19.9 MW_{el} of electrical power. The main difference between the two plants is the working fluid adopted: in the PS10 the fluid is water, which leaves the receiver in saturated vapor conditions and subsequently is expanded in a turbine; instead, in Gemasolar plant molten salts are used in order to allow a continuous operation of the system. Through a second heat exchanger, a heat storage system guarantees a continuous operation of the plant up to maximum of 15 hours. The only stops are made for maintenance issues or for prolonged bad weather conditions.

Two main elements have been considered in the present study: the solar field and the receiver. Thermal flux maps on the external receiver surface can be obtained by analyzing the optical performance of the heliostats, studying the behavior of the latter when a variable DNI occurs due to passage of clouds. The receiver withstands severe thermal conditions and thus is one of the most critical elements of the plant. In the transient taken into account, the heat thermal flux is highly variable and leads to high temperature gradients variation that could induce high thermal stresses in the receiver.

At the very beginning of this thesis, a Matlab code previously done by a master student of Politecnico di Milano has been analyzed. The latter studied the on-design working conditions of the above mentioned solar plants. For this purpose Delsol3, a software for performance simulation of Solar Power Plant developed by Sandia National Laboratories, was used. The goal of this thesis was to identify a new aiming strategy able to reduce peak fluxes without affecting the output power of the plant. In this way a diminish in the maintenance costs could further reduces the energy price of this brand new technology, that is one of the biggest issues to be solved in order to have an affordable energy cost.

Maintaining the same general structure, it has been developed another code by adding new functionalities in order to achieve the goals of the present work. In fact, the main idea of this thesis is to find the best aiming strategy able to face the issues occurring during the passage of clouds over the solar field and to check if the best strategy used in the on-design working conditions is the same also during a transient. Moreover, another Matlab code modelling the heat exchange process of PS10 plant has been implemented in order to obtain temperature maps of the external surface of the receiver. Hence, the real thermal stress in the receiver can be analyzed.

The first step of this work has been a preliminary study on the weather conditions of the province of Seville in order to understand the possible situation that the studied plants have to withstand. First of all, the clouds type leading to fast alternating DNI has been identified: “cumulus humilis”. These clouds come in a range of sizes, from small popcorn

cumulus to large tropical cloud clusters and are also known as the “clouds of good weather”. They leads to rapid change among blue sky (with a DNI of about 1000 kW/m²) and shadow (DNI = 0) and cause an unstable working operation for the solar tower. A deep study on the main direction and magnitude of the wind in the Seville province has been done and averages values have been used to model the clouds passage. Due to the fact that the clouds passage is not simulate in a continuous way, the simulation provide a temporal subdivision of the entire process in “*time-steps*”; 10 and 20 time-step have been chosen respectively for PS10 and Gemasolar. These different subdivisions have been considered because the wind direction (S-W, 220°) and velocity are the same for the two plants, while the size of Gemasolar is almost the double. When a cloud passes over the field, different sectors are covered at each time-step; this choice has been done to have a good compromise between quality and a computational cost of the simulation. Afterwards, for each plant six clouds have been selected and modeled and both partial and total shadowing of the field have been simulated. In order to understand the most severe conditions, different zones have been shadowed separately. It has been investigated if the amount of shadowed heliostats is the most important parameter or, on the contrary, if also the position and thus the efficiency of the latters does matter.

Subsequently, different aiming strategies proposed in previous studies have been analyzed in order to identify the one that leads to lower values of peak flux and flux gradient. The default aiming strategy used in the plants aims all the heliostats to the central part of the receiver with the purpose to avoid spillage losses. The other options attempt to reduce peak flux by spreading in a more homogeneous way the incident thermal flux.

In order to verify if some of these strategies can deal with the severe condition imposed by the transient, six of them have been chosen. To define these strategies, PS10 solar field has been subdivided in 64 zones (radial-azimuthal division 8x8), while 128 zones (8x16) were chosen for Gemasolar. This distinction is due to the different sizes of the fields and to the different number of time-steps. In fact, a greater spatial discretization of Gemasolar allows an excellent simulation quality without a high increase of the computational costs. After that, nine focusing points on the receiver have been defined; these have a rectangular pattern and are equally spaced. The modeled PS10 receiver surface is composed by four panels, as the real configuration, while the Gemasolar one consists of three panels, in order to better analyze the cylindrical surface of this receiver. By means of the developed code, to each zone of the field has been associated a specific point on the receiver. Hence, all the heliostats belonging to a specific zone have been aimed to a specific area of the receiver, managing to spread the incident flux. The user can edit new strategies or modifying the existent ones, resulting in a better understanding of the plant working conditions. Once selected the plant type, the aiming strategy and the cloud, the code produces a series of numerical results and graphs showing the behavior of the solar field and the receiver. Firstly, by means of *surf* (3-D) and *countourf* (2-D) graphs, the maps of the heat flux incident on the receiver and the map of the heat flux gradient are provided. These maps allow a visual approach to the studied case, and permit a better understanding of the main issues of the transient working conditions. Secondly, the solar field performances are showed through two different graphs: the first one (*Solar field by heliostats*), represents the efficiencies of each single heliostat by means of a color scale, from blue to red; the second one (*Solar field by zones*), shows the contribution of each zone of the field. In other words, the color designated for each zone is proportional to the heat flux that the latter transmits to the receiver, calculated as the sum of all the heliostats that belong to that zone.

The first graph allows to understand how the optical losses of each heliostats change during the year and during the day. In particular, it can easily show the contributes of the different losses: cosine effect, shadowing, blocking, spillage and atmospheric attenuation. Moreover, the second graph permits to identify the high efficiencies zones of the field and thus to understand which could be the most problematic shadowing type. This graphical representation qualitatively shows the field performances and leads to a better comprehension of the solar plant behavior during a cloudy day.

However, numerical results are needed in order to quantitatively analyze the outputs. For this reason, three main variables able to describe the potential stresses affecting the receiver have been chosen: peak values, temporal variation step-by-step and maximum gradient of the thermal flux. Each of these variables have been analyzed for each panel composing the receiver and all the data collected have been synthetized by means of *excel* graphs.

With the purpose of identify the most dangerous off-design condition and the best aiming strategy able to face it, all the possible combinations between aiming strategy and clouds have been analyzed. The obtained results clearly show that the best aiming strategy found for on-design conditions (previous study) it is the best also for the off-design ones. By doing a comparison with the remaining strategies it is possible to notice a strong reduction in all the parameters taken into account: 14÷33% reduction of the peak flux, 13÷19% reduction of the maximum gradient and 8.5÷28% reduction of the temporal variation of the peak flux. Concerning the clouds, the worst meteorological conditions for both the plants is the one that leads to the shadowing of the entire field. Moreover, by looking at the partial shadowing cases, another important result has been achieved: in most of the case the results obtained with a cloud affecting half of the field are similar to the one obtained for a smaller cloud that covers only some high efficiencies zones. In conclusion to this first part, it is possible to say that the worst cloudy day conditions are not always the ones with big clouds. The way in which a cloud crosses the field is a crucial factor: a small cloud passing on specific zones of the field could be worse than a big one covering half of the field.

In the second part of this thesis, the thermal maps previously obtained have been used as input for the simplified thermal model of the receiver of PS10, developed in Matlab. First of all, the geometry has been set: a layout of 336 straight and vertical pipes with a nominal diameter DN 2'' has been chosen. For sake of simplicity, it has been supposed that the water enters in the receiver in saturated conditions at the pressure and temperature imposed by the steam drum (250 °C, 40 bar). Moreover, the mass flow is equally subdivided in each pipe and it has been chosen in order to have a steam quality of 0.2 at the inlet of the steam drum. Furthermore, the pressure drops of the down-comers and of the up-risers are not taken into account. In the second step it has been defined the subdivision of the receiver surface in 168 elements, called flux units. This discretization has been done in order to be able to use the heat flux map previously calculated with Delsol3. Moreover, to each unit flux corresponds a constant heat flux value that is absorbed by 14 pipes.

A global thermal balance is imposed in order to find the temperature of each unit flux. The thermal power absorbed by each unit flux (q_{trans}), is the power coming from the field (q_{field}) subtracting the amount of the following losses:

- *Radiative losses*: the receiver is subjected to high temperature due to the strong energy incoming from the field and thus loses energy ($q_{lossrad}$) emitting radiations in the infrared and visible light according to the Stefan-Boltzmann law. Considering an emissivity of about 0.4 and different view factor for the internal and external panels (respectively 0.45 and 0.3) the calculation of this contribute can be achieved;
- *Convection losses*: some of the energy is lost because the air close to the receiver surface is heated and natural circulation phenomena occur. Only natural convection is taken into account because cavity receivers are thought to reduce the effects of forced convection. Moreover, in the case study, the wind is coming from south west, while the aperture faces north. This further reduces its effects. In order to calculate this effect the Churchill & Chu correlation is used;
- *Reflection losses*: a part of the radiation is not absorbed even if the pipes' surfaces are coated with a high absorptivity paint that minimizes this loss. This is due to the specific characteristic of the considered surface (reflectivity of 0.02 is considered);
- The amount of the losses through the interior in a concrete tower is very low compared to the external ones; therefore, for sake of simplicity they are not taken into account in the studied model.

The global thermal balance of each unit flux it is:

$$q_{trans} = q_{field} - q_{lossrad} - q_{lossconv} - q_{lossrefl}$$

An iterative process has been set up after calculating the thermal power actually transferred to each single pipe. In this way, it has been possible to compute the external surface temperature of the receiver. By considering the thermal power q_{trans} exchanged between the external surface and the working fluid, it is easily achievable the numerical value of $T_{wallExt}$. Both conductive and convective contributions (respectively of the pipe and of the internal fluid) have been taken into account to compute the overall heat transfer coefficient. To calculate the convective term of the working fluid has been used the Kandlikar correlation considering nucleate boiling conditions.

The model described is able also to produce other results: firstly, with *surf* and a *countourf* graphs it has been possible to study the thermal map of the whole receiver and a graphical representation of the temperature gradient is also displayed; secondly, several other results concerning the quantitative performance of the receiver have been obtained. These are the peak values, the temporal variation and the gradient of the temperature in each time-step. In order to synthetize the results it is has been necessary the *excel* support.

A cross-check between the aiming strategies and the different type of clouds has been done in order to reaffirm the conclusions previously obtained in the optical analysis. Assuming the worst cloud condition, the behaviors of the six strategies have been analyzed and the thermal maps have been produced; vice versa with the best aiming strategy and the different types of clouds. Finally, it is possible to say that the conclusion obtained with the analysis of the thermal maps verify the ones achieved with the optical study. The aiming strategy found is able to increase the thermal performance of the receiver, lowering both peak flux and temperature gradient. Even if some aberrations from the average values are

detected for the temperature gradient, the cloud previously described brings to the worst off-design conditions. Although these irregularities cannot disprove the conclusions, a deeper study of the real thermal stresses is recommended, to better understand the true thermal behavior and the hazard of the receiver.

Index

Abstract.....	5
Sommario	7
Introduction	9
1 Solar Energy	11
1.1 Solar Radiation.....	11
1.2 Available Technologies.....	11
1.3 Concentrating Solar Power.....	12
1.4 Solar Tower Power Plants	14
1.4.1 Power cycle	14
1.4.2 Tower	17
1.4.3 Receiver.....	17
1.4.4 Heliostat Fields.....	18
1.5 Energy performance of a heliostat field	20
1.6 Analyzed commercial Solar Towers	22
1.6.1 PS10	22
1.6.2 Gemasolar.....	23
1.7 Thesis Objective.....	24
2 Preliminary Studies	25
2.1 Clouds and wind.....	25
2.1.1 Clouds characterization	25
2.1.2 Wind characterization	27
2.1.3 Clouds modeling: PS10.....	28
2.1.3 Clouds modeling: Gemasolar	32
2.2 Aiming strategies PS10.....	36
2.2.1 Previous creation of the aiming strategies.....	36
2.2.2 Aiming strategies adopted.....	38
2.3 Aiming strategies GEMASOLAR.....	42
2.3.1 Previous creation of the aiming strategies.....	42
2.3.2 Aiming strategies adopted.....	43
2.4 Property of material at high temperature.....	47
2.4.1 Creep	47
2.4.2 Thermal expansion	48

2.4.3 Coating materials.....	48
3 Available Software for the required objective	49
3.1 DELSOL3.....	49
3.1.1 General description.....	49
3.2 Delsol limitations	49
3.2 De Giorgi’s software proposals	51
3.2.1 First solution: Microsoft Office Excel interface.....	51
3.2.2 Second solution: Mathworks Matlab interface.....	53
3.2.3 Graphical display.....	56
3.2.4 Limitations and weakness	57
4 Software Development.....	59
4.1 Explanation of the principal interface	59
4.1.1 Choice of the plant	60
4.1.2 Import Input file	60
4.1.3 Choice of the aiming strategy.....	60
4.1.4 Choice of the shadowing	61
4.2 Overall structure of the code	62
4.2.1 Graphical results.....	62
5 Thermal model	69
5.1 PS10 receiver model.....	69
5.2 Thermal model	71
5.2.1 Thermal losses.....	71
5.2.2 Energy Balance in a flux unit	73
5.2.3 Mathematical Iterative Process.....	77
5.3 Graphical Results	78
6 Discussion of the results.....	81
6.1 PS10	81
6.1.1 Heliostats efficiency and characteristics of the field.....	81
6.1.2 Numerical results.....	86
6.1.3 Worst conditions analysis.....	89
6.1.4 Selection of the best aiming	92
6.2 Gemasolar.....	96
6.2.1 Heliostats efficiency and characteristics of the field.....	96
6.2.2 Worst conditions analysis.....	102
6.2.3 Selection of the best aiming	105
6.3 Numerical results of the Thermal model.....	109

7 Future developments	117
7.1 Software improvements.....	117
7.2 Thermal model improvements	118
Conclusions	121
Figures Index	123
Tables Index	127
Nomenclature and acronyms index	128
References	130

Abstract

The aim of this thesis is to analyze the performances of two commercial solar towers, PS10 and Gemasolar, in off-design conditions. It is studied how the systems work with a reduced and variable DNI due to clouds passage on the solar fields, with a particular focus on the receivers. This component is one of the most critical elements of the plant because it is subjected to very high heat flux coming from the heliostats. Moreover, during transient operations, high energy flux variations cause sudden temperature changes that lead to stresses in the receiver material. In the first part of this work, several aiming strategies are studied, in order to understand which one leads to lower values of peak flux and flux gradient in off-design conditions. Heat flux maps are calculated with Delsol3, a software for performance simulation of Solar Power Plant developed by Sandia National Laboratories, creating an user interface with Matlab. This first optical study shows how the best aiming strategy found for on-design conditions in previous studies is the same also for the present work. The main idea of this strategy is to spread the incident radiation on the entire receiver surface, in order to decrease the peak flux values without a strong impact on the energy production. In the second part of the work, the obtained heat flux maps are used as inputs in a thermal model, implemented in Matlab. The model simulates the heat exchange in the PS10 receiver and produces temperature maps from which it is possible to understand the issues of the off-design conditions. The obtained thermal behavior of the receiver verifies the conclusions made with the optical study: the aiming strategy previously found is able to improve the thermal performance of the receiver, reducing peak fluxes and temperature gradients. Only a few slight deviations from the normal trend are found. In order to better understand these irregularities, several possible improvements of the present codes are proposed and a deeper study of the real thermal stresses is recommended.

Keywords:

Concentrating Solar Power, Optical Performances of a Solar Tower, Aiming strategies, Transients conditions due to passage of clouds, Software interface developments, Receiver Thermal Performances.

Sommario

La presente tesi ha come scopo l'analisi delle prestazioni di due impianti solari a torre commerciali, PS10 e Gemasolar, in condizioni di funzionamento off-design. Per raggiungere questo obiettivo si è rivelato necessario uno studio sulla risposta del sistema ad una radiazione solare variabile e ridotta a causa del passaggio di nuvole sul campo solare, con particolare attenzione al comportamento del ricevitore. Questo componente è infatti uno degli elementi più critici dell'impianto, a causa del grande carico termico a cui è soggetto. Inoltre, durante i transitori presi in considerazione, le elevate variazioni di quest'ultimo causano repentini gradienti di temperatura che possono portare ad elevati stress termici nel ricevitore. Nella prima parte del lavoro sono analizzate varie strategie di puntamento, con lo scopo di individuare quella che comporta valori inferiori del flusso termico incidente e del gradiente di quest'ultimo. Le mappe di flusso sono calcolate con Delsol3, un software sviluppato da Sandia National Laboratories che permette di simulare il funzionamento di impianti solari a torre. Per rendere il suo utilizzo più intuitivo e immediato viene inoltre programmata una interfaccia in Matlab. Questo primo studio ottico mostra come la strategia di puntamento che si era rivelata essere la migliore in condizioni nominali (studi precedenti), continui ad essere la migliore anche nel presente elaborato. La idea di fondo di questa strategia è quella di distribuire la radiazione incidente più omogeneamente sull'intera superficie del ricevitore, in maniera tale da diminuire i valori dei picchi di flusso senza ridurre la produzione di energia. Nella seconda parte del lavoro, le mappe di flusso precedentemente ottenute sono utilizzate come input per un modello termico, sviluppato in Matlab. Quest'ultimo è in grado di simulare lo scambio termico nel ricevitore della PS10 e di ottenere il profilo di temperatura della superficie esterna del ricevitore stesso, da cui è possibile analizzare le problematiche derivanti da condizioni di utilizzo diverse da quella di disegno. I risultati dello studio termico verificano le conclusioni ottenute con lo studio ottico: la strategia di puntamento trovata in precedenza è in grado di migliorare la performance termica del ricevitore, riducendo sia i picchi di flusso che i gradienti di temperatura. Si riscontrano solo delle piccole deviazioni dagli andamenti medi. Per individuare la fonte di queste irregolarità, vengono proposte diverse modifiche e miglioramenti per entrambi i codici sviluppati e si raccomanda lo svolgimento di uno studio più dettagliato sui reali stress termici prodotti.

Parole Chiave:

Solare termodinamico a concentrazione, Prestazioni ottiche di una Torre Solare, Strategie di puntamento, Transitori dovuti al passaggio di nuvole, Sviluppo interfaccia software, Prestazioni termiche del ricevitore.

Introduction

Research in Concentrated Solar Power fields and related thermodynamic cycles began more than 40 years ago, and in the last decade this technology has undergone a huge growth in the commercial applications. A lot of thermo-economic analyses have been made, and in 2007 the first commercial plant started its energy production: PS10, located in Sanlúcar la Mayor, Seville, Spain. The latter is a 10 MW_{el} power plant characterized by a north field and a cavity receiver configuration. Despite the previous test plants that tried new kind of innovative receivers and several layout of the power cycle, for this first commercial plant an easier solution has been adopted. In order to increase the reliability, the system produces saturated steam later expanded into a steam turbine. A few years later, in 2011, a new commercial solar tower was launched: Gemasolar, situated in Fuentes de Andalucía, Seville, Spain. This plant differs both in size and configuration from PS10: it provides a production of 19.9 MW_{el}, with a surrounding field and the receiver is an external one. Moreover it uses molten salts as working fluid and has a heat storage to allow continuous operation also during night. In order to consider a general scenario of the existent commercial facilities, both in terms of field, receiver and working fluid, PS10 and Gemasolar constitute the object of the present dissertation. Therefore, in the chapter 1 an introduction to the solar energy is provided, with a description of the principal technologies available to exploit it and a detailed analysis of the two plants of interest.

In order to reduce the electricity cost and increase the competitiveness of these plants, some changes in the existing plant management possibly have to be made, along with a global cost reduction (in particular the O&M one). For these reasons, in this work a way to find out critical aspects during off-design working conditions due to the passage of clouds is investigated. In fact, a deep analysis on these aspects would allow to highlight weakness in the operation strategies, and permit to improve the plant management. In order to do this, a previous investigation on the characteristics of clouds and wind and the way to model them in Matlab has been made, and it is explained in chapter 2. The latter also explains the different aiming strategies used, and their construction. Afterwards, a software for performance simulation of Solar Tower Power Plants is adopted in order to test these strategies and consequently obtain the correspondent heat flux maps on the receiver of the two plants. Delsol3 of SANDIA National Laboratories has been chosen, due to its powerful features explained in chapter 3. Moreover, a Matlab interface has been developed, to allow an easier communication with Delsol3. The explanation of this interface, along with a review of previous studies that made possible its creation, it is provided in chapter 3 and 4.

Moreover, a thermal model to predict the behavior of the receiver of the PS10 when a cloud is passing over the field has been developed using Matlab, and it is fully explained in chapter 5. This code uses the flux maps obtained with Delsol3 as inputs, and allow the calculation of the temperature on the surface of the receiver.

The results obtained with the first code and the correspondent observations and conclusions are examined in the first part of chapter 6. The crucial avail of this work is that

the cost for the implementation of the possible improvements achieved would be virtually negligible. In fact, only *software* modifications on the aiming strategies of the heliostats would be necessary, and not *hardware* ones in their drive mechanisms or other components of the plant. Moreover, passing from a heat flux map to a temperature map, further analysis on the thermal stresses are made possible and a validation of the previous observations is permitted.

In chapter 7 are described some possible developments of the software for future analyses.

Chapter 1

Solar Energy

In this first chapter an introduction of the Solar energy is provided, with a description of the principal technologies available to exploit it.

1.1 Solar Radiation

The sun is a star that behaves as a black body at the temperature of 5777 K. Inside its core several fusion reactions take place, in particular the fusion of 4 protons of Hydrogen into 1 Helium atom, and supply the energy that the sun emits. The latter is then transferred from the interior to the external surface by a succession of radiative and convective processes. The sun irradiates to the Universe 3.824×10^{20} MW but, due to the high distance (1.495×10^{11} m) and the dimensions of the two bodies, only 172.5×10^9 MW are intercepted by the Earth. This amount of energy is defined by the “Solar Constant”, 1367 W/m², which represents the mean value of thermal power received, outside the atmosphere, per unit area normal to the propagation direction.

The Solar Constant does not coincide with the radiation value effectively incident on the earth surface because of the influence of the atmosphere: two phenomena intervene to reduce it, absorption and scattering.

The first consists, as the word says, in the absorption of part of the radiation by the particles composing the atmosphere, in particular water, molecular oxygen and ozone.

The scattering of radiation, instead, is caused by interactions with air molecules, water, and dust. The level of scattering is a function of the number of particles through which the radiation must pass and the size of the particles relative to the wavelength λ .

The reduction to the irradiation introduced can vary between the 30% (perfectly sunny days) and 90% (cloudy days).

1.2 Available Technologies

The energy radiated by the Sun and intercepted by the Earth's surface can be exploited through two main technologies: Photovoltaic and Solar Thermodynamic.

The first performs a direct conversion between solar and electrical energy using the “Photovoltaic Effect”, i.e. the ability of the photons composing the solar beams to increase the energy state of the electrons when hitting particular semi-conductors materials.

The strength of this technology is the ability to use both the direct and the diffuse radiation; the weakness, on the other side, is the low efficiency of the process “solar to electricity”, limited to 17-18% for the most expensive photovoltaic cells.

The second type does not imply a direct conversion to electricity: firstly the solar energy is converted into thermal energy by heating a vector fluid, and then follows the expansion of the latter in a power plant cycle to produce electricity.

A further division can be made, in terms of the use of the solar radiation. In fact, the radiation coming from the Sun can heat the vector fluid directly or after a process of “concentration” in smaller areas.

The latter is the category called “Concentrating Solar Power” (CSP), which is the object of the present study.

1.3 Concentrating Solar Power

In order to study the CSP, a brief introduction needs to be done. The principal purpose of the concentration of the radiation from a Collecting Area (A_C) to a smaller Absorbing Area (A_A) is the growth of the heat fluxes employed to increase the vector fluid enthalpy. The main result is the achievement of higher temperatures and, consequently, higher efficiencies of the thermodynamic cycles. In addition, smaller surfaces at high temperature have smaller heat losses towards the atmosphere. The ratio between the Areas described, constitutes a fundamental parameter for these plants, called Concentration Ratio (C_R):

$$C_R = \frac{A_C}{A_A} \quad (1.1)$$

This factor, along with temperatures of the vector fluid, results to be the crucial variable of the optimization process of the efficiency of a receiver.

The conversion of solar thermal electricity (STE) is mainly based on four CSP technologies:

- parabolic dish collectors (PDC);
- linear Fresnel collectors (LFC);
- central tower systems (CRS);
- parabolic trough collectors (PTC).

Linear Fresnel and parabolic trough collectors are line-focusing concentrators and needs a single-axis tracking system (see figure 1.1). Their C_R results to be lower than 100 and are characterized by medium temperature levels up to 550 °C (see Table 1.1).

On the other hand, parabolic dish and central tower systems are point-focusing concentrators featuring a two-axis tracking system. They can reach C_R greater than 1500 and high temperatures above 1500 °C.

Due to this fact, the latter are expected to achieve higher efficiencies of energy conversion. Currently, the annual solar-to-electricity efficiency may achieve 13% for LFC plants, 11% to 16% for PTC, 12% to 25% for PDC, and 7% to 20% for CRS [1].

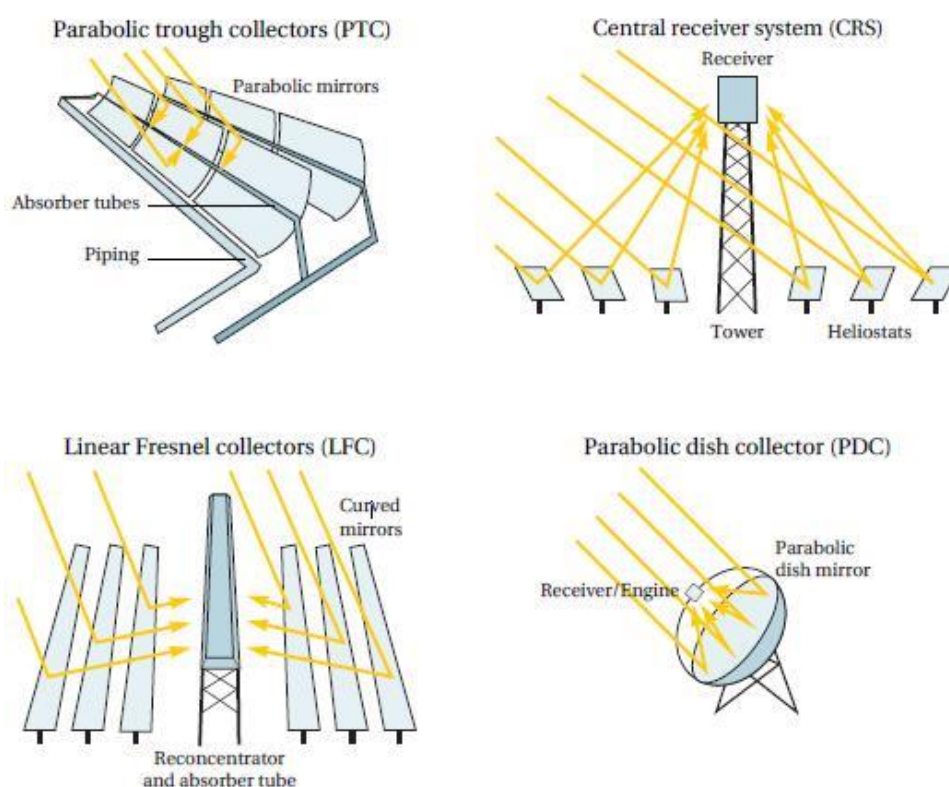


Figure 1. 1. Concentrating solar collectors (adapted from [2]).

In regard to the cost of electricity, nowadays only PTC and CRS plants are developed enough to provide an estimate of their range of variation: respectively $14 \text{ } \$/kWh_{el}$ to $36 \text{ } \$/kWh_{el}$, and $17 \text{ } \$/kWh_{el}$ to $29 \text{ } \$/kWh_{el}$. Looking at the medium-term, a series of potential cost improvements have been identified, leading for instance to a projected cost of $8 \text{ } \$/kWh_{el}$ for central tower plants by 2020 [3]. Even more challenging, the SunShot initiative launched by the U.S. Department of Energy (DoE) in 2011 aims at grid parity for CSP in general with $5\text{-}6 \text{ } \$/kWh_{el}$ without subsidies [4], which requires disruptive rather than incremental technological advancements over the current decade [5].

Collector	Focus	Tracking	C_R	T [°C]	Sol-to-El eff. [%]	LEC [$\$/kWh_{el}$]
Linear Fresnel	line	Single-axis	10 - 40	60 - 500	13	-
Parabolic trough	line	Single-axis	10 - 85	60 - 550	11 - 16	14 - 36
Parabolic dish	point	Two-axis	600 - 2000	100 - 1500	12 - 25	-
Central tower	point	Two-axis	300 - 1500	150 - 2000	7 - 20	17 - 29

Table 1. 1. Concentrating solar collectors (adapted from [6])

As central tower plants result to be the technology that shows the highest potential improvement both at the energy level and the economic level, they are the object of the present study.

Firstly a brief state of the art is provided, presenting the different power cycle set-ups and the characteristics of the solar tower and the receivers; secondly, the main features of the fields of heliostats are discussed and the commercial plants of interest are described.

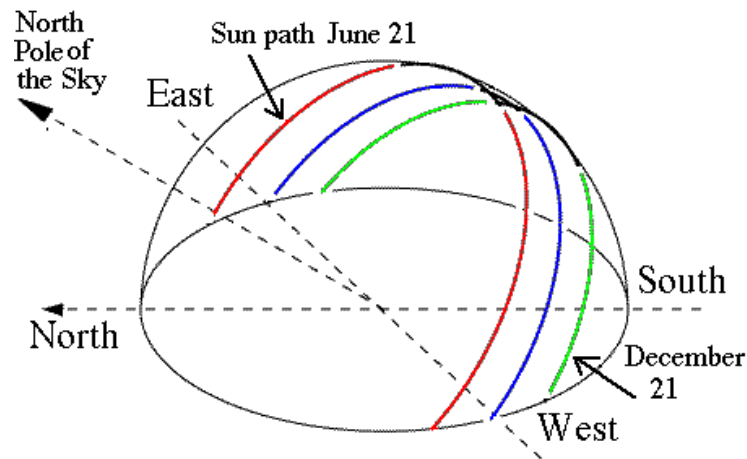


Figure 1. 2. Sun motion in the sky (azimuth-elevation angles variation) during a day, for solstices and equinoxes.

1.4 Solar Tower Power Plants

Solar Tower power plants consist of fields of mirrors, called heliostats, collecting the solar radiation and reflecting it towards a receiver situated at the top of the tower. There the incoming radiation is transferred to a fluid through a heat exchanger and the obtained thermal energy is converted into electricity in a power cycle.

1.4.1 Power cycle

Nowadays, the conversion cycles experimented in this technology are mainly four, and only two of them are used in an industrial and commercial scale:

- pressurized air cycles, experimental (e.g. Solugas [7]);
- atmospheric air cycles, experimental (e.g. Jülich [8]);
- molten salt cycles, 17 MWel in commercial operation (Gemastar [9]);
- direct steam cycles, 36 MWel (PS10 [10], PS20 [11], Sierra Sun Tower [12]) and 29 MWth (Coalinga [13]) in commercial operation.

As shown in Figure 1.3, in the pressurized air cycles the air passes firstly in a turbo-compressor of a gas turbine block. Afterwards, it is heated in a pressurized receiver at temperatures of 800-900 °C [14] and sent to a combustion chamber, where the fuel is added and the mixture goes through a combustion process. Then, the exhaust gases pass in

a turbine and after that in a steam generator of a Rankine cycle, allowing the increase of the overall efficiency with a combined cycle.

Moreover, there also some proposals of more advanced cycles, including a tower-mounted topping gas turbine in addition to the main ground-based gas turbine [15].

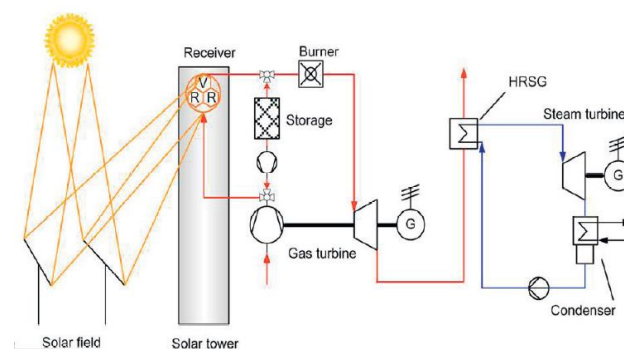


Figure 1. 3. Pressurized air cycles (adapted from [16])

In the atmospheric air cycles plant (see figure 1.4), the ambient air passes through a volumetric receiver made of wire mesh of porous ceramic foam [17]. There it is heated by the solar radiation to temperatures of 680-950 °C, and then it could be directed either through a packed bed storage unit, typically made of rocks [18] during the charge process, or through a steam generator during the discharge. Afterwards, the air returns to the inlet of the receiver, with the possibility of a re-cycle of the 45 % [5].

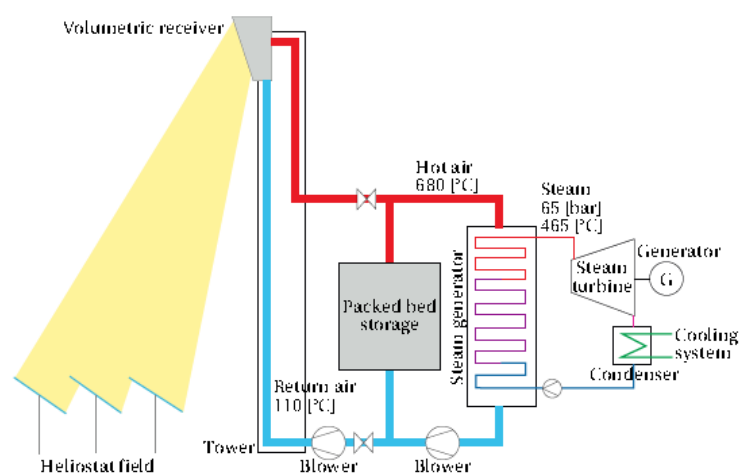


Figure 1. 4. Atmospheric air-based cycle (Jülich solar tower, adapted from [19]).

The molten salt cycle is the conversion cycle used in the commercial plant Gemasolar in the province of Seville, Spain, and thanks to its storage system results to be one of the most important topic of research and development for the future of this technology. The molten salt is pumped from the cold storage tank (290 °C) to the receiver, where it is heated up to 565 °C and then is stored in the hot storage tank (figure 1.5). Afterwards, the molten salt passes through a steam generator in order to run a conventional steam cycle, and finally returns to the cold storage tank. Depending on the amount of molten salt used, the storage capacity may reach 15 hours per day, allowing 24 hours of operation on a summer day. Moreover, other proposals are being considered and developed, such as the use of new

salts with wider liquid temperature range in order to enable the generation of supercritical steam [20].

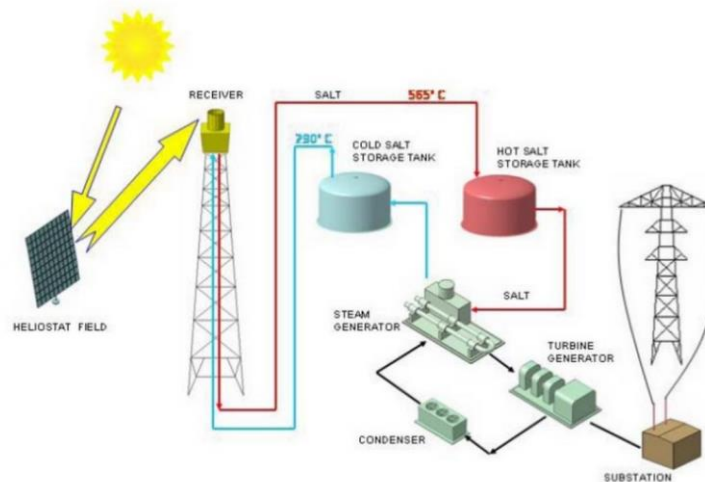


Figure 1. 5. Molten salt cycle plant [21].

Direct steam cycle power plants are different from the previous ones, because the fluid expanded in the steam turbine is the same that is heated in the receiver. In the figure 1.6 it can be seen that the feed water is pumped and passes through the receiver, where it is evaporated typically up to a steam quality of 0.2-0.3. Afterwards, the fluid goes to a steam drum that divides the steam and saturated water. Then the steam, maintained at saturation conditions (250 °C and 40 bar [10], is accumulated back to the ground in a short-time buffer tank that allows a regulation capacity of about 45 minutes at half nominal power. After that, the steam is expanded in the turbine, condensed at about 0.06 bar and 50 °C and finally pumped up in the tower again.

The main future improvement for this technology could be the generation of superheated steam, in order to make possible the use of larger industrial turbines and to increase the cycle nominal efficiency [22].

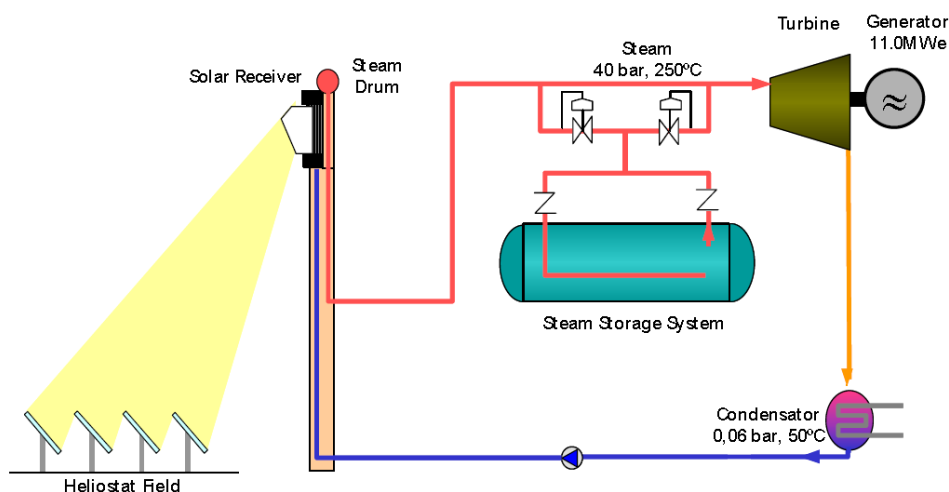


Figure 1. 6. Direct steam cycle plant (PS10, adapted from [23]).

1.4.2 Tower

The central tower presents the receiver at its top and has to reach a considerable height, at least around 100 meters, in order to allow the furthest heliostats to create a sufficiently good reflected image on the receiver. Moreover, the tower has got also another essential task that concerns the fact that the heat transfer fluid is conducted up and down it. It must be able to guarantee the appropriate insulation to avoid heat losses by convection to the atmosphere and by conduction through the structure and at the same time be sufficiently spacious to contain all the pipes. Finally, the tower should also be designed by keeping in mind the sensitivity to wind, the shadow projected onto the field and the impact on the landscape in the distance.

The structure of the central tower could be made either of steel lattice or reinforced concrete. The first option obviously causes slightly less shadow on the field, but also a worse pipe insulation and wind resistance. The great majority of the commercial plants present reinforced concrete towers, using them also as buildings with rooms dedicated to various experiments.



Figure 1. 7. Steel lattice vs Concrete Tower. a) Ivanpah, b) Gemasolar.

1.4.3 Receiver

The receiver of a central tower is a delicate component, due to the fact that it receives the concentrated solar radiation resulting in thermal fluxes of high intensity. There are two main concepts of receiver: cavity ones or external ones. In a cavity receiver the absorbing surface is located inside the tower, and the radiation enters through an aperture. In this way convection and radiation heat losses to the atmosphere decreases, in spite of a strong

reduction of the acceptance radiation angle. Then, cavity receivers are normally use individually and only in north-field plants, for example PS10 or PS20.

External receivers are not protected, and so more disposed to thermal losses, either convection ones due to the wind cooling or radiation ones to the sky. On the other hand, they have no limitations on the acceptance angle and this is a perfect feature to work with surrounding fields, for example Gemasolar.

Moreover, the receiver elements can be attached together in different overall pattern, normally in a flat or a cylindrical geometry. The first one may tilt towards the field to improve the capture of the radiation; the second one may be in the form of a half-cylinder cavity receiver, or of a full cylinder external receiver. Considering the two plants of interest for this work, PS10 and Gemasolar, they present respectively a cavity receiver formed by four flat panels attached together in a shape of a half-cylinder, and an external cylindrical receiver.

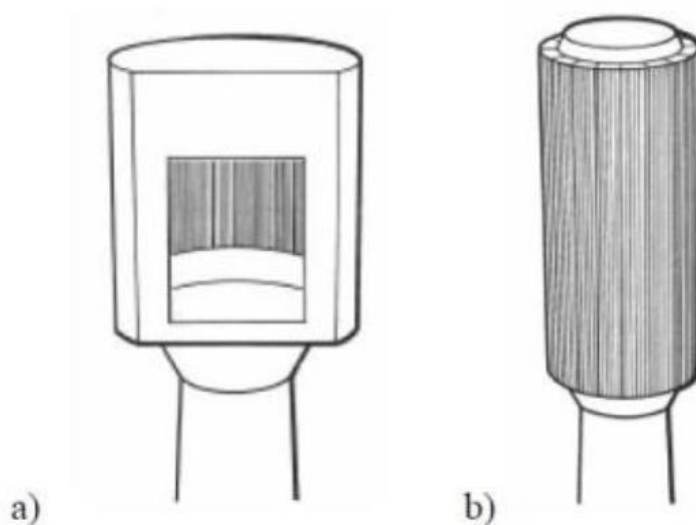


Figure 1. 8. a) Cavity receiver, b) External receiver

1.4.4 Heliostat Fields

In the last forty years more than 30 solar fields have been designed and built worldwide, but only a few of them are for industrial commercial facilities. The majority are experimental fields, of medium-small size, constructed in order to start the tests on the CSP technology. Examples of these fields are the CRTF in Albuquerque, USA (1978) or the Thémis tower in Targassonne, France (1982). Moreover, a few pilot plants were commissioned as well, such as Solar One and Two in Barstow, USA (1982 and 1996) or the SEDC in the Negev desert, Israel (2008) in the recent past.

As regards the commercial plants, the first one ever built and started-up is the PS10 in Sanlúcar la Mayor, Spain (2007). Since this moment, several commercial facilities have been designed and built, and they can be categorized according to their total reflective area in: small-scale ($<10^7$ 000 m²), medium-scale (10⁷000-100⁷000 m²), and large-scale facilities ($>100^7$ 000 m²) [5]. The aim of small-scale facilities such as the Solastor field in Lake Cargelligo, Australia (2011) is to provide electricity and/or heat to relatively small

communities. Medium-scale facilities like the Sierra SunTower in Lancaster, USA (2009) are designed to satisfy the demand of local industrial scenarios. Finally, large-scale facilities such as PS20 and Gemasolar in Spain (2009 and 2011), and Ivanpah in California (2013), run towards heliostat fields with more than 1'000'000 m² of total reflective area, in order to satisfy greater electrical demands. This could be the starting point for multi-tower set-ups.

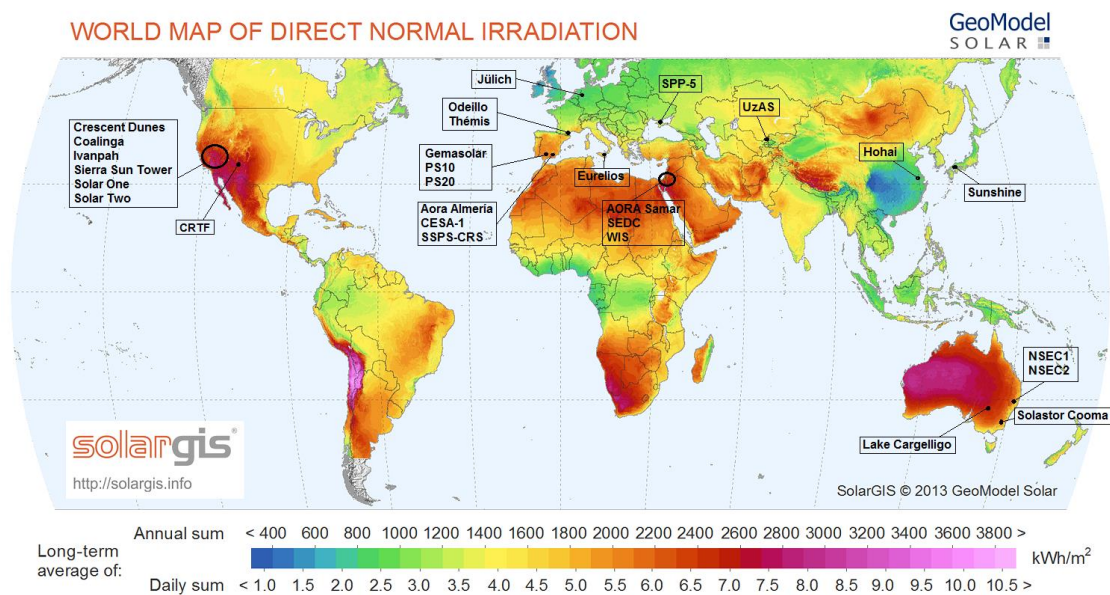


Figure 1. 9. Map of Heliostat fields worldwide, with DNI (adapted from [24]).

It can be easily observed from figure 1.9 that the majority of the Heliostat fields are situated in developed countries, especially in zones characterized by high values of DNI, at least 2500 kWh/m^2 . Existing commercial facilities can be found in western USA, eastern Australia, southern Spain and middle-east, but not yet in the Sahara zone, southern Africa, Mongolia, Chile, Argentina or Brazil. This can be easily explained considering that the DNI is not the only factor to be taken into account. Also topology, hydrography, land cover and power network available have to be considered to design a solar power plant, along with a social and political point of view [8].

Basically, the field layouts can be divided in two main categories: *North-field* (or South, considering the Southern hemisphere) or *surrounding field*. The first one presents the whole group of heliostats only on one side of the central tower, whereas the second one is characterized by mirrors that completely surround the tower. The selection of the layout mostly depends on the site's latitude and on the chosen receiver: the North-fields normally are coupled with cavity receivers, surrounding ones with external ones. The experimental facilities normally feature a North-field layout, the commercial ones can present both of them (e.g. PS10 and PS20 north-field, Gemasolar and Ivanpah surrounding field).

Another distinction could be made on the disposition of the mirrors in the field layout, and it can be defined two kinds of dispositions: *grid* and *circular* layouts. The first ones present heliostats disposed by a simple grid of W-E and S-N rows; the second ones by concentric circles whose center is the tower's base. In the two cases, the spacing between rows may increase with the distance to the tower's base in order to decrease interferences between neighboring heliostats. Nevertheless, the final layouts are normally calculated via software

with a techno-economical optimization: the results, generally speaking, are irregular shapes characterized by a higher presence of mirrors in the Northern part of the field (considering the Northern hemisphere), due to the better incident angles of the sun.

The mirrors composing the field, called heliostats, require high values of reflectivity, together with other important characteristics such as a great accuracy of the tracking system, resistance to wind, and low specific costs. They are moved by a drive mechanism in two directions (azimuth-elevation) in order to follow the daily sun motion in the sky and intercept the radiation with the highest normal surface component possible. Heliostats can be composed of a single mirror panel or an assembly of several panels, mounted on a frame supported by a horizontal axis and a vertical axis. The panels, both of rectangular or circular shape, can present a slight convex curvature in order to obtain a more focused image on the receiver. The wind results to have a considerable impact on the mirrors, causing them to oscillate, and also the fouling effect can deteriorate them. In order to prevent this, periodical washing to contrast the loss of reflectivity are required.

Finally, the heliostat field is the part that affects the most to the installation cost of the entire plant, because of the huge number of mirrors (from hundreds to thousands) and the bi-dimensional driving system required for each of them.

1.5 Energy performance of a heliostat field

The performance of the heliostat field is affected by several losses, caused by optical, geometrical and physical factors on one hand and by the interaction between neighboring mirrors on the other hand. The principal losses between the direct normal irradiance incident on the heliostats and the concentrated beam on the receiver are:

- *Cosine effect*: losses caused by this effect are due to the fact that the heliostats are not perpendicular to the incident insolation, and the result is that they are using a smaller area than the real available one. In other words, the mirrors can reflect towards the receiver only a part of the incident radiation, due to their inclination. This kind of losses cannot be avoided at all: since a heliostat continuously reflects in a fixed direction, given by the position of the receiver, the only moment in which it will be perpendicular to the sun vector would be when the sun is aligned with the receiver. However, in this case the sun would be obviously hidden by the tower itself.

The cosine losses slightly increase with the distance from the receiver, due to the fact that furthest heliostats are a little more misaligned with the receiver and the sun. Moreover, these losses have a particular evolution throughout the day: west-side heliostats show minimal losses in the morning and maximal losses in the afternoon, and vice-versa for east-side heliostats.

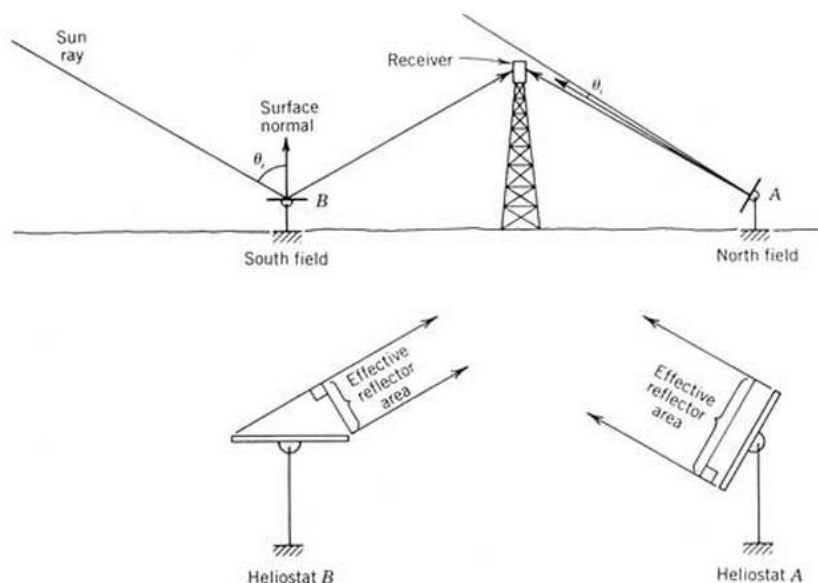


Figure 1. 10. The cosine effect for two heliostats in opposite directions from the tower. Heliostat A in the north field has much greater cosine efficiency than heliostat B (at noon). [25].

- *Spillage*: these optical losses appear when the image of the radiation reflected by the heliostats on the receiver is larger than the area of receiver itself. If it happens, a portion of the reflected radiation will not contribute to the heating process, and then it will be lost. A simply way to calculate the spillage losses is with the ratio between the portion not caught by the receiver and the whole reflected radiation. The furthest heliostats obviously present greater values of spillage, due to the fact that they produce a bigger image on the receiver than the nearest ones.
- *Atmospheric attenuation*: these losses are cause by the interaction between the reflected radiation and the atmospheric air from the heliostat to the receiver, due to absorption and diffusion processes, and obviously increase with the distance from the receiver.
- *Reflectivity and Cleanliness*: the *reflectivity* losses represent the amount of radiation that is not reflected by the clean mirror, instead of the *cleanliness* losses that are the amount of radiation that cannot be reflected due to absorption and diffusion through dirt on the mirror itself. Reflectivity strongly depends both on the quality of the mirror surface and on its resistance to corrosion, whereas cleanliness depends on dust deposit and the frequency of cleaning or raining.
- *Shadowing and Blocking*: these two losses, differently from then previous ones, are caused by the interaction between neighboring mirrors. As it can be observed in the figure 1.11, the *shadowing* occurs when one heliostat is in the shadow of one or more neighbors, so it happens before solar radiation hits the considered heliostat. These losses are calculated by projecting the images of the covering mirrors on the covered one, along the incoming radiation's direction. As a consequence, the shadowing loss results to be the ratio between the overlapping area and the total area of the considered heliostat. Otherwise, the *blocking* occurs when the radiation reflected from a given heliostat cannot reach the receiver, because it is partially

“blocked” by other neighboring heliostats that intercept the radiation itself. These losses are calculated in the same way of the shadowing ones, with projected areas. The great difference between these two losses is that in the blocking the direction of the radiation is constant (heliostat always aims to the receiver), instead of the shadowing’s one that depends on the position of the sun. The consequence is that the blocking losses can be avoided or strongly reduced by a smart selection of the field layout, through an optimization of the azimuthal and radial spacing between the heliostats.

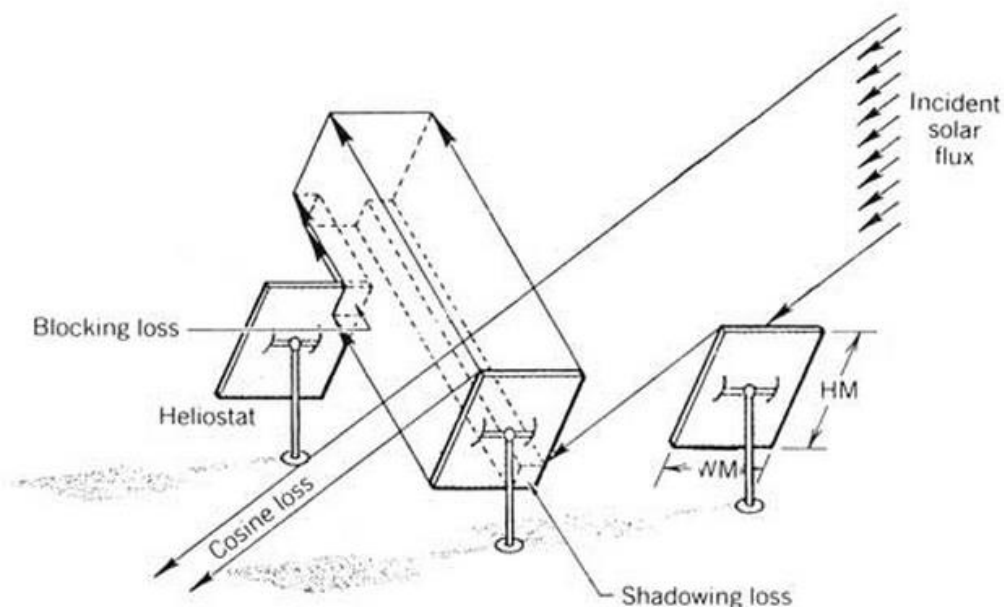


Figure 1. 11. Shadowing and blocking loss [25].

1.6 Analyzed commercial Solar Towers

The present study conducts an analysis of two Solar Tower power plants in particular, that are the Spanish plants “PS10” and “GEMASOLAR”.

A detailed description is included in the following paragraph, with a discussion of their different features, from the dimensions, to the receiver shape and the heat exchange fluid.

1.6.1 PS10

The “Planta Solar 10” is the first commercial Solar Tower power plant of the world [26]: its construction ended in 2007 and since then it has been connected to the electrical grid and has supplied a mean value of 24.3 GWh/year. It is located in Sanlúcar la Mayor, Seville, and it is property of Abengoa Solar. It presents a North field, composed of 624 heliostats and occupying a surface of 600000 m², of which the 13% is composed of reflecting surface.

The receiver is located inside a cavity situated at 100 m from the ground and the heat exchange fluid is water, which is then directly expanded in the power cycle.

The plant has a nominal power of 11 MW and its cost has been of 3000 €/kW_{gross} (thus resulting in an investment cost of about 35.000.000 €).



Figure 1. 12. PS10 Solar Tower Power Plant.

1.6.2 Gemasolar

Gemasolar plant is rather recent, it became operative in 2011, and employs innovative technologies. It has a nominal power of 19.9 MW but presents a storage system dimensioned for a continuous operation of the plant (15 hours storage for a 24 hours a day working), where the only stops are made for maintaining or for prolonged bad weather conditions. The resulting working hours for a year are about 6500 and the energy production of 110 GWh/year. The heat exchange fluid is the same of the storage, i.e. a mixture of molten salts. The two tanks of the storage are kept at 565°C and 270°C. This allows the production of a steam that enters the turbine at 100 bar, 540 °C, resulting in good efficiencies of the cycle (40%). The heliostat field surrounds the tower and is composed of 2650 mirrors (for an overall surface of 185 Ha, almost 2 km², of which the 15.6% reflective); the receiver is therefore external cylindrical. The tower is 147 meters high and the receiver is 16 meters high with an 8 meters diameter.



Figure 1. 13. Gemasolar Solar Tower Power Plant.

1.7 Thesis Objective

In this thesis it has been decided to analyze the performance of a solar tower in off design conditions. It has been study how the system works with a reduced and variable DNI due to clouds passages on the solar field.

Starting from previous studies done on the on-design conditions for the same plants, a further improvement has been done. It has been studied how the shadow on the solar field affects the incident radiation on the receiver and thus how the temperature map of the latter changes during cloudy days.

Even if the plant studied receives at least nine hours of sunshine 320 days per year, with 15 hours per day in midsummer, this aspect is very important to understand the optical and thermal behavior of the system and the related stresses on the solar receiver. The latter is one of the key equipment in a solar tower power plant and operates under extremely non-uniform heat flux, cyclic weather and cloud transient cycle conditions. Very high and quick changes of radiation lead to sudden variations of heat flux. Despite the null “fuel” cost, the kWh cost resulted to be twice the mean traditional plants kWh cost [26]. This work investigates a way to reduce the cost of this rather new technology and improve the management of this system reducing the cost of order and maintenance. The idea is to find a correct aiming strategy that can prevent premature failure. It has been investigated which can be the proper tracking of heliostats simulating different type of clouds covering the field over specific days of the year. Different scenarios are simulated choosing the most common and unfavorable weather conditions for the specific plant studied. The objective is to understand if the best aiming strategies found in previous studies on the on-design conditions are the best also for the off-design.

Chapter 2

Preliminary Studies

In this chapter a series of concepts, fundamentals for the comprehension and development of the present study, are presented. The fundamental features of all these topics are resumed, along with the suppositions and approximations made to achieve an easier model of the problem object of study.

2.1 Clouds and wind

2.1.1 Clouds characterization

One of the most important role of water in the earth system is its regulation of climate. The average earth's surface temperature is kept cooler than it would be thanks to the evaporation of the water from the ground. Furthermore water vapor is an important absorber of long wave radiation (infrared); in fact, it is the most important greenhouse gas in the atmosphere and helps the whole earth system to keep an almost stable temperature [27].

This thesis focuses on the off-design working conditions due to unfavorable meteorological states. For this reason, a preliminary study about clouds and wind characterization has to be done: this step is very important because the entire thesis is based on these first considerations.

Clouds are representative, and thus lead, to complex meteorological phenomena such as rain, snow and hailstorm. From a thermodynamic point of view, clouds are the visual aspect of several events that take part in a gaseous fluid known also as atmosphere: temperature, humidity and pressure.

Clouds are challenging to model because of the very high inhomogeneity in type, shape and velocity, and they are universally classified by altitude range.

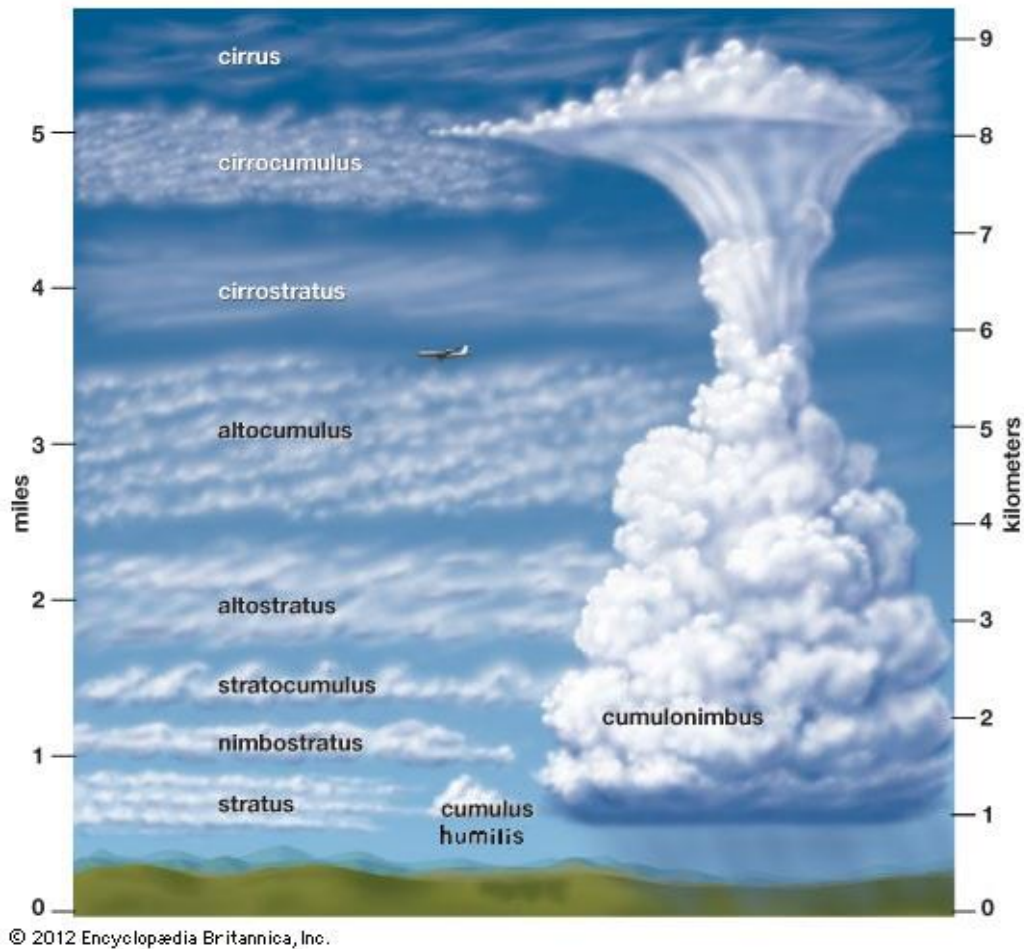


Figure 2. 1. Clouds classification by altitude of occurrence, adapted from [28].

The type of clouds taken into account in the present study are the “*cumulus humilis*”, that are also known as the “clouds of good weather” [29]. They are characterized by a flat light grey bases and small white domed tops. Usually the vertical height from base to top is less than the width of the cloud base. This type of clouds are the worst for this type of plants because leads to fast alternating DNI. Rapid change among blue sky (with a DNI of about 1000 kW/m²) and shadow (DNI = 0) leads to a unstable working operation for the solar tower.

These clouds come in a range of sizes, from small popcorn cumulus to large tropical cloud clusters [30]. The boundary of the clouds are, usually, highly irregular. It is extremely difficult, if not impossible, to model them as any common geometric figure [30].

The velocity of a cloud is obviously related to the wind speed at that height. A lot of study has been done on this topic. Hisashi Kon [31] demonstrated that the ratio between wind speed and clouds speed decreases with the height due to the variation of density of the clouds. Moreover, it has been seen that due to the fact that wind speed increases with the height, these two phenomena offset each other. For these reason the clouds assume a quite uniform velocity along its axis and the speed is very close to the average wind speed touching the cloud. An assumption done in this work is that the clouds have the same speed and velocity of the wind. Moreover it is assumed that the transmittance of the cloud

is zero. It means that all the direct solar incident radiation is stopped by the cloud. Furthermore a hypothesis on the boundary was made: edge sharpness, to avoid further complexities.

2.1.2 Wind characterization

PS10 is located in Sanlúcar la Mayor, in the Seville province, a floodplain formed by the Guadalquivir River, in the Andalusia region. The latter is approximately in between 36° and $38^\circ44'$ parallel in the south of Iberian Peninsula. Its climatic analysis shows that it is an area in which masses of air from the Atlantic Ocean flow. During spring and summer a humid and warm wind comes from the third quadrant (S-W), and it turn to the first (S-E) during fall and winter. This last, as counterpart, is dry and cold [32].

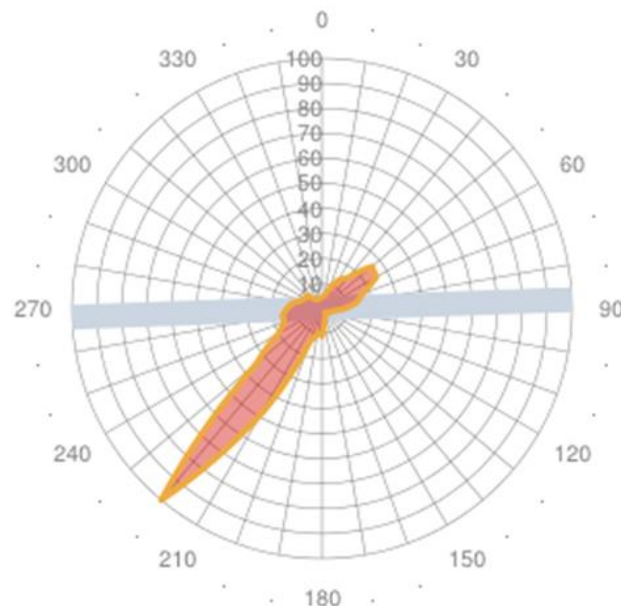


Figure 2. 2. Wind profile measured in the meteorological station of the Seville airport. This diagram takes into account both frequency distribution and Average wind intensity. Scale in percentage point compared to the maximum. [33]

Gemasolar is located in Fuente De andalusia, in a fertile plain between Genil and Carbones river. In this location the wind direction is almost the same shown in the above graph, for sake of simplicity it has not been reported the specific wind's graph. On the other hand, the wind speed is a little bit higher.

Wind speed and direction varies with altitude. This means that wind's parameters measured close to the earth surface level, where meteorological stations are located, could not be the same at the clouds level. For this reason a lot of study has been done to outline empirical equations to forecast this phenomenon. In order to evaluate this effect, in this work, it has been chosen to use the Hellman equation.

$$v_w(H) = v_{10} \left(\frac{H}{H_{10}} \right)^a$$

where: $v_w(H)$ = velocity of the wind at the height H [m/s]

v_{10} = velocity of the wind at height h_{10} , [m/s]

H_{10} = 10 meters, a = Hellman exponent

Cumulus humilis are clouds that stays around 500-2000m; generally are classified as low clouds. Applying the above formula, it has be seen a small change in wind speed and magnitude and, for sake of simplicity, it is assumed that velocity and direction of this type of clouds are the same measured in the meteorological station.

Moreover wind plays another important role: as the wind velocity increases, the heat losses of the receiver obviously increase. The higher the speed, the greater the heat transfer coefficient of convection through atmosphere.

2.1.3 Clouds modeling: PS10

Six different clouds were chosen, all coming from the main wind direction (S-W, 220°) despite the last one(S-E, 130°). After the following descriptions there are figure 2.3 and figure 2.4 that show the evolution of the cloud on the field. The designed clouds are the following:

1. A big cloud covering all the solar field: “*total shadow S-W*”;

It has been decided to model this cloud to see how the heat flux map changes when the entire field is sudden shadowed. The main idea behind this choice is to model a cloud that affect progressively all the heliostats, firstly shadowing and then unshadowing the whole field. The wind is modeled according to the available data, hence the cloud starts to cover firstly the mirrors in the bottom left part, and lastly the ones in the upper right part. Knowing that the PS10 field has a main diameter of about 750 meters, the cloud has a diameter at least as the same size of the plant.

2. A big cloud covering the right half of the solar field: “*right shadow*”;

Heliostats behave in different ways as their position changes in respect to the solar tower. By shadowing only a part of the field it is possible to study how the shadowed mirrors really affect the heat flux map and consequently the temperature map. The solar field has been split in two sides along a line that has the same direction of the wind (S-W 220°). Right shadow means that all the heliostats that lie on the right side of that separation line are progressively shadowed.

3. A big cloud covering the left half of the solar field: “*left shadow*”;

The same consideration done on the right cloud case can be extended to this cloud. It has been decided to see the effects of a big cloud crossing on the left side of the solar plant. It is possible to identify the heliostats that most affect the operation of the receiver by doing a comparison with the previous case.

4. A small cloud crossing in the middle of the solar field: “*small shadow*”;

As already said, *cumulus humilis* clouds size can vary a lot. For this reason also smaller clouds are simulated in this thesis: the one studied is of about 200m of diameter. It is very important to understand if also a small cloud has any strong impact on the working operation of the power plant. It has been decided to simulate it in order to cross the heliostats closer to the tower, because these heliostats are the one that have the smaller image on the receiver and thus are responsible to the increase of the peak flux.

5. A long and thin cloud crossing in the middle: “*long shadow*”;

Looking at the literature no one has ever studied the effect of a cloud like this one before. But looking at the sky it is often possible to see cloud like the one modeled. So the authors of this work decided to consider also this case to simulate the reality in all its aspects, because the sky it is not always as the others depicted it.

6. A big cloud covering the entire solar field coming from Southeast: “*total shadow S-E*”.

While the southwest condition has been chosen for the main wind direction detected in Sanlúcar la Mayor, it has been selected also the S-E direction, even if it is not a dominant wind. This choice was done in order to have a wide range possible of options to study. The cloud has the same size as the one of the first case. Therefore, this time the shadowing process starts from the bottom right part.

The choice of these types of clouds was done in order to identify the most unfavorable weather conditions. In this way, it is possible to understand which heliostats most affect the energy production. Also the 6th case has been chosen to see how a different coverage of the field affects the transient behavior of the system.

Due to the fact that the clouds passage is not simulate in a continuous way, the simulation provide a temporal subdivision of the entire process in “*time-steps*”. It has been chosen to subdivide in 10 *time-steps* the progressive covering of the field. This choice has been done to have a good compromise between quality and a computational cost of the simulation.

As it can be observed from the figures 2.3 and 2.4, an irregular shape of the clouds with sharp edge has been assumed. Of course not all the 10 time step are represented in these figure but only few, in order to let the reader understand the main path of each cloud. Only the shadowing process is showed because the unshadowing process is exactly the opposite: the cloud keep maintaining its direction with the same velocity, unshadowing firstly the heliostats shadowed in the covering process.

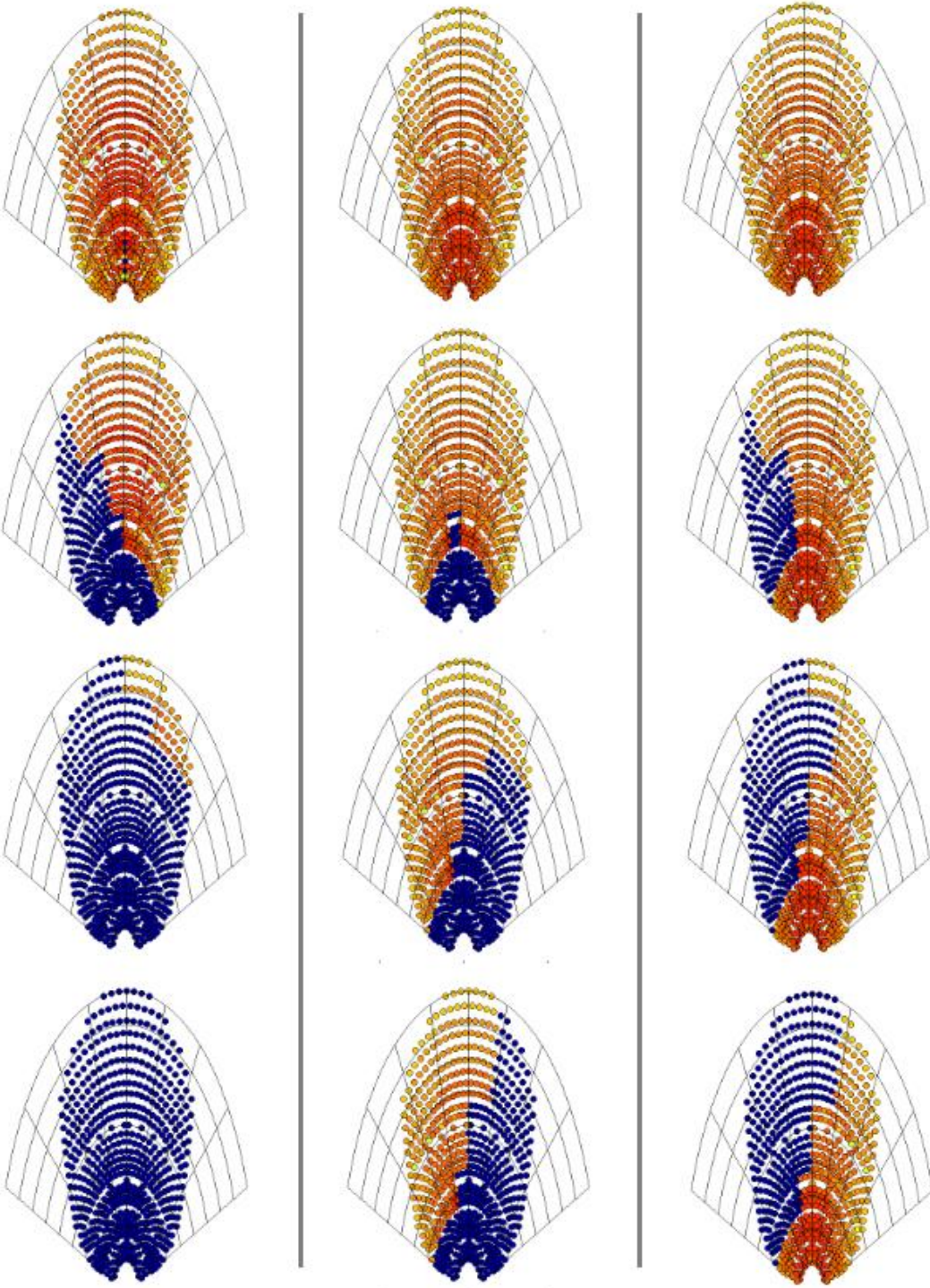


Figure 2. 3. Evolution of the shadowing on the solar field for different clouds. From left to right respectively: total shadow S-W, right shadow, left shadow.

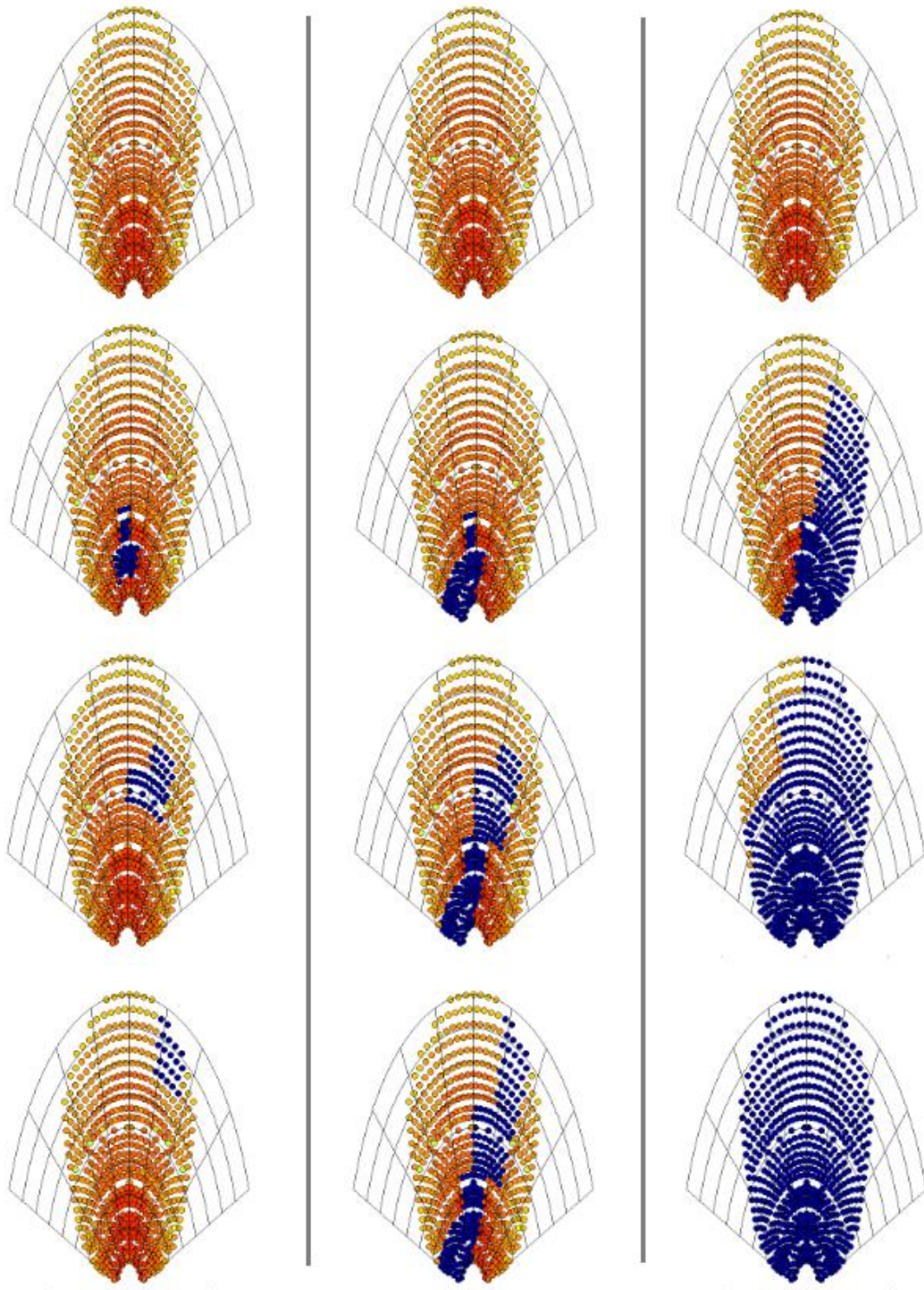


Figure 2. 4. Evolution of the shadowing on the solar field for different clouds. From left to right respectively: small shadow, long shadow, total shadow S-E.

2.1.3 Clouds modeling: Gemasolar

As for the previous case, also in the Gemasolar transient simulation it has been chosen to characterize six different clouds. In this case all the clouds come from the same direction (S-W, 220°). It has been decided not to simulate clouds coming from south-east (as done for PS10) due to their low probability of appearance, allowing the study of more significant ones. Similar clouds with different sizes have been taken into account, in order to better analyze the effects of the shadowing of high efficiency zones and to see how the field's size can mitigate the strong DNI reduction.

The chosen clouds are the following:

1. A big cloud covering all the field: *“total shadow S-W”*

As the field of Gemasolar is bigger than PS10 one, obviously a cloud able to cover the entire field has to be bigger as well. The average diameter of Gemasolar is about 1500 meters, so a cloud with the same diameter has been chosen.

2. A big cloud covering the left part of the solar field: *“left shadow”*

The field has been subdivided in two main areas with a line parallel to the main wind direction and crossing in the middle. In this case all the left part has been progressively shadowed as shown in figure 2.5.

3. A cloud big as the PS10 covering the left part of the field : *“left shadow as PS10”*

The peculiarity of this case is that the cloud has the same size of the whole PS10 plant: 750 meters in average.

This choice has been made to understand which effects the same cloud has on two different plant size. A sort of preliminary sensitivity analysis on the size of the field can be done by comparing the obtained results with the *“total shadow”* one in the PS10 case.

4. A small cloud crossing in the middle of the field: *“small cloud”*

Even if the plant size is increased, the effect of a small cloud is investigated. In this simulation the size of the cloud still remains the same of the PS10 case: an average diameter of about 200 meters.

5. Two small clouds crossing in the middle of the field: *“two small clouds”*

As the size of the field increases, also the probability to have more than one cloud crossing simultaneously the field increases. So, two side clouds are modeled, both of about 200 meters of diameter. These two clouds are about 150 meters far and cross in the middle of the field, where there are the heliostats that most affect the peak flux values on the solar receiver.

6. And a clouds big as PS10 covering the central part of the solar field: “*total shadow as PS10*”

As in the case number two the cloud has the same size of PS10 plant.

Also in this case the effect of the same cloud on two different size fields is studied, in order to understand how much the field size can affect the transient conditions considering the same shadow.

A particular choice has been done on two specific clouds (cases 3 and 6), having the same size of the PS10 solar field. This option is useful to compare how two distinct solar plants with two different sizes can be affected by the same cloud. Due to the fact that Gemasolar is much bigger than PS10 but the wind speed is almost the same it has been necessary to increase the number of time-step to 20. In this way the quality of the simulation is still good with a small increase of the computational cost and thus of the time needed to run all the simulations.

Also in this case the shapes of the clouds are irregular and the smaller clouds tend to a round shape.

In figure 2.5 and 2.6 only some time steps are showed to let the reader understand the main path of each cloud.

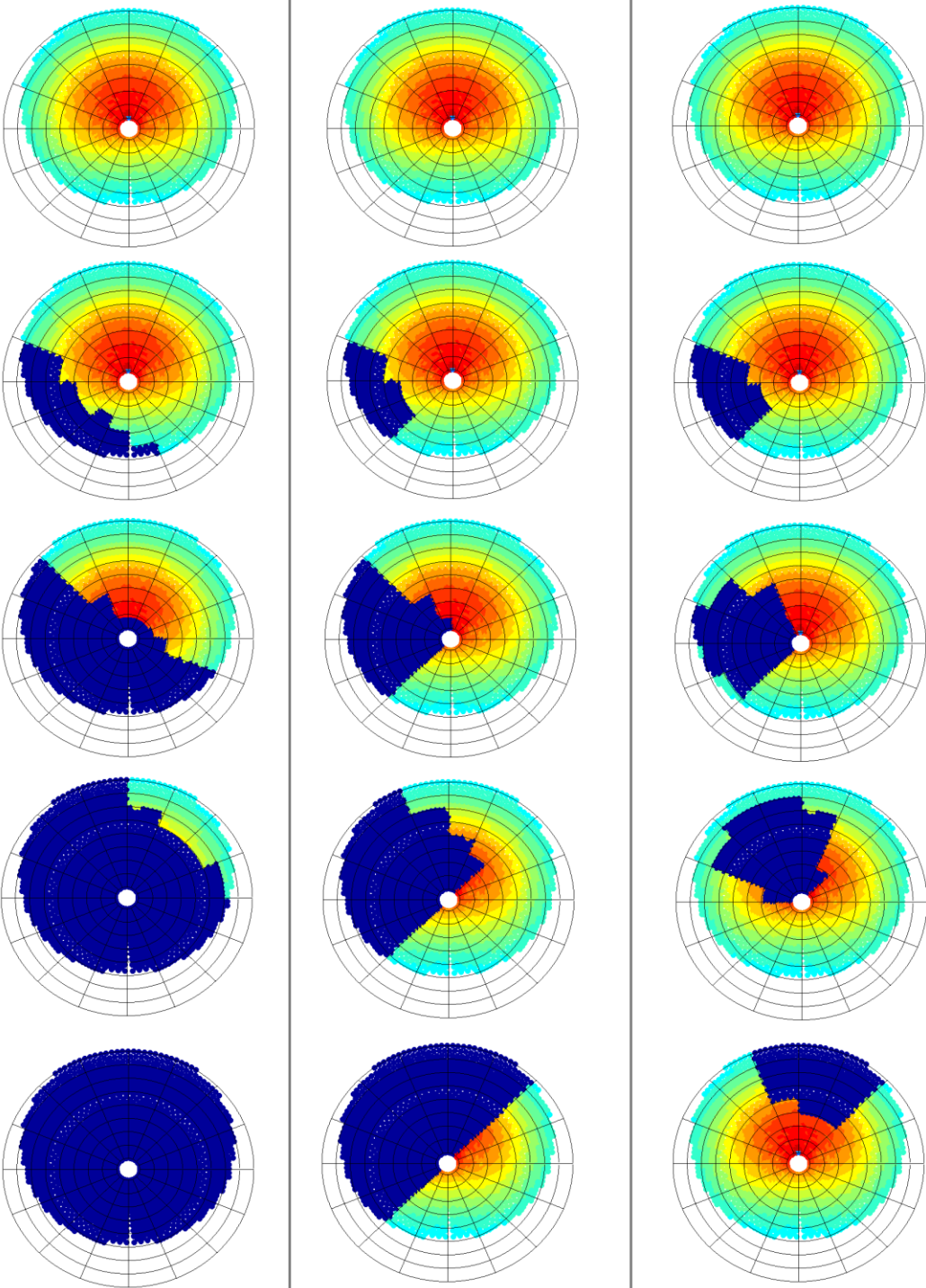


Figure 2. 5. Evolution of the shadowing on the Gemasolar solar field for different clouds. From left to right respectively: total shadow S-W, left shadow, left shadow as PS10.

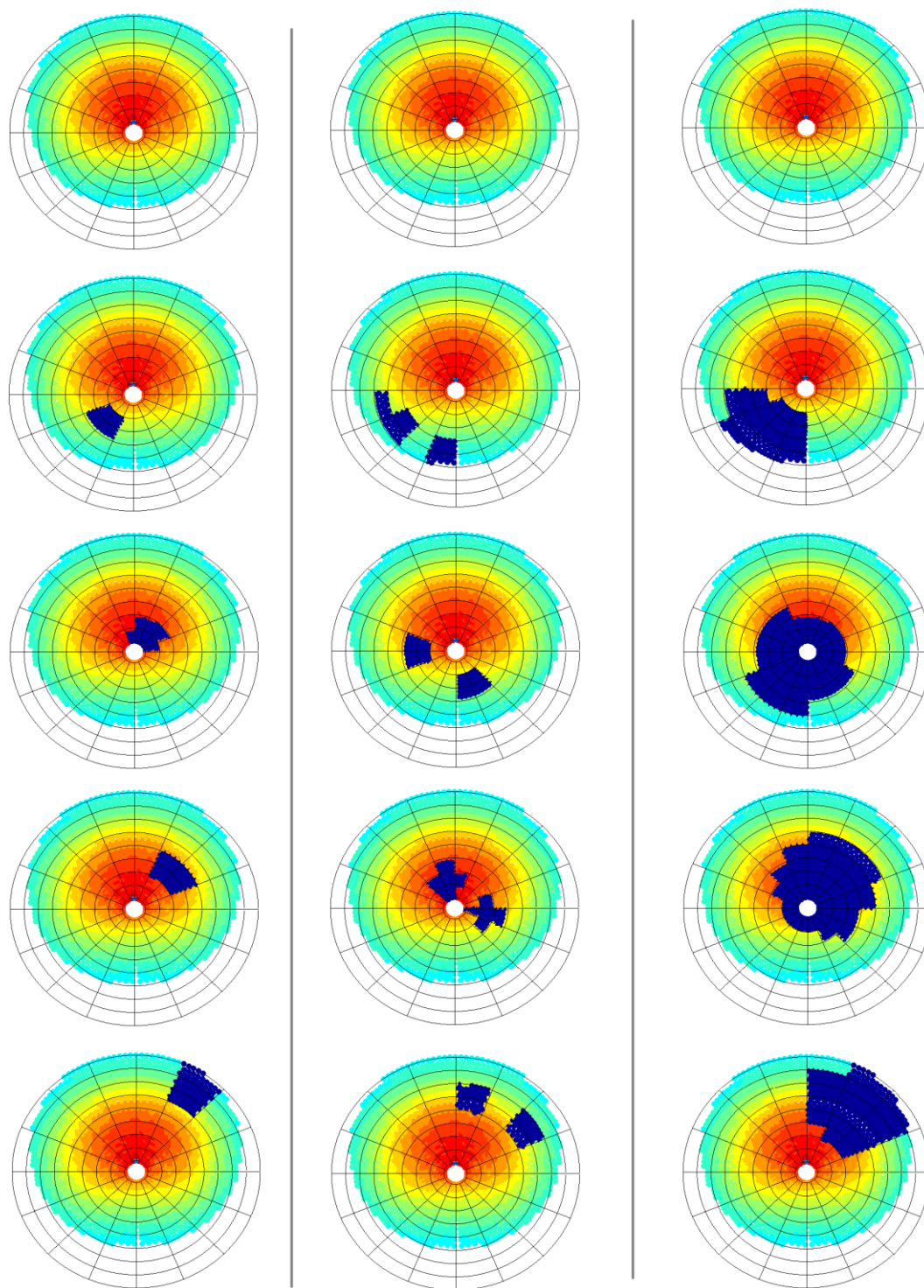


Figure 2. 6. Evolution of the shadowing on the Gemasolar solar field for different clouds. From left to right respectively: small cloud, two small clouds, total shadow as PS10.

2.2 Aiming strategies PS10

2.2.1 Previous creation of the aiming strategies

In order to allow the creation of new aiming strategies different from the default ones normally used by Delsol, a series of approximations has been made by De Giorgi [34].

First of all, a division of the solar field in zones was made, to associate a group of heliostats to the same zone and permit to set their aiming likewise. Due to the irregular layout of the field of the PS10, the easiest geometrical approximation of the latter appeared to be the section of an annulus, which brought to a radial/azimuthal division. With this supposition, different configurations of the field have been developed, from a 2x2 division to the final 8x8 one. The latter, shown in the figure 2.7, is the one used in the present work due to its good characteristics: it provides a good spatial discretization with an acceptable computational load.

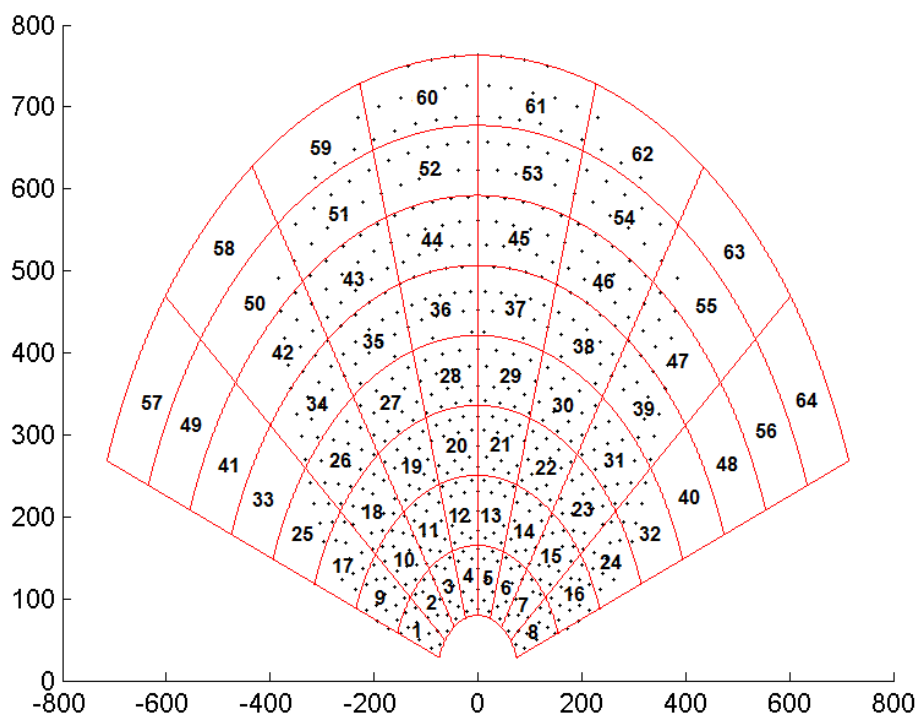


Figure 2.

7. Zone division and numeration of the PS10 solar field.

Moreover, 9 points in each panel of the receiver have been defined in order to achieve the zone aiming. The point number 5 coincides with the center of the panel, and the location of the others can be defined with the values for the horizontal and vertical displacement. The latter are eligible by the user in the program of De Giorgi, contrariwise in the present study it has been chosen the default value of 3 meters, the best for the defined aiming strategies. Further information can be found in the paragraph 4.1.3 and in figure 2.8.

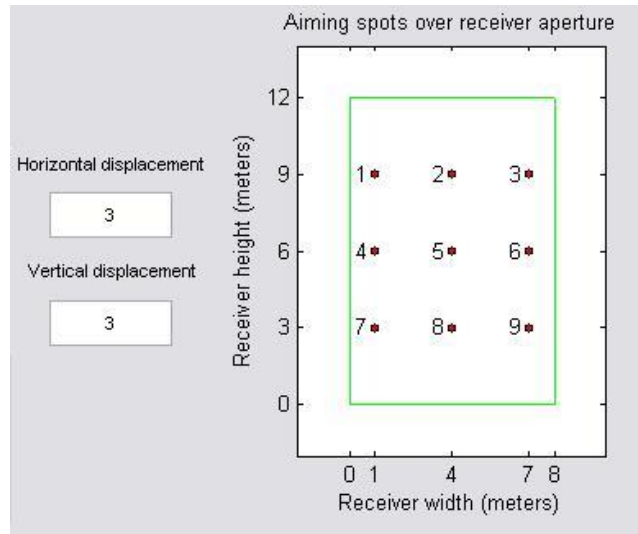


Figure 2. 8. Representation of the aiming points of the panels of the receiver.

Now it is possible to define the desired aiming strategy: associating a number from 1 to 9 to each zone, all the heliostats included in that zone will aim to the point of the receiver that corresponds to that number. If the number 0 is chosen, the heliostats will aim to a point considerably far from the receiver (100 meters higher): in this way it has been possible to simulate the shadowing of clouds, simply de-focusing the heliostats.

However, the receiver is composed by four panels attached together, and the field is theoretically divided in four sectors pointing at one panel each one. In this way, only 16 zones correspond to each panel. Starting from the west side of the field, the first sector is pointing at the panel 2e (east) to decrease cosine effect losses (see chapter 1), and so on. Nevertheless, in the representation of graphical results (see chapter 4 and 6) the position of the panels is inverted, in order to facilitate the comprehension.

An explicatory sketch is provided in figure 2.9.

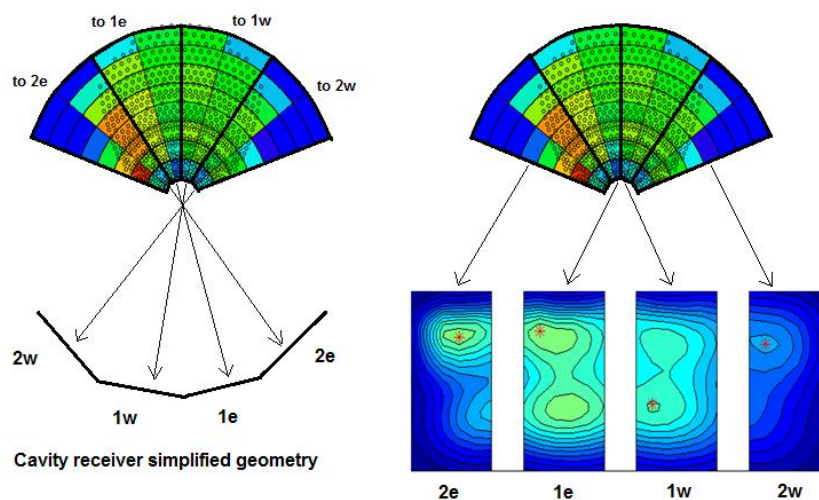


Figure 2. 9. Explication of the aiming distribution of the field.

Moreover, another aspect should be taken into account: the influence of the azimuthal and radial zone position on the image on the receiver causes a slight difference between the pointing points of the receiver defined in figure 2.8 and the real points which the different parts of the field are aiming to (figure 2.13).

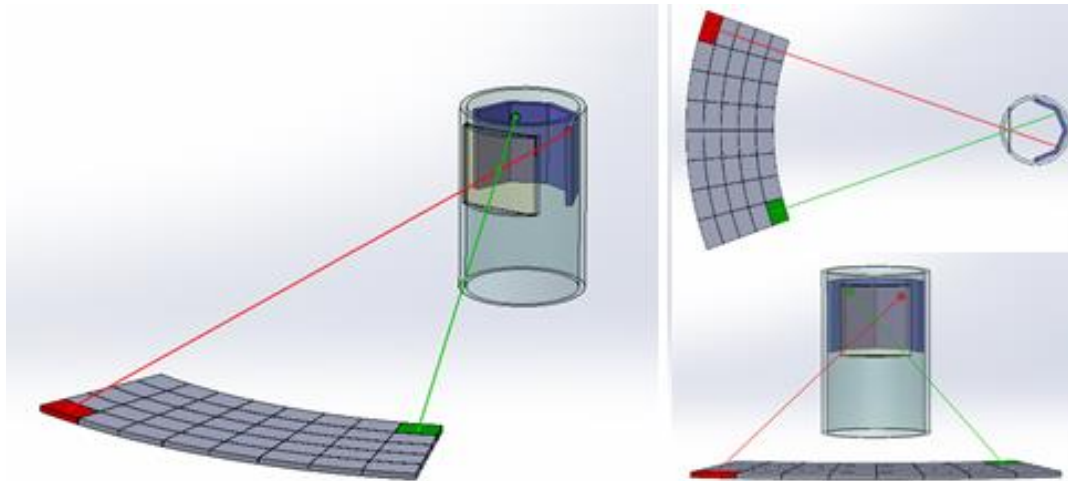
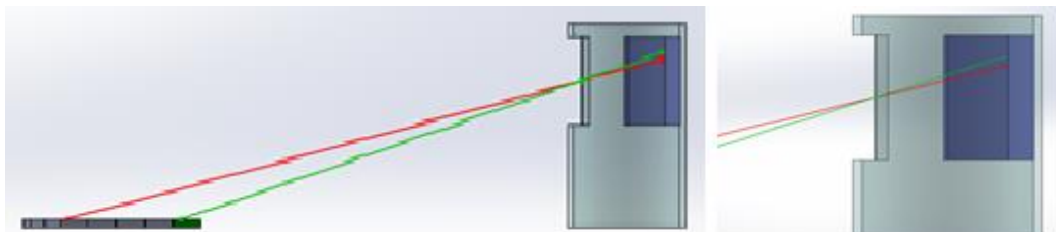


Figure 2. 10. Visualization of influence of the azimuthal zone position in the field on the image position on the receiver [34].



11. Visualization of influence of the radial zone position in the field on the image position on the receiver [34].

2.2.2 Aiming strategies adopted

First of all, the default aiming strategy of Delsol has been studied. As it can be observed in figure 2.12, this strategy consists in focusing the entire solar field at the point 5, in order not to increase the spillage losses. In fact the bigger is the distance of the heliostat from the tower, the bigger will be its image on the receiver. The result is a high concentration of heat flux in the central part of the receiver and a high value of the peak flux, which could possibly leads to the choice of more expensive materials.

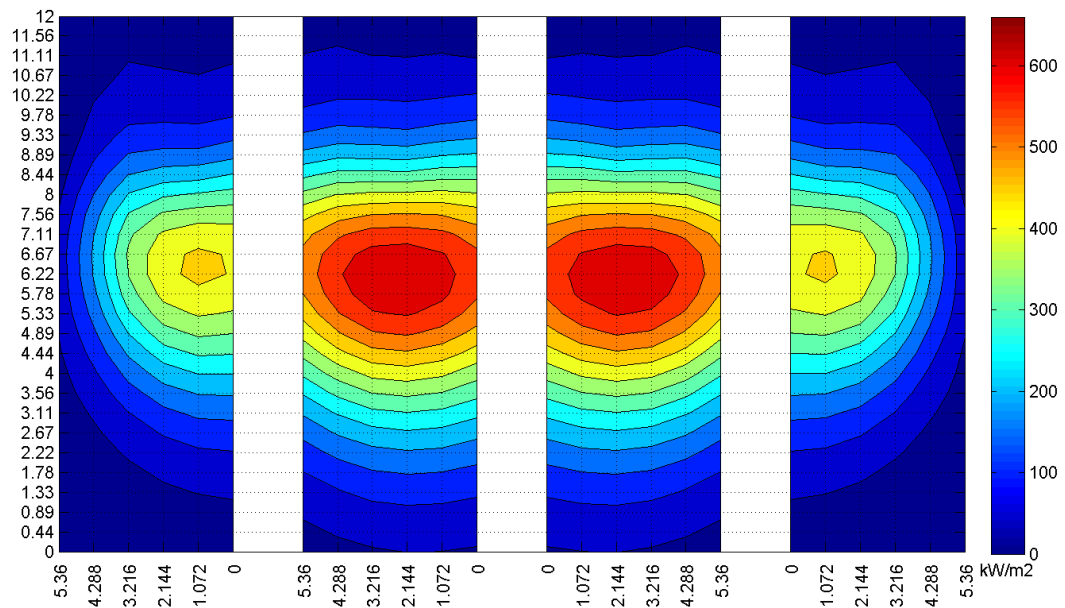


Figure 2. 12. Default aiming flux maps on the receiver of the PS10 on March 21st at noon. [34]

Secondly, after a process of development and optimization based on the evaluation of the contribution of single zone heat fluxes and in the consideration of general flux distribution and power supplied, six different effective aiming strategies has been created by De Giorgi.

Aiming Strategy 1

The idea of the strategy number 1 is to spread the image in the vertical direction to reduce the gradients and the peak flux typical of the default aiming (figure 2.12), keeping focused at point 5 the second half of the field. The peak, as it can be observed in the figure 2.13, is considerably reduced, but also the overall power obtainable decreases.

Aiming strategy 2

The second strategy tries to avoid the high concentration of the flux in the upper part, distinctive of the aiming 1. In order to do this, the rows 3 and 4 are focused at point 8, in the lower part of the receiver. This strategy provides a peak flux lower than default one but higher than the strategy 1; nevertheless, the new distribution of the heat flux permits to obtain a higher overall power than strategy 1.

Aiming Strategy 3

This strategy is the complementary of the aiming 2: the focusing of first four rows is inverted, so that the row 1 and 2 re focused at the point 8 and the 3 and 4 to the point 2. The result is an aiming strategy with a better distribution of heat flux, providing a lower peak and a small growth of overall power compared to the default aiming.

Aiming Strategy 4

This is the only strategy in which the aiming of the second half of the field is modified, focusing the row 5 and 6 to the point 2. There are no positive results, as the peak is higher than the one of the aiming 3 and the overall power is lower.

Aiming Strategy 5

This strategy starts to fully take advantage of the division in 8 rows, focusing the row 1 at the point 8 and the row 2, 3 and 4 at the point 2. This process provides an increase of the overall power and a reduction of the peak flux, showing the real way to improve the aiming strategy.

Aiming Strategy 6

This last strategy obtains a better distribution of the heat flux on the panels, spreading it in a vertical way. Row 1 and 4 are focused at the point 8 and row 2 and 3 at the point 2, achieving a strong reduction of the peak flux, along with a small reduction of the overall power compared to the aiming 5. As it can be observed in the figure 2.13, finally a good uniformity of the heat flux distribution is obtained.

The six aiming strategies are resumed in table 2.1 and in figures 2.13 and 2.14, where an overview of the characteristics of each aiming strategy is provided.

	Aim 1	Aim 2	Aim 3	Aim 4	Aim 5	Aim 6
Row 1	2	2	8	8	8	8
Row 2	2	2	8	8	2	2
Row 3	2	8	2	2	2	2
Row 4	2	8	2	2	2	8
Row 5	5	5	5	2	5	5
Row 6	5	5	5	2	5	5
Row 7	5	5	5	5	5	5
Row 8	5	5	5	5	5	5

Table 2. 1. Resume of the 6 aiming strategies. The row 1 contains the zones from 1 to 8, the row 2 from 9 to 16 and so on.

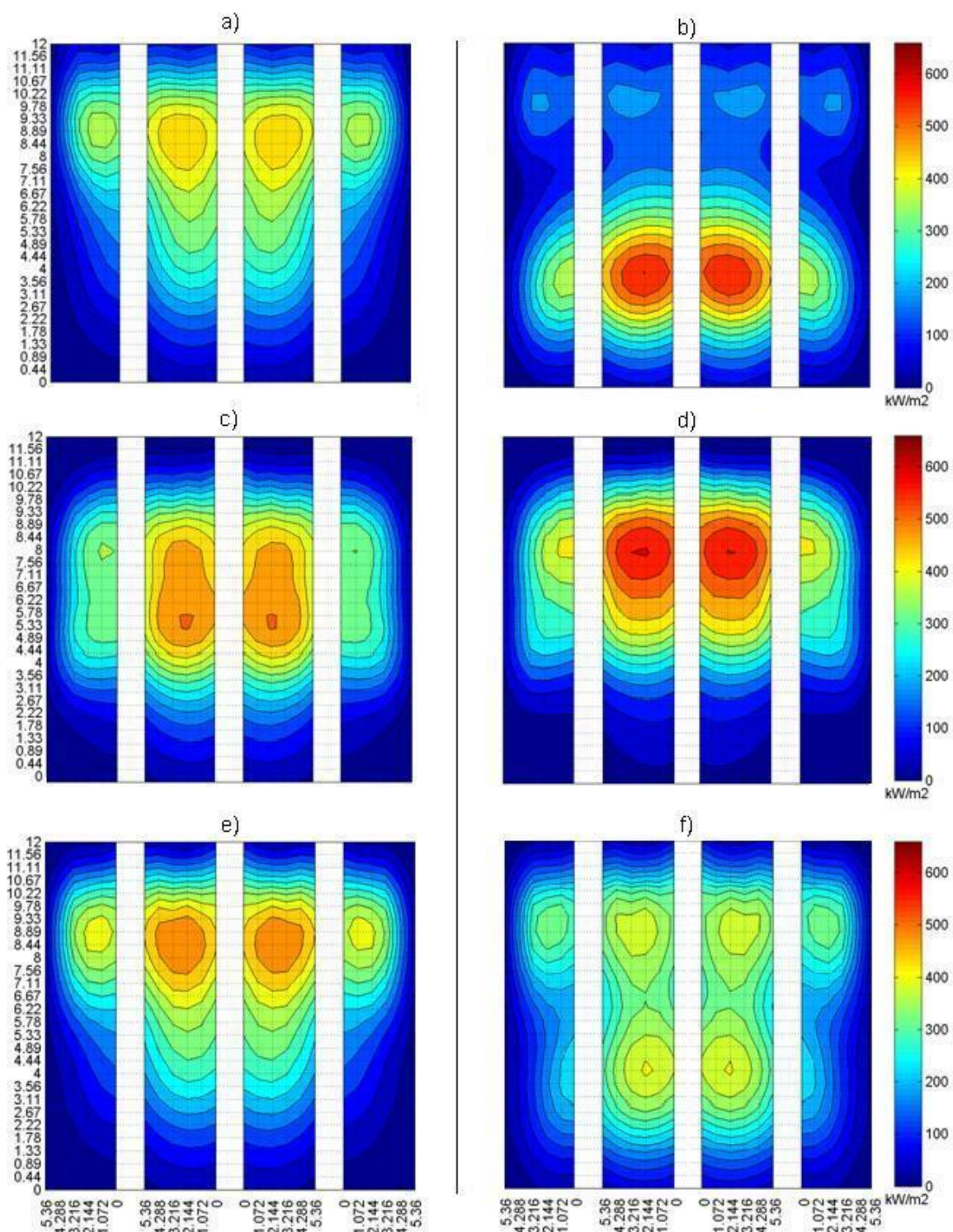


Figure 2. 13. Flux map on the receiver of the PS10, on March 21st at 12h, obtained with: a) aiming strategy 1, b) 2, c) 3, d) 4, e) 5 and f) 6.

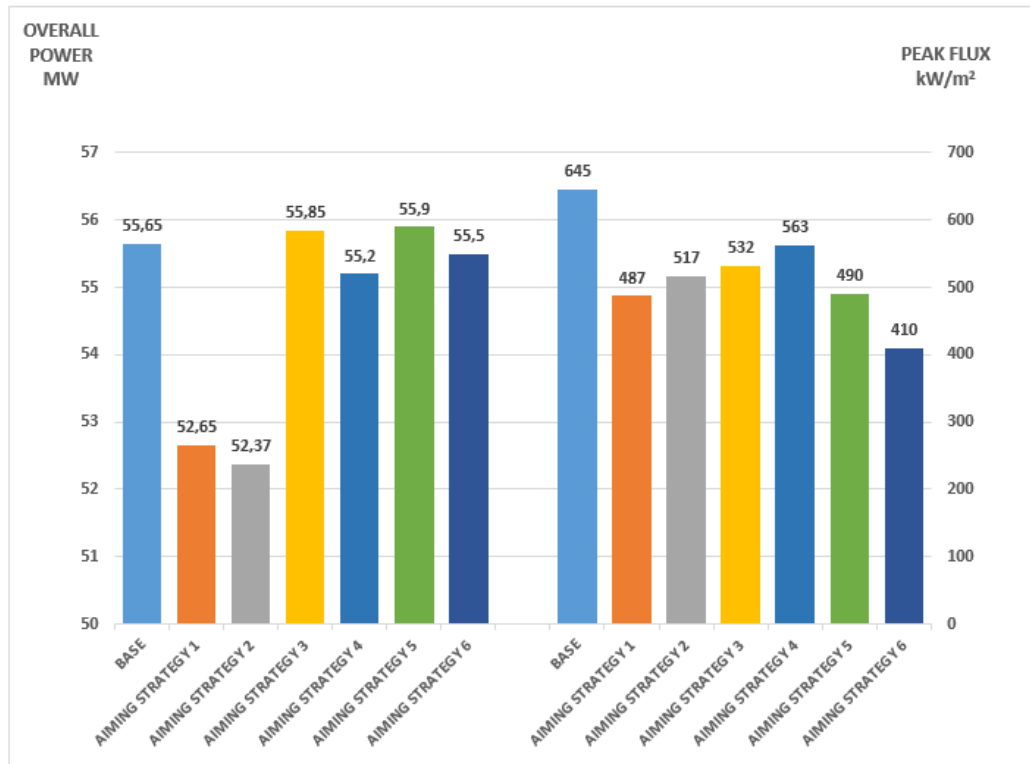


Figure 2. 14. Results obtained with the traditional aiming (base) and the Aiming Strategies.

These six aiming strategies are the departure point of the present study, due to their good characteristics and reliability. Another reason why it has been chosen to use the same aiming strategies of De Giorgi is that it would be really interesting to discover if the conclusions obtained for on design conditions are similar to the off design. In other words, if the aiming strategy 6, the best according to De Giorgi, continues to be the most favorable also during a transient condition due to the passage of clouds.

2.3 Aiming strategies GEMASOLAR

The main ideas behind the Gemasolar aiming strategies are the same of the PS10 approach. The goal is to investigate several focusing strategies of the heliostats on the receiver in order to understand which of those has the lower impact in terms of peak flux and thus thermal stresses. The greatest difference with the PS10 case is that Gemasolar has an external receiver. Its cylindrical configuration oblige to have an aiming strategy in which the radiation has to be as much perpendicular to the surface as possible, in order to avoid high incident angles and thus lower absorption of the incoming flux.

2.3.1 Previous creation of the aiming strategies

In order to create a series of suitable aiming strategies, first of all a good zone division has to be made. Instead of the PS10, in which only 64 zones have been defined, for the field of Gemasolar a division in 128 zones has been taken into account (differing from De Giorgi's choice, which subdivided it in 64 zones). The reason of this choice is due to the different

size of the fields: considering the same velocity of the wind, a greater number of time steps is needed to model Gemasolar. Moreover, the doubling in the number of zones it is necessary to increase the spatial discretization accuracy, and thus to improve clouds passage simulation. Therefore, a division in 8 rows and 16 azimuthal sectors has been created (figure 2.15).

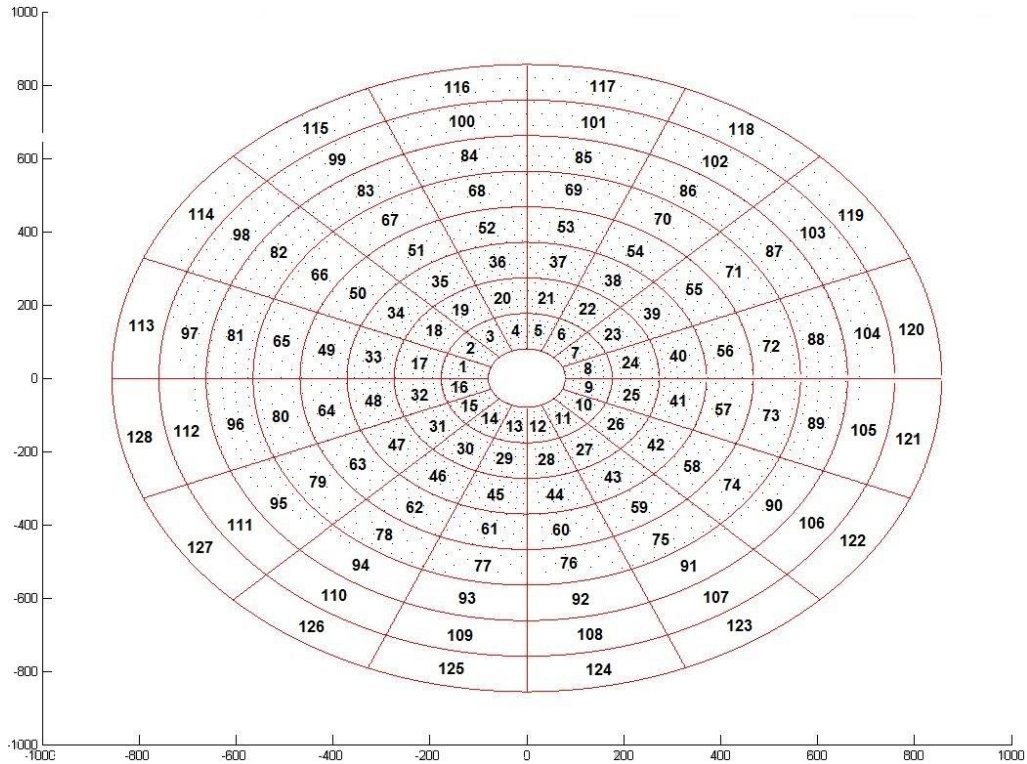


Figure 2. 15. Zone division and numeration of the Gemasolar solar field.

Moreover, 9 points on each panel of the receiver have been defined, exactly in the same way as for the PS10. Also the construction of the aiming strategy, assigning to each zone one of the 9 aiming points, is identical.

Finally, in order to allow the representation of the flux maps (for example, figure 2.16), the receiver surface it has been divided in three parts. Due to its cylindrical geometry, three sector of 120° have been defined, starting from south and continuing with clockwise direction (panels 000-120-240).

2.3.2 Aiming strategies adopted

As for the PS10 the default flux map is shown below. In this base case all the heliostat are focused in on the receiver in order to have the lowest spillage losses level.

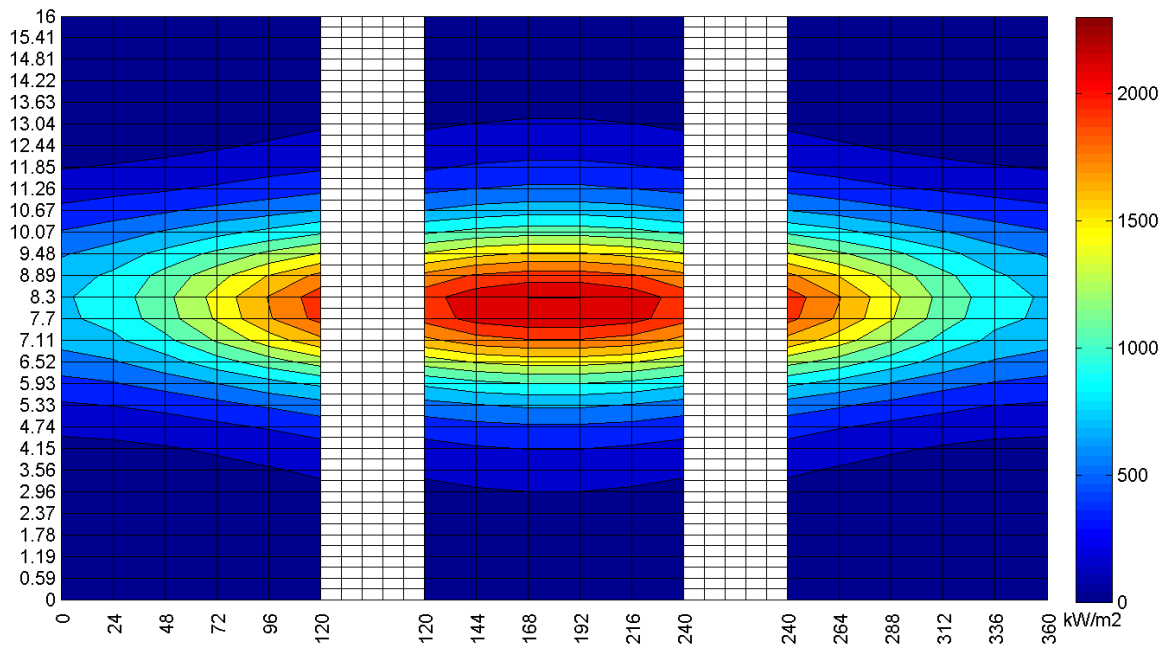


Figure 2. 16. Default aiming flux maps on the receiver of Gemasolar on March 21st at noon. [34]

Aiming strategy 1

The first strategy focus the first four rows to point 2 (higher part), while the remaining are aimed in the middle as in the base case. As results the peak flux reduces with a low variation of the total energy absorbed.

Aiming strategy 2

In this case the third and the fourth row point the receiver in point 8 (the bottom part) maintaining the first two row focused as before on point 2. Differently than PS10 case it shows a strong peak reduction with a small loss of energy. This fact is due to the different geometry of the receiver.

Aiming strategy 3

The results obtained with this strategy are almost the same of the previous case: in fact this strategy is like the strategy number two but with inverted focusing: first two row points at the bottom and third and fourth row to the top.

Aiming strategy 4

With this aiming strategy it has been evaluated how the spillage losses varies changing the focus of the heliostats far from the tower. Peak flux lowers slightly and spillage losses obviously start to increases. For this reasons in the following strategies the second half of the field will not be displaced from the center.

Aiming strategy 5

The fifth configuration, compared with the previous ones, shows a reduction of the peak flux of minor intensity but also it has the lowest energy losses. The first row is aimed to the bottom of the receiver and the following three to the top.

Aiming strategy 6

This strategy consists in focusing the first and the third row to the top and the second and the fourth to the bottom part of the receiver. It shows very low energy losses and peak reduction reaches its highest value.

Below is showed a table (table 2.2) that resumes the six different aiming strategies and a representation of each one (figure 2.17):

	Aim 1	Aim 2	Aim 3	Aim 4	Aim 5	Aim 6
Row 1	2	2	8	8	8	2
Row 2	2	2	8	8	2	8
Row 3	2	8	2	2	2	2
Row 4	2	8	2	2	2	8
Row 5	5	5	5	2	5	5
Row 6	5	5	5	2	5	5
Row 7	5	5	5	5	5	5
Row 8	5	5	5	5	5	5

Table 2. 2. Resume of the 6 aiming strategies for Gemasolar. The row 1 contains the zones from 1 to 8, the row 2 from 9 to 16 and so on.

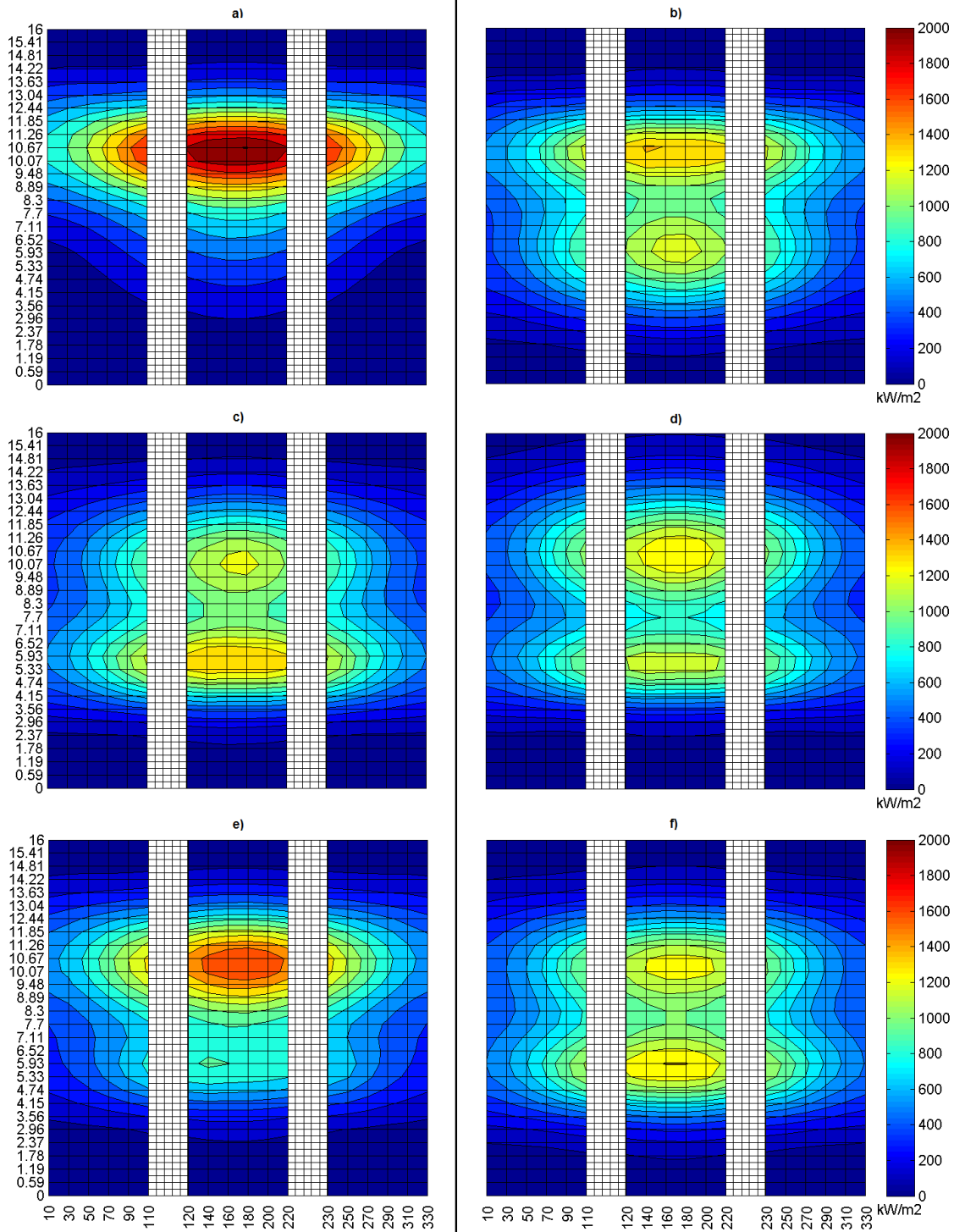


Figure 2. 17. Flux map on the receiver of Gemasolar, on March 21st at 12h, obtained with: a) aiming strategy 1, b) 2, c) 3, d) 4, e) 5 and f) 6.

In the PS10 case the difference among the 6 aiming strategies are very strong both in the variation of power and also in the peak flux. As we can see in figure 2.18, for Gemasolar it is not the same: the overall collected energy has a maximum variation of about 1% while the peak flux shows a reduction in case 6 of 40%.

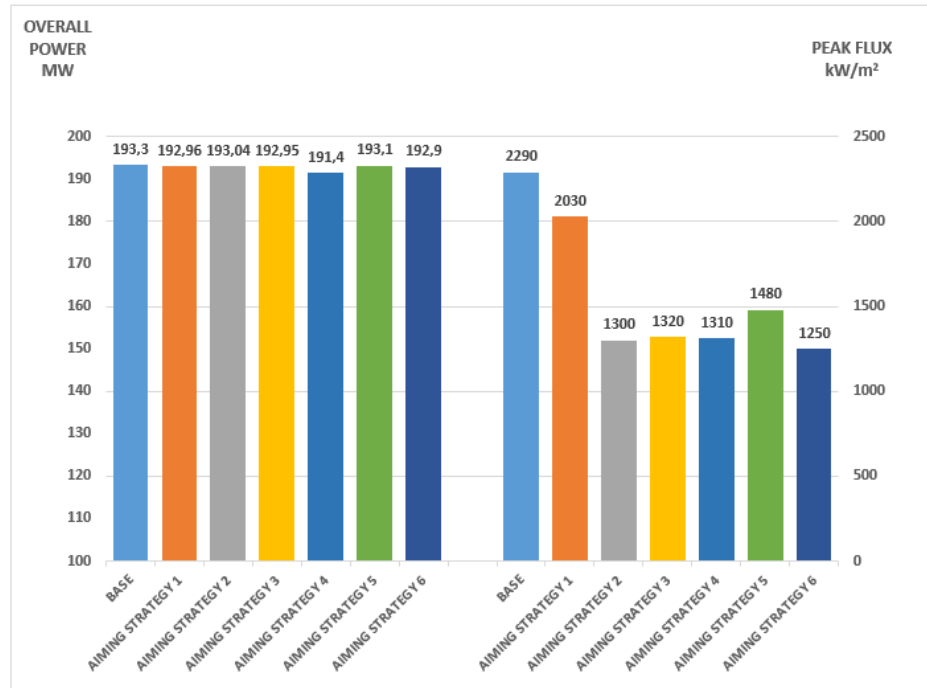


Figure 2. 18. Results obtained with the traditional aiming (base) and the Aiming Strategies, for Gemasolar.

Aiming strategy 6 appears to be the most favorable in on-design conditions also for Gemasolar.

2.4 Property of material at high temperature

2.4.1 Creep

The focus of this work is to identify which are the critical issue for a solar tower system and search solutions to reduce the effect of sudden variation of heat flux. This imply a preliminary introduction on the effects of the variations of temperature on the material of the receiver.

Mechanical properties of materials, usually determined at ambient temperature, are subject to significant changes as the temperature changes.

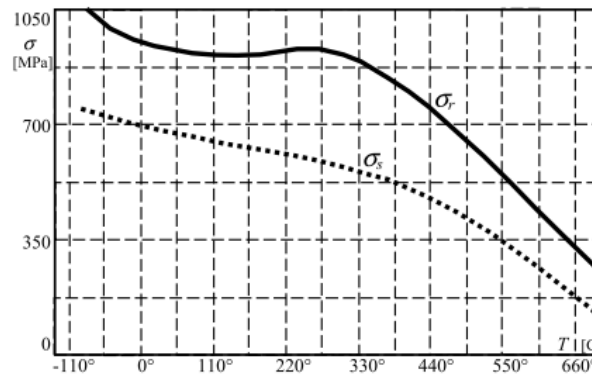


Figure 2. 19. Trend of steels' strength as temperature changes.

In figure 2.19 is shown the static properties of steel at different temperatures. The trends are representative of most of the materials: as temperature increases, tensile strength reaches a maximum value, after which it decreases very quickly.

Creep is defined as a time-dependent deformation under constant load. Usually this phenomenon is associated to a stress state at high temperature conditions. Ferrous material specimens subject to constant load for very long time at high temperature are permanently deformed even if the actual stress is less than the yield stress at that temperature. In the design stage of a system subjected to high temperature the election of the material is a key factor: high performance and expensive material.

2.4.2 Thermal expansion

As the temperature rises, in materials in solid phase, the interatomic distance increases. This implies and increases in the dimension, as shown in the following expression:

$$\varepsilon_{i=x,y,z} = \alpha_i(T - T_0) = \alpha_i\Delta T$$

where: α [$^{\circ}\text{C}^{-1}$]: coefficient of thermal expansion;

T_0 [$^{\circ}\text{C}$]: initial temperature; T [$^{\circ}\text{C}$]: final temperature.

When a sudden variation occurs, a temperature gradient is established within the component. This could imply a different dimensional contraction in different area of the element: the residual stresses generated can lead to premature failure of the component.

Resistance to thermal shock of a general material is explained by:

$$RTS \cong \frac{\sigma_r k}{E \alpha}$$

RTS is obviously proportional to the tensile strength σ_r and to the thermal conductivity k : as the latter rise, the heat dissipation capability of the materials increases reducing the temperature gradient. RTS is inversely proportional to the young modulus E . The higher E , the higher stresses at equal strain. As the last term α (coefficient of expansion) grows, also the thermal deformations increase.

2.4.3 Coating materials

A special coating material that has a selective behavior respect to the incident radiation covers the receiver's pipes. Its own optical properties, such as reflectivity, absorptivity and emissivity, change significantly as the wavelength of the radiation changes. It has to behave as close as possible to an ideal material: null reflectivity (means absorptivity=1) in the spectral range of the solar radiation, and reflectivity=1 (null absorptivity) in the thermal infrared region, with a sharp change among the two regions.

Composed materials, such as ceramic-metal, satisfy these requirements since they have a high absorptivity peak in the solar spectrum and a low emissivity in the thermal infrared region.

Chapter 3

Available Software for the required objective

In order to simulate the behavior of the chosen system, a set of software were used to develop the analysis.

3.1 DELSOL3

3.1.1 General description

The core of the simulation was done using a program developed by Sandia National laboratories (United States Department of Energy), called DELSOL3. The program, later simply called “Delsol”, was developed for specific analysis on Solar Tower power plants. This software, due to its analytical convolution approach, has a very high rapidity of execution. It also let the user free to set a very wide range of parameters: DNI variation, cosine effect, shadowing and blocking, spillage, mirror and receiver reflectivity, radiation and convection efficiency, atmospheric attenuation and piping losses [35]. Moreover also the size of the system can be chosen, such as tower height and field layout. This implies a very high flexibility thus the possibility to simulate all the kind of different solar tower power plants at different conditions.

With Delsol it is possible to develop specific analysis on a solar plant:

- Detailed model for the optical performance;
- A simpler model of the non-optical performance;
- An algorithm for the field layout through heliostats coordinates specification;
- An algorithm to find the best system design;
- Economic model for calculating energy costs.

Furthermore, Delsol can either evaluate the performance of a system previously designed by the user, or optimize a system design for a given desired power system’s characteristics.

For this work, only the first class of analysis was used, because the aim is to evaluate the performances of an already existing power system. In particular the analyzed design is the Spanish commercial plant PS10, presenting a north field and a single cavity receiver.

Delsol is relatively easy to use. With a minimal input, Delsol can simulate a very wide range of different systems.

3.2 Delsol limitations

The biggest issue is that it is not user friendly. It does not have a user interface, and the input file is a formatted file, created by the user, which contains all of the Namelist input data required to run a specific job. A very strictly format criteria must be respected, such as spacing between variables and Namelist order. Moreover, it is necessary to store all the files related to each single calculation in a specific folder with the executable file written in a text format.

Each Namelist is composed by many variables, each one with a particular grammar, meaning, range and a default value. For this reason, it is very complicated to correctly set the input for a specific case of study and the users' manual must be consulted many times [34].

&NLFLUX	CAMPO SOLARE PS10
iflx=1	624 35
ifxout=1	1 9
iflaut=3	0.0 86.8
xfc=2.47	21.4 84.0
yfc=-3.17	42.7 75.4
zfc=2.5	59.8 61.2
polf=90.	73.6 44.1
azmf=157.5	-73.6 44.1
nxflix=6	-59.8 61.2
fazmin=-2.68	-42.7 75.4
fazmax=2.68	-21.4 84.0
nyflix=28	2 10
fzmin=-6.	12.8 98.2
fzmax=6.	37.0 91.1
/	58.4 79.7
&NLEFF	76.9 61.2
/	89.7 39.9
	-89.7 39.9

Figure 3. 1. Extract from an input text file of Delsol.

Delsol give as output another formatted file, which contains all of the standard output from a Delsol's execution. Delsol only writes, and does not read, this file [36]. This aspect is the most critical because the results are not immediately understandable by the user. It appears as another formatted file with an ordinated list of parameters. There are no graphical displays and thus no direct visualization of the results. This forces the user to set a further investigation to understand Delsol's outcome.

```

THE 35 ROW CONTAINS 7 HELIOSTATS

IND. HSTAT NO.= 618 ROW = 35 EAST = 0.00 NORTH = 763.00 RADIUS= 8.14THT, RANGE = 8.20 THT, REC. AZM = 0.00 ELV= 83.00
DAY HOUR AZ ANG EL ANG COSINE SHADOW BLOCK ATM TRANS SPILLAGE TOTAL NO.X AIM NO. Y AIM 1ST X AIM 1ST Y AIM
355.00 -3.00 -20.9 77.7 0.932 1.000 0.959 0.922 0.903 0.655 1 1 0.00 0.00
IND. HSTAT NO.= 619 ROW = 35 EAST = 44.20 NORTH = 761.60 RADIUS= 8.14THT, RANGE = 8.20 THT, REC. AZM = 3.34 ELV= 83.00
DAY HOUR AZ ANG EL ANG COSINE SHADOW BLOCK ATM TRANS SPILLAGE TOTAL NO.X AIM NO. Y AIM 1ST X AIM 1ST Y AIM
355.00 -3.00 -22.5 77.6 0.922 1.000 0.968 0.922 0.903 0.654 1 1 0.00 0.00
|

FLUX CALCULATION|
UNITS OF FLUX ARE KILOWATT/SQ. METER
THE FLUX IS CALCULATED FOR DAY= 355.00 HOUR= -3.00 INSOLATION= 0.829 KW/M2
HI(M) HORIZONTAL DISPLACEMENT IN FLUX PLANE(M)

-2.680 -1.608 -0.536 0.536 1.608 2.680

6.000 0.457E+02 0.641E+02 0.599E+02 0.525E+02 0.571E+02 0.620E+02
5.556 0.707E+02 0.944E+02 0.916E+02 0.818E+02 0.892E+02 0.926E+02
5.111 0.110E+03 0.141E+03 0.141E+03 0.132E+03 0.134E+03 0.131E+03
4.667 0.152E+03 0.192E+03 0.198E+03 0.191E+03 0.188E+03 0.176E+03
4.222 0.200E+03 0.249E+03 0.262E+03 0.257E+03 0.244E+03 0.220E+03
|

```

Figure 3. 2. Extract from an output text file of Delsol.

In order to study a particular behavior of a system several simulations must be run. This obliges the user to change, each run, the input file and store it in a proper folder.

Furthermore, every output must be interpreted. This fact makes the study even more difficult.

In this thesis, the focus is to identify correct aiming strategies to find out the best performance of the existing field. Exploiting Delsol's features, it must be set the vertical and horizontal displacement for every heliostat, but it is very challenging for the extremely high number of mirrors and for the reasons above seen.

Moreover, it would be very tough to deduce from the Delsol's outputs which aiming strategy improve the transient behavior of the studied system.

At the end, it is possible to say that Delsol is a very powerful program but has many issues to be solved in order to exploit its great potentiality.

3.2 De Giorgi's software proposals

In the work developed by De Giorgi, two main logical solutions to face this problem were found out:

3.2.1 First solution: Microsoft Office Excel interface

The main feature of this program is the tabular form. It allows the clear and intuitive visualization of the input and output data while the macro programming permits the automatic, and thus fast, execution in background of the majority of the commands.

Three main worksheets were created in order to manage input, output and flux map image. Moreover, four main macros were set up.

The first allows the user to set, in an easy and ordered way, all the input variables needed for the calculation. Once set all the input, the execution of the macro creates a text file respecting all the format criteria (such as spacing and format criteria) readable by Delsol.

The second one, once selected, runs Delsol, performing all the calculation.

The third is the macro for the output date: it simply stores each line into a cell of a dedicated worksheet.

The last generates a graphical visualization of the flux map of the receiver. It reads the output, imports each flux value into a cell and, depending on the value, associates a proper color. This macro, moreover, performs further evaluation such as total power collected from the panels and highlights the peak value of the heat flux on the receiver.

There is also a fifth macro that, once selected, runs all the four macros together, to speed up the calculation.

With this work, De Giorgi achieved several advantages, such as faster setting of all the inputs and automatic execution of Delsol. Moreover a graphical representation of the results allows a much faster interpretation of the outputs coupled with the calculation of new significant values from Delsol results.

As De Giorgi outlined, in his work the use of the interface showed some weak points:

- The execution of Delsol is slow due to the not optimal compatibility between VBA (visual basic for applications) and the external programs;
- The graphical representations are limited and the evaluation of further parameters is restricted;
- The overall interface is easier to use than Delsol but it is still not "user friendly".

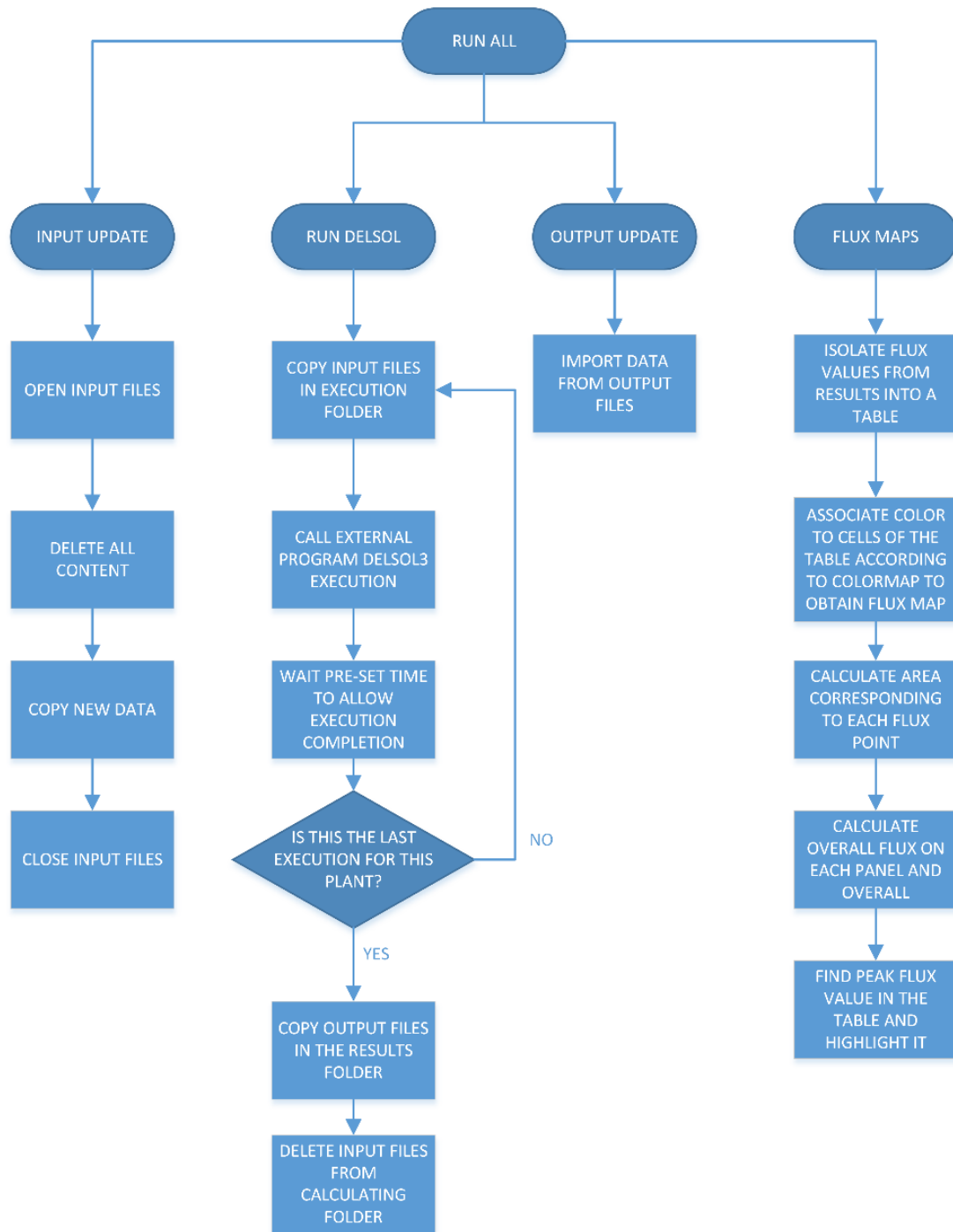


Figure 3. 3. Macros operation scheme.

3.2.2 Second solution: Mathworks Matlab interface

As just outlined, excel interface is a good step forward for the usage of Delsol, but is not enough for the purposes of the work. The main issues are related to the excessive amount of data to input for aiming strategies assessment on real field. For this reason, De Giorgi developed another interface using Mathworks Matlab to create a tool for zone definition. This lets the user to access to a direct and intuitive user interface, with a graphical interactive display.

Matlab provides a tool, called GUIDE, which let the user create a graphical display, called Graphical User Interfaces (GUIs), in which a set of control button, called components, can be designed.

These allow the user to perform different interactive tasks:

- Read and write data files;
- Accomplish any type of computation;
- Communicate with other GUIs;
- Display data as table or as plots.

The GUIDE allows a fast graphical creation of the layout of a GUI through the choice of different default component: push buttons, axes, tables, etc. The latter can be positioned and shaped in a predefined window.

To each component of the GUI it is automatically assigned a code file containing an empty function that will answer to a user interaction. Obviously the user must write the code lines defining the required operation.



Figure 3. 4. Main De Giorgi's GUI.

In the figure 3.4 it is possible to see the main GUI created by De Giorgi. The more important task achievable are:

- Selection of the type of the plant: this execute the branch of the code related to the selected option;
- Browse the input path and thus choose which day of the year simulate;
- By clicking on “modify input”, a second GUI is opened (figure 3.5). In this window is possible to modify the input table in order to change parameters arbitrarily. A “help” button helps the users in the comprehension of the parameters. By selecting another button, “zone aiming”, the GUI showed in figure 3.6 is opened. This is the most important achievement done in the De Giorgi’s work. It allows to subdivide the real field in different zone. Each zone is composed by different number of heliostats, depending on the geometry of the field. The main idea is to aim every heliostat, belonging to the same area, to the desired point on the receiver. When a zone aiming is changed this allow to apply it to every heliostat composing the zone. This is the most important aspect developed in the De Giorgi’s thesis because it achieves the goal to simplify the use of Delsol. This GUI, after the user’s interaction, compiles and saves automatically the required txt file of Delsol and speeds up the process without the need to manually insert all the inputs.

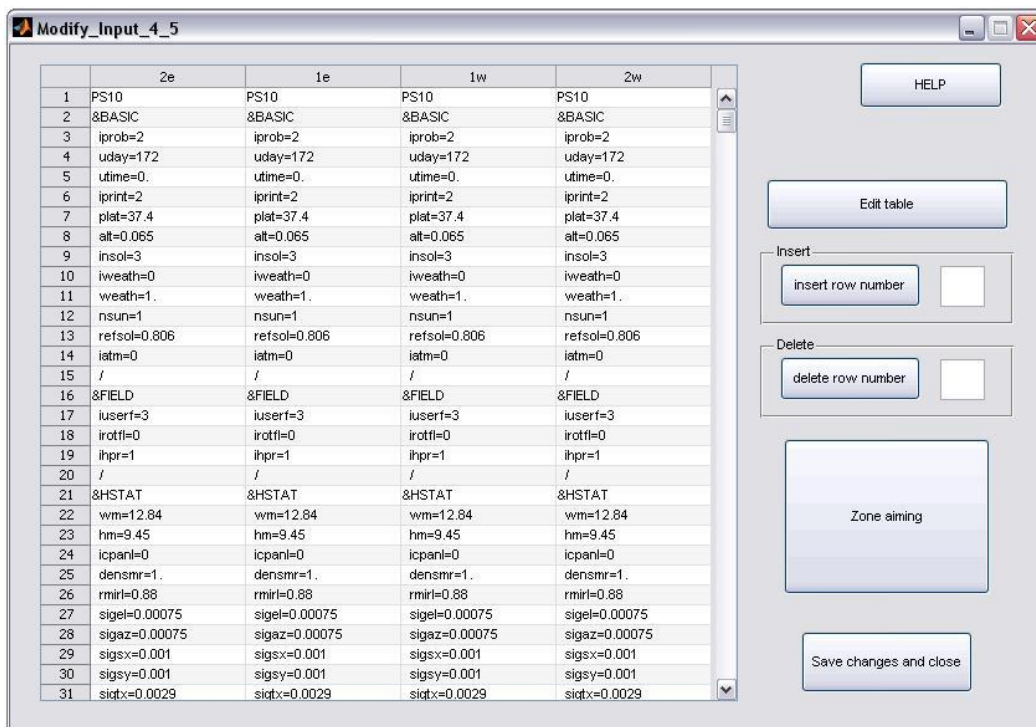


Figure 3. 5. GUI for input parameters modification.

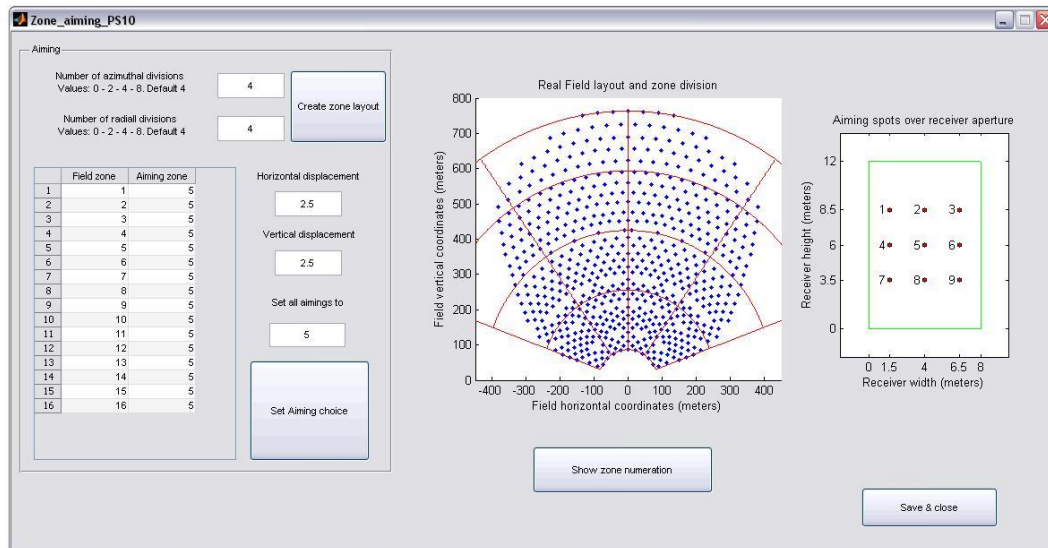


Figure 3. 6. GUI for setting aiming strategy and field layout subdivision.

On the upper left part of figure 3.6 it is possible to choose the number of zone and thus the field layout division (4, 8, 16, 64 zones) depending on the user's need. This choice is graphically displayed in the central part of the GUI. The table on the left part allows the user to insert the aiming points on the receiver aperture and assigns it to each field zone. On the right part, it is possible to visualize the receiver points and setting the horizontal and vertical displacement of the aiming points.

In conclusion, it is now possible for the user to associate to each zone a specific aiming point, by writing numbers in a table.

When the "save and close" button is pushed, Delsol input file are created and stored in a temporary folder. Back in the main GUI, it is now possible to run Delsol.

After a few seconds need by the program to run the calculation, it is now possible to push the "import output" button, where the results of interest are shown (see figure 3.7)

The table in the upper part shows the heat flux calculated, while the lower one displays the power values collected by each panel, the overall power and the peak flux.

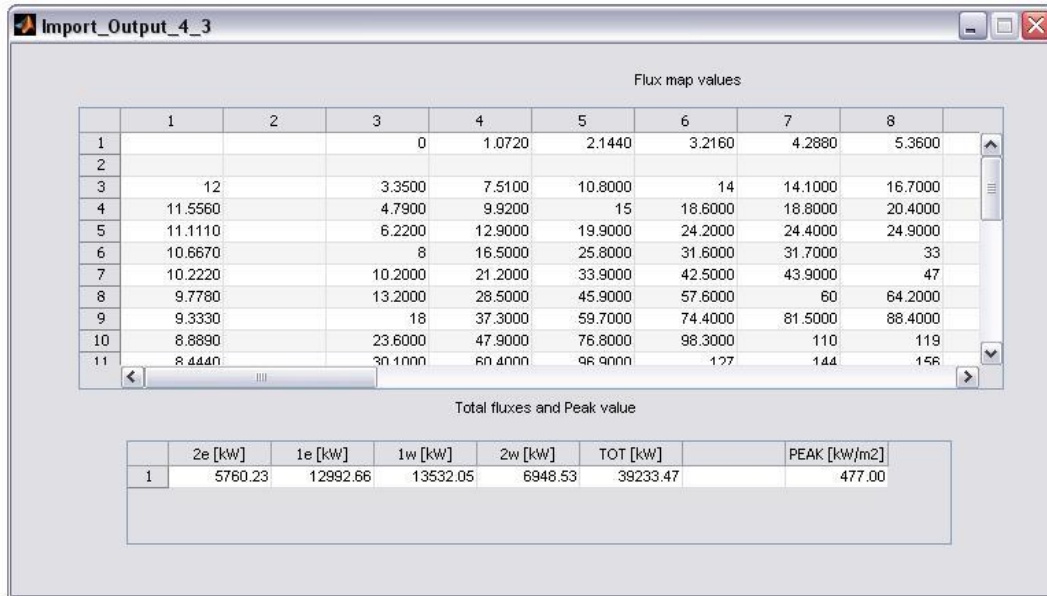


Figure 3. 7. GUI for graphically display output.

3.2.3 Graphical display

By pushing on the “flux maps” button, three different graphical representations on the results appear. Below only the two most significant are shown.

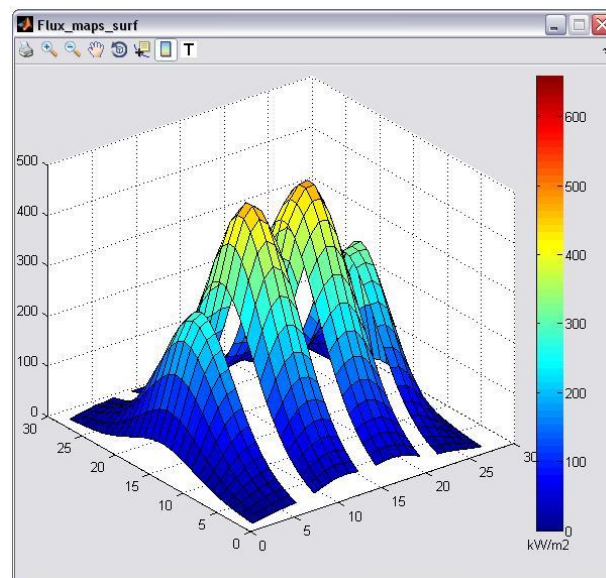


Figure 3.8: Example of Surf Map

Figure 3.8 shows a 3-D graph obtained with the “surf” function. In this way a 3-D graphical representation lets the user to visualize the value of the heat flux. On the x and y axis are stored, respectively, the x and y position of the heat flux; while on the z axis is stored its value. To better understand the graph, a Colormap is associated to the heat flux value.

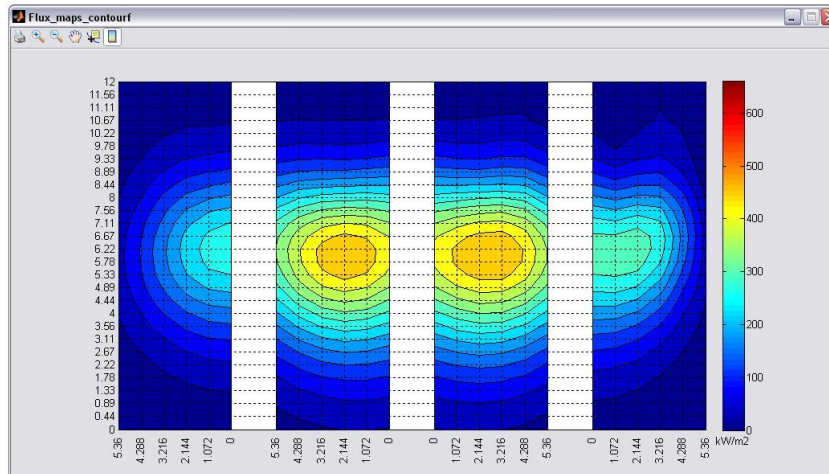


Figure 3.9: Example of *Contour Map*

Using the “contour” command, the figure 3.9 is created by Matlab. Through this map it is possible to visualize a 2-D Colormap of the heat flux in each point of the receiver. A series of iso-lines separates the zones of the receiver presenting the same value of heat flux.

3.2.4 Limitations and weakness

With his thesis, De Giorgi developed a way to simplify the use of Delsol in order to exploit in an easier way the great potential of this program. He was able to couple it with Matlab and developed a user friendly interface. Faster evaluations of the considered systems are achieved due to predefined input and graphical displayed output.

With the present work, more features are developed starting from De Giorgi’s idea. Moreover, some weak points have been improved:

- The weakest point was the input: in was possible to browse only three days of the years, all simulated at midday. To choose another hour, the user had to change the table of the input in the GUI showed in figure 3.5. This passage is not user friendly at all because require the knowledge of Delsol’s input Namelist;
- The choice of the aiming strategy had to be done manually each time setting, for each zone, the aiming point on the receiver. It is a very long procedure and the risk to make a mistake is very high;
- The output, such as peak flux and power available, was plotted in a table without the possibility to memorize it in a worksheet (e.g. excel). This lack restrict the possibility to do further studies on different simulations and to compare different conclusions.

All the improvements and the new idea worked out in this thesis are explained in chapter 4.

Chapter 4

Software Development

In this chapter an explanation of the program and of the obtained results it is provided, with all the suppositions and simplifications done.

4.1 Explanation of the principal interface

Following the main idea of De Giorgi's work, a MatLab *GUI* interface has been adopted, as it can be seen in the following figure:

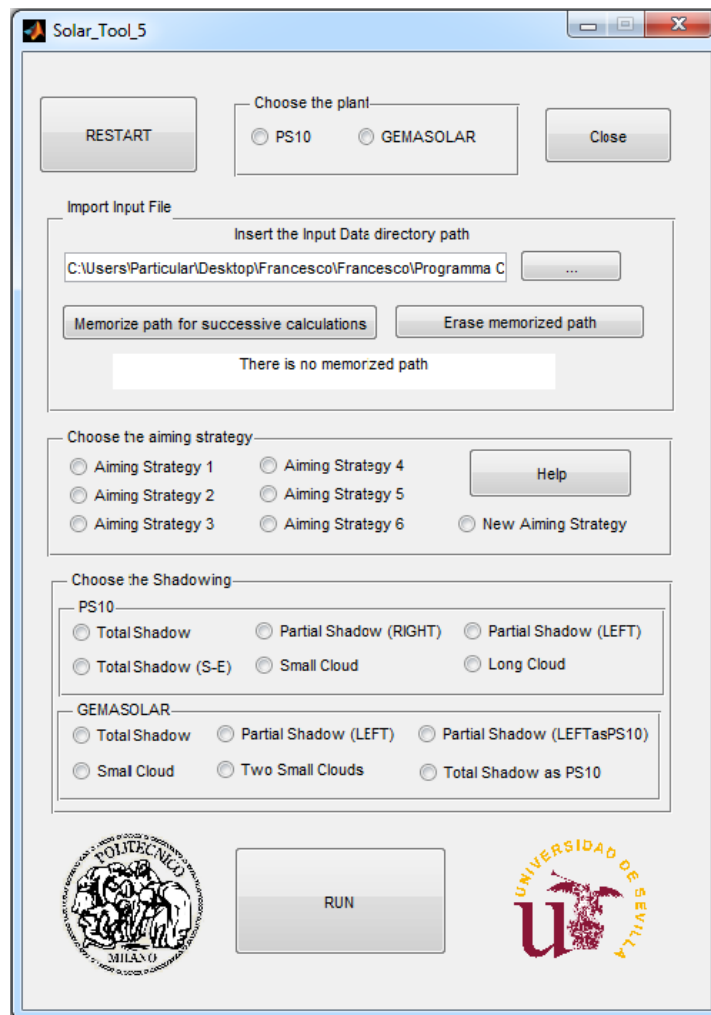


Figure 4. 1. Principal interface of Solar Tool 5.

In order to simulate the off design conditions of the two plants, it has been decided to focus on different cases: several clouds have been modeled and different aiming strategies have been used. It follows the explication of each section of the interface.

4.1.1 Choice of the plant

Maintaining the same structure of De Giorgi's code, first of all the user can choose which kind of plant is going to be analyzed: PS10 or Gemasolar. This division is automatically maintained by the program for the "Aiming Strategy" section, but not for the other ones: the user has to pay attention to choose the right input path and type of shadowing. Nevertheless, this process is immediate and intuitive, and moreover an efficient system of helps and alerts is included.

4.1.2 Import Input file

First of all, it have been chosen nine "input path" correspondents to three characteristic days in the year, for three different hours each one. These days are solstice of winter (21th of December), the solstice of summer (21th of June) end the equinox of spring (20th of March), at 9 a.m., 12 a.m. and 15 a.m. It is possible to choose the preferred input path by the browse button connected to the INPUT folder in the main directory. The input path, used directly by Delsol, is a txt file and it is possible to change manually the day and the time modifying the variables *UDAY* and *UTIME* in the Delsol's Namelist *BASIC*.

UDAY represents the number of the day starting from the 1st of January; *UTIME* fixes the hour of the day considering 12 a.m. as zero, negative in the morning and positive in the afternoon. The resume of these parameters for the different days is showed in the next table:

MAR			JUN			DEC		
9 am	12 am	15 am	9 am	12 am	15 am	9 am	12 am	15 am
UDAY			UDAY			UDAY		
80	80	80	172	172	172	355	355	355
UTIME			UTIME			UTIME		
-3	0	3	-3	0	3	-3	0	3

Table 4. 1. Resume of UDAY and UTIME parameters for the different inputs

In this section it is possible also to save the selected input path for further calculations, and obviously to delete the one previously saved.

4.1.3 Choice of the aiming strategy

In this section it is possible to choose among six already existing aiming strategies, described in the chapter 2.

In the help section a briefly description of the aiming strategies is provided, in order to let the user fully understand its meaning and permit a favorable choice.

Moreover, it is also possible to edit a new aiming strategy thanks to a second interface called "New Aiming Strategy". As the figure 4.2 shows, the user simply has to insert in the table the desired point of the receiver in correspondence of the desired row and then save the changes. Automatically all the heliostats of that row will aim to the chosen point. This feature it could be really useful, if changes to default strategies have to be done or if the user wants to create a brand new aiming.

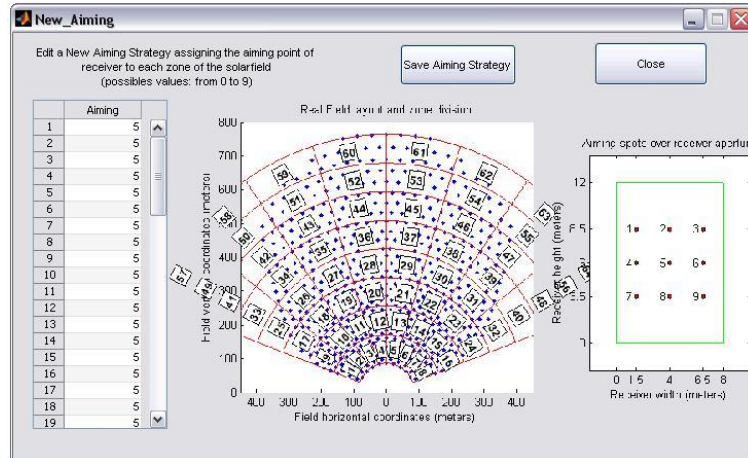


Figure 4. 2. Image of the New Aiming Strategy GUI for PS10.

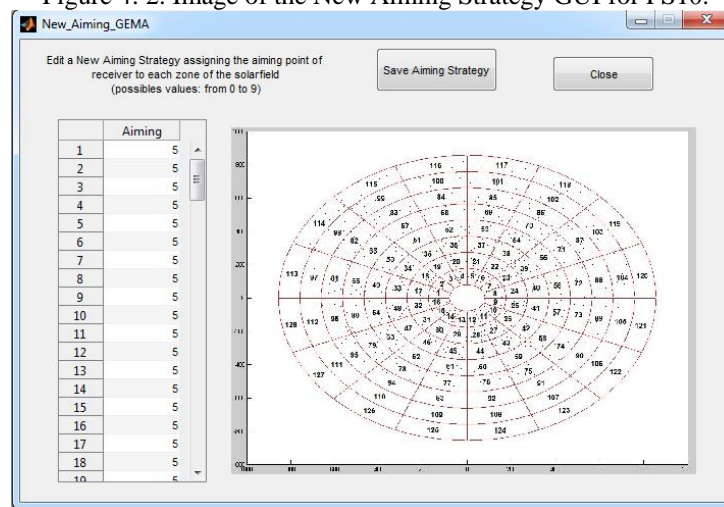


Figure 4. 3. Image of the New Aiming Strategy GUI for Gemasolar.

With the zone division created by De Giorgi, a few zones are empty because of the geometry of the field. Obviously assigning a point of the receiver to these zones does not affect to the calculation because no heliostat is detected in them, so this fact does not result to be a problem. Moreover, like already explained in chapter 2, a default value for the horizontal and vertical displacement of the point of the receiver is set. This default value was the result of an optimization process of the considered aiming strategies. It may be necessary to change it if the brand new strategy results to be really different from the other, in order to reduce possible spillage losses.

4.1.4 Choice of the shadowing

In this section it is possible to choose the cloud that is going to cover the solar field between 6 existing types, already explained in chapter 2, for each type of plant. The help section contains also a short explication, in order to permit to the user to fully understand the meaning of each shadowing.

4.2 Overall structure of the code

Once that an input path, an aiming strategy and a type of cloud are chosen by the user, it is finally possible to run the calculation. Pushing the RUN button, the code automatically executes Delsol and provides two main results: a series of graphical results and a large amount of numerical results.

It would be quite useless to completely explain the whole Matlab code, due to its length and complexity. Therefore, a brief and explicatory resume it is provided.

In the calculation block, first of all the code copies and saves all the input txt files (one for each panel) contained in the INPUT folder into a temporary folder used for the calculations, called TEMP4COMPUTING, in order not to permanently modify the input path. Without this precaution, Delsol in the following step would not be able to recognize and work on the input, modified after the first execution of the program. After that, the program modifies the input contained in TEMP4COMPUTING, attaching the chosen aiming strategy with a series of *sscanf/ssprintf* functions. Now the input file is ready to be executed by Delsol, which produces its correspondent output. Then follows the *import output* stage, where the code reads and copies the required results such as the thermic flux on the receiver and the global efficiency of each heliostat. After that, all the maps and graphs are created and automatically saved in the correspondent destination in the RESULTS folder. The entire process is made for each time step of the selected shadowing.

For each combination of input path, aiming strategy and type of shadowing it is automatically created a sub-folder, in order to simplify the storage and the accessibility of the results.

As already explained, the program calculates a series of numerical results in each time step, in order to make possible the construction of all the graphs explained in the following paragraph and also to consider other aspects of this work. These results are saved in a particular excel file created by Matlab, with a special disposition that facilitates the comprehension and the composition of recapitulatory diagrams. Obviously, this process has been made for each aiming strategy and for each type of shadowing.

To simplify the storage and the accessibility of the results, the excel file carries the name of the input path chosen (for example: June 9h) and it is formed by 6 different sheets. Each sheet contains the results for a given type of shadowing and each variable is calculated for the 6 aiming strategies. Therefore, the recapitulatory diagrams represent the profile of the considered variable during the 10 time steps, for each aiming strategy.

4.2.1 Graphical results

In order to facilitate the reading and not to overload the text with a huge amount of figures, only examples of PS10 results are included here. Nevertheless, the explication of the results both for PS10 and Gemasolar is provided in chapter 6.

For each time step, the program creates the six different graphs contained in the following section.

- *Surf map*: already explained in the chapter 2, this is a 3D graphical representation of the incident thermal flux in each point of the receiver and it presents also a colorbar to simplify its reading. The main avail of this diagram is that it is immediately understandable by the

user: it results really simply to identify where the overall peak flux is and which is the most irradiated panel.

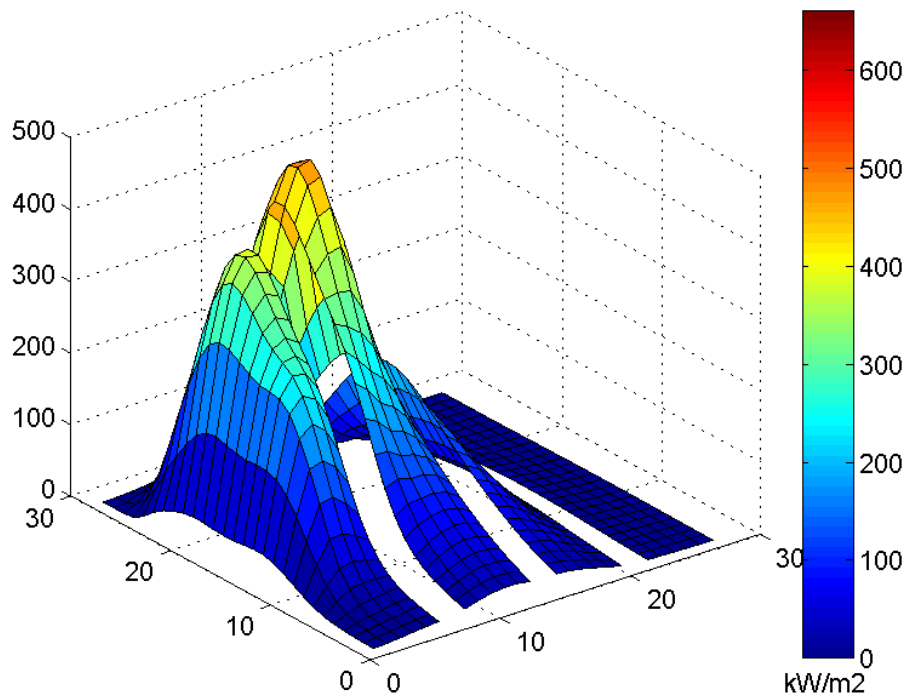


Figure 4. 4. Surf Map of the 7th time step of the passage of a big cloud covering only the right half of the solar field (aiming strategy 4, June 12h). The panel 2w is completely devoid of irradiance, the peak flux is located in the 1e.

- *Contour map*: this diagram consists in a 2D map of the heat flux for each point of the receiver. It includes a colorbar and a series of lines that separate zones with the same value of the heat flux. Basically, represents the same thing of the surf map but with different properties: the exact position of the peak flux in each panel results to be easier to identify. Moreover, a great avail of this graph is that it very understandable the difference between the different aiming strategies, reminding the location of the aiming points of each panel.

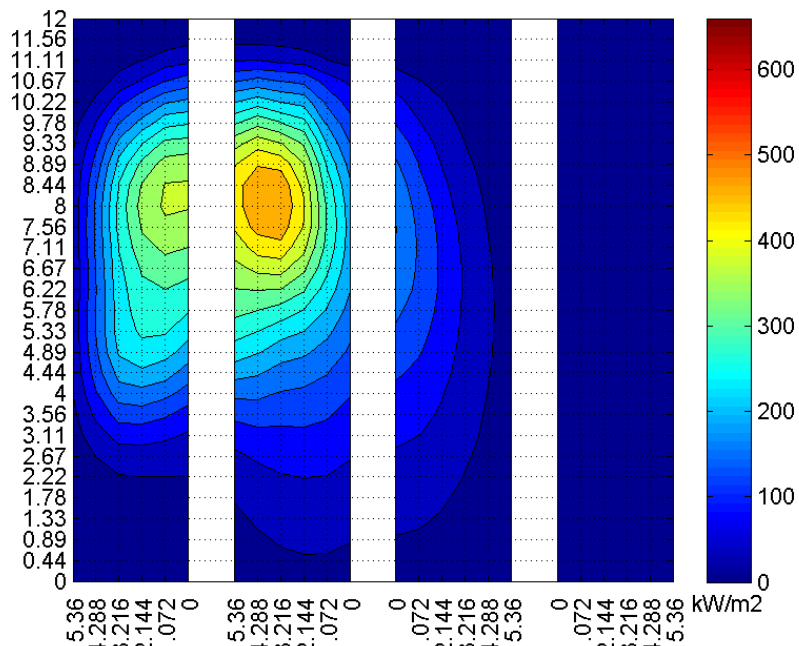


Figure 4. 5. Contour Map of the same situation of figure 4.3. The different approach of the two graphs is perfectly understandable.

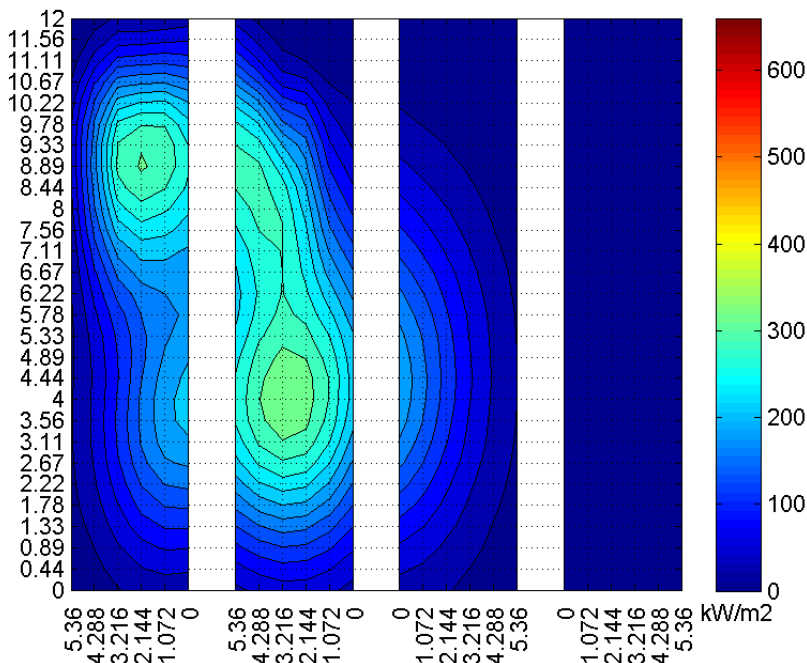


Figure 4. 6. Contour Map of the same situation of figure 4.4, except for the aiming strategy (here it is used the number 6).

- *Gradient map*: in order to analyze the thermal stresses, it has been taken into account also the spatial gradient of the heat flux in the receiver. It has been calculated the gradient for each point and also an special graph has been created. The latter is composed by different elements: first of all, the iso-lines of the contour map are drawn, in order to give a reference of the distribution of the heat flux; secondly, for each point a small arrow representing the gradient is plotted (with the Matlab function *quiver*), as well as the

maximum value of the gradient, pointed out with a star. The arrows are a good manner to represent the gradient vector, due to the presence of a direction and a verse. The intensity of the gradient in each point is proportional to the length of each arrow. The result is a quite user-friendly graph, that allows to visualize the gradient of the heat flux together with its distribution, providing a way to compare the position of the peak flux and the maximum gradient.

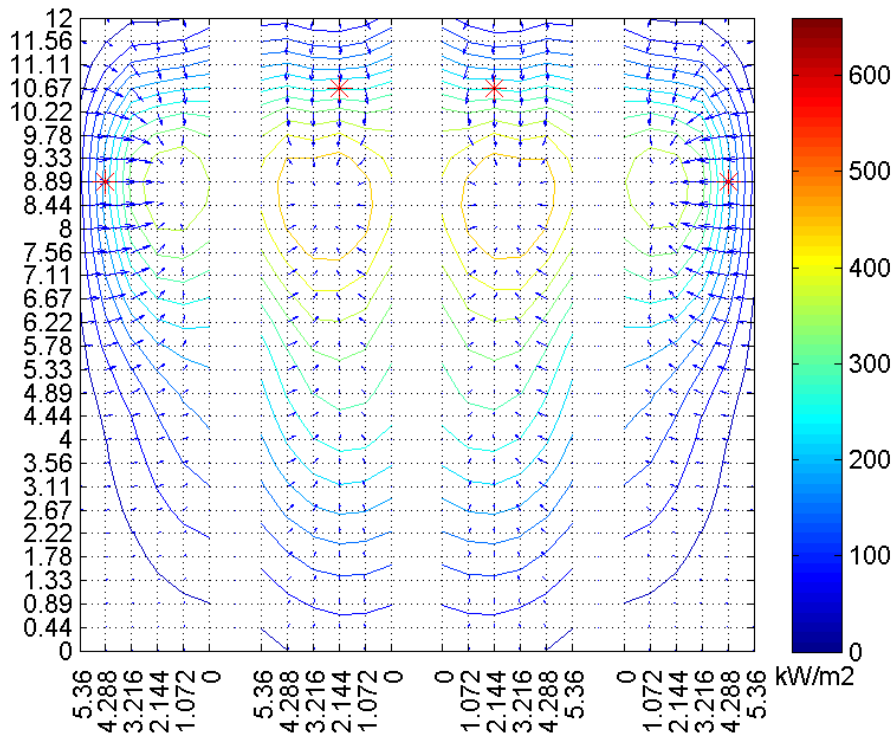


Figure 4. 7. Gradient Map of June 12h using the aiming strategy 5 in on-design conditions.

- *Solar field by zones*: this graph consists of the plot and the scatter of all the heliostats forming the entire solar field. The heliostats are represented as black points, and the division in 64 zones is provided as well, in order to show approximately the number of heliostats that belong to each zone. Moreover, each zone presents a different color, proportional to the heat flux coming from that zone. Actually, it is not representing the true heat flux, but a *heat flux factor*. This factor is defined as the ratio between the heat flux coming from a zone, calculated as the sum of the heat fluxes of all its heliostats, and a maximum heat flux. The latter is the maximum value that a zone can provide with the DNI of the days selected for this work and with the solar field of the PS10, and it results to be 13,4 kW/m² (25 kW/m² for Gemasolar). It has been chosen to use this factor in order to simplify the comparison between all the different inputs. This qualitative graph loses meaning if studied singularly, but defining a maximum common value and comparing different situations it is possible to better understand the behavior of the field during the passage of cloud. For this reason, the possible values go from 0 to 1.

This graph represents the amount of heat flux coming from each zone, showing the ones that are contributing more. Further information and explications are available in the chapter 5.

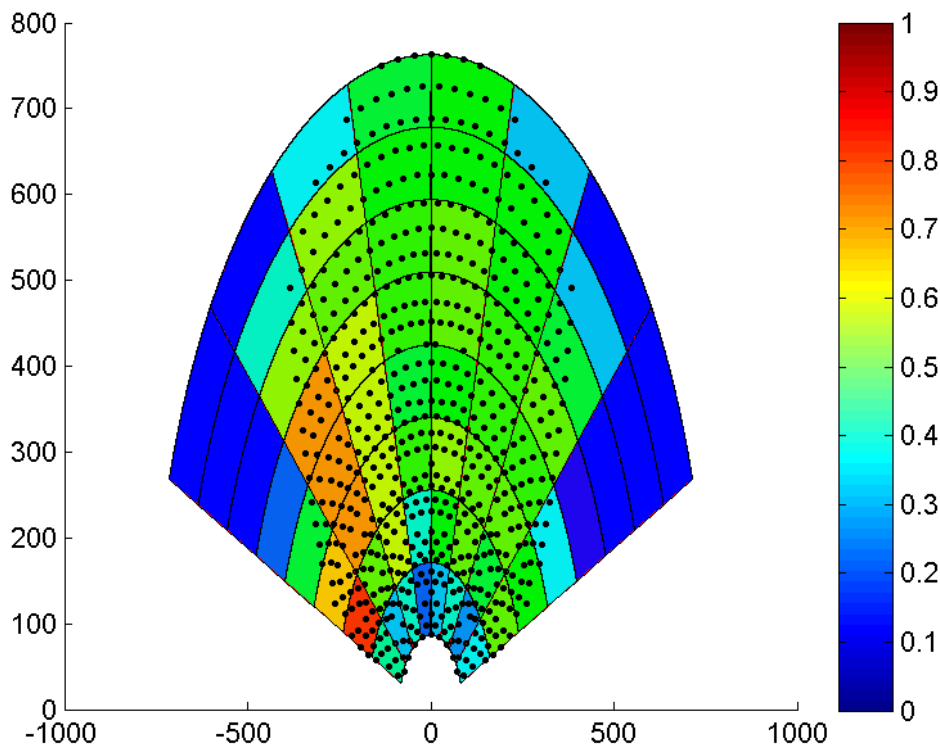


Figure 4. 8. Solar field by zones graph for the input path June 9h in on-design conditions.

- *Solar field by heliostats*: similar to the previous one, this graph represents the global efficiency of all the heliostats of the solar field. The latter is obtained from the output of Delsol and includes all these factors: cosine effect, shadowing and blocking, the atmospheric transmittance, optical effects due to elevation and azimuthal angle and the spillage effects. The following figure shows an extract from the output of Delsol, with the efficiencies for the first heliostats of the first row: the global efficiencies are calculated multiplying *spillage* and *total* ones (in fact, *total* only includes cosine effect, shadowing, blocking and the atmospheric attenuation).

DAY	HOUR	AZ ANG	EL ANG	COSINE	SHADOW	BLOCK	ATM TRANS	SPILLAGE	TOTAL NO.	X AIM NO.	Y AIM	1ST X AIM	1ST Y AIM
80.00	0.00	0.0	39.4	0.999	1.000	1.000	0.980	0.889	0.767	1	1	0.00	0.00
80.00	0.00	-7.1	39.1	0.996	1.000	1.000	0.980	0.911	0.783	1	1	0.00	0.00
80.00	0.00	-14.7	38.4	0.985	1.000	1.000	0.980	0.964	0.820	1	1	0.00	0.00
80.00	0.00	-22.0	37.0	0.968	1.000	1.000	0.980	0.997	0.833	1	1	0.00	0.00

Figure 4. 9. Extract from the output of Delsol.

The importance of this graph is that it shows the most efficient heliostats, their position and the presence of special areas of high/low efficiency. Moreover, it is very interesting to see how these characteristics change during the year, for different days and times.

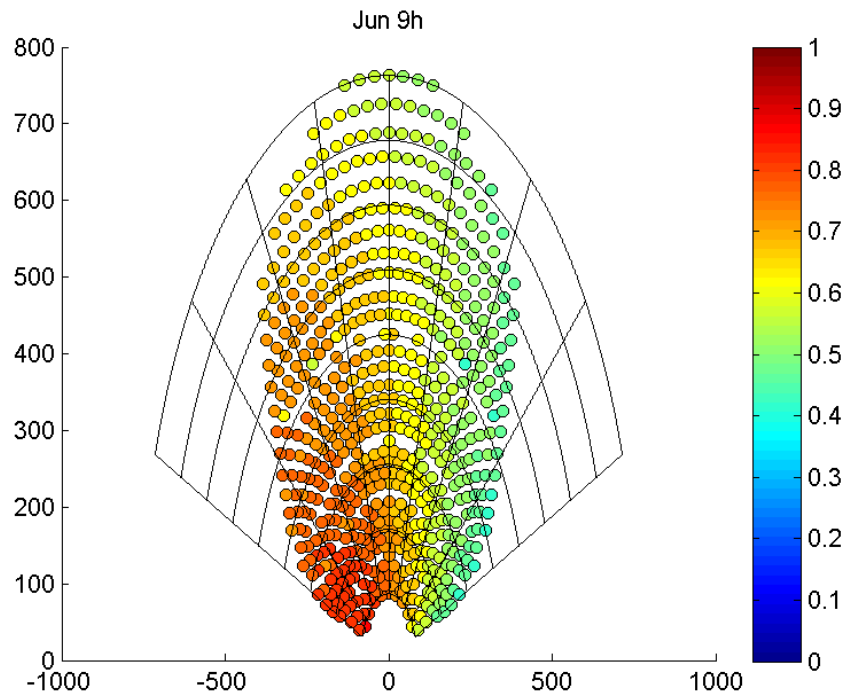


Figure 4. 10. Solar field by heliostats graph for the input path June 9h in on-design conditions.

- *Mixed plot*: consists of two graphs already explained, the *Solar field by zones* and the *Contour map*, attached together in one plot. The aim of this action is to find an answer to the move of the peak flux in the receiver for different time steps, studying it simultaneously with the evolution of the heat flux coming from the solar field. As it will be explained in the chapter 5, this graph results very useful also to represent the global evolution of the heat flux due to the passage of clouds: the user can physically see the cloud passing over the solar field, and at the same time the change in the heat flux can be observed.

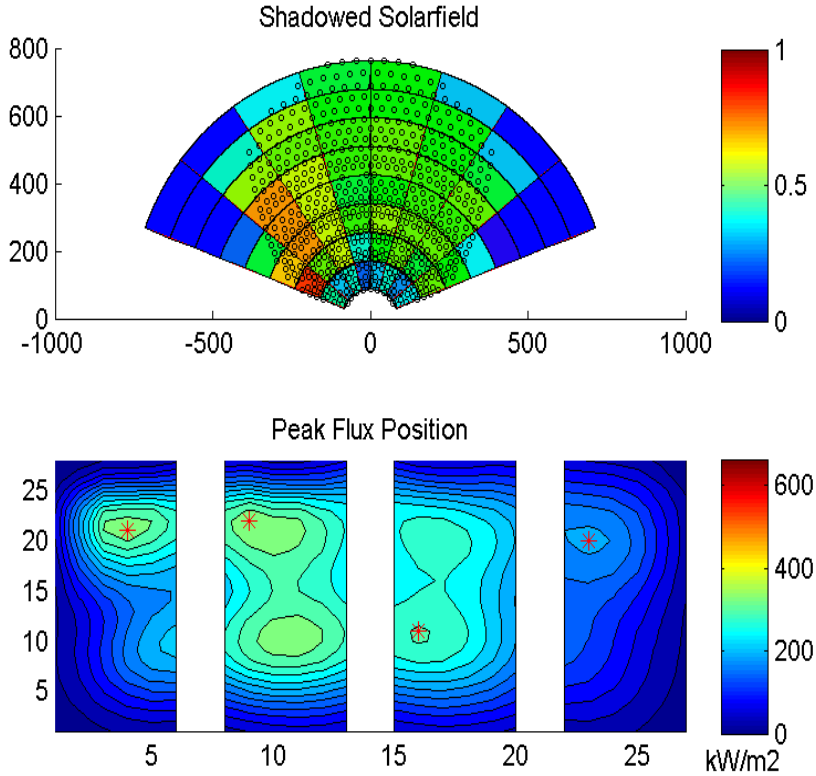


Figure 4. 11. Mixed plot graph for the input path June 9h using aiming strategy 6 in on-design conditions.

Chapter 5

Thermal model

In this chapter the heat fluxes in the receiver of the PS10 Solar power plant are analyzed, and a simplified model of the latter is proposed. The principal aim of this modeling is to obtain a temperature map of the external surface of the receiver, using the different flux maps showed in the previous chapters. Indeed, a consistent study of the thermal stresses in the receiver would be possibly achievable.

5.1 PS10 receiver model

The solution adopted for the PS10 receiver is the most economical one thanks to the use of relatively cheap materials [37]. This is possible because it consists only in an evaporation section without the presence of economizer, super-heater or re-heater. The absence of different sections allows a simpler layout of the heat exchanger. As it is possible to see from figure 6.1, another important aspect is the high heat transfer coefficient inside the pipe, due to the presence of boiling water. In the saturated flow boiling region, it almost increases of about one order of magnitude compared with the liquid forced convection one: this fact further increases the cooling effect of the water. In the model, the fluid enters in the receiver as saturated water and exits with a steam quality x_s of about 0.2 (mean value at the inlet of the steam drum); considering each pipe, typical range of x_s goes from 0.04, for the less irradiated pipes, to 0.3, for the central ones (figure 5.8). According to these values of the steam quality, forced convection flow boiling correlations are used to calculate the thermal map, in particular the boiling dominant ones (see 5.2.2, formula (15)).

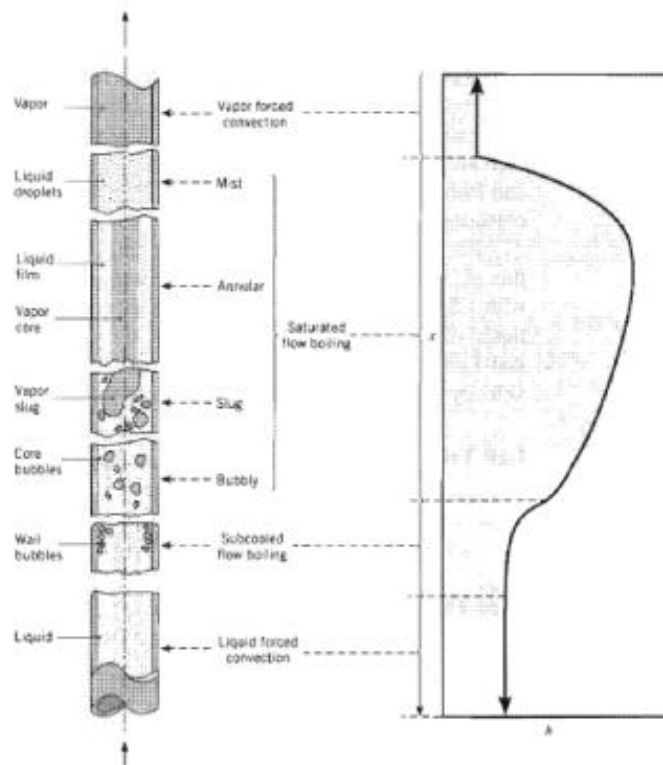


Figure 5. 1. Flow regime and heat exchange coefficient for a forced convection boiling flow in a pipe.

The model used to describe the heat exchange process that leads to the creation of thermal maps is inspired by the work previously done by [38]. In both the models a simple pipe's layout has been chosen: straight vertical pipes without bending. Moreover the mass flow is supposed to be the same for each pipe.

Firstly, a standard type of pipe is chosen [39] and the model is created, with a given flux map on the receiver. Afterwards, the mass flow rate for each pipe is adjusted in order to obtain the desired value of the steam quality at the inlet of the steam drum. As after-specified in chapter 5.2, the modeled receiver consists of 336 pipes.

Mass flow per pipe [kg/s]	Total mass flow [kg/s]	ISO-Diameter	Schedule 80 (thickness)[in]	Steam Quality
0.35	117.6	DN 2''	0.218	0.2334
0.38	127.68	DN 2''	0.218	0.2150
0.4	134.4	DN 2''	0.218	0.2042
0.42	141.12	DN 2''	0.218	0.1945

Table 5. 1. Values of the steam quality for different mass flows, using a standard size of pipe. Input used: June 12 a.m., aiming strategy 6.

A mass flow per pipe of 0.4 kg/s has been chosen as the default-value for further calculations, although it can be easily changed by the user.

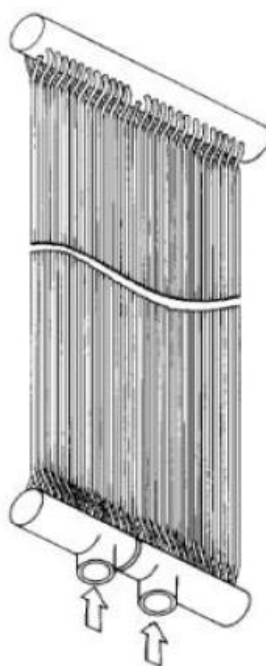


Figure 5. 2. Vertical pipes layout used in the thermal model.

5.2 Thermal model

The model takes as input the heat flux map found with the Matlab model described in chapter 4. It is so possible to simulate the quasi-static transient behavior of the solar power plant and to understand the most critical situations when a cloud is passing over the field. The discretization of the thermal map is due to the discretization of the heat flux map: each panel, a rectangle of 12 m x 5.4 m, is composed by 168 flux units, 28 in the height and 6 in the width. Therefore, each flux unit is a rectangle of 0.9 m of width 0.42857 m of height (area A_{ij} , see table 5.3): considering pipes with external diameter of 2.375 in (table 5.1), 14 pipes are attributable to a single flux unit, so 84 for each panel and 336 pipes for the entire receiver.

A thermal balance is established for each flux unit, in order to achieve the complete thermal map. Moreover, the model allows to calculate several parameters of interest, such as steam quality, external surface temperature of the receiver, the efficiency of the heat exchange process and the steam mass flow.

5.2.1 Thermal losses

Before facing the details of the iterative process used in the model, it is necessary to explain in detail all the assumptions and considerations taken into account to design the thermal model of the receiver. As already said, PS10 has a cavity receiver and this has many consequences on both the mirrors focusing process and the heat exchange. The radiation coming from the sun withstand several optical losses, as explained in chapter 1.5, and only a little part of it reaches the receiver. Moreover, the radiation that is effectively absorbed by the fluid inside the pipes is subjected to further thermal losses, showed in figure 5.3.

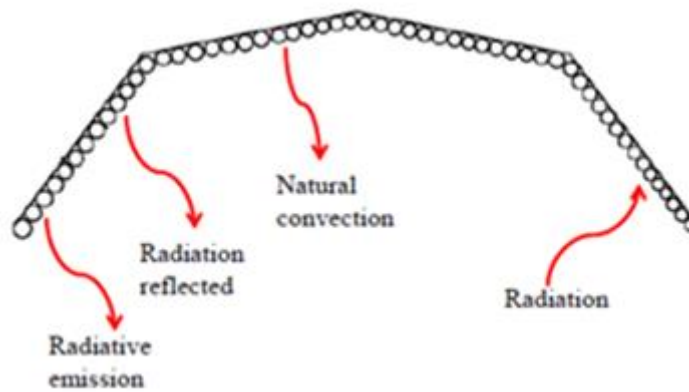


Figure 5. 3. External thermal losses for the PS10 cavity receiver.

These losses can be divided in two main groups: losses towards the ambient and losses through the interior of the tower.

Losses towards the ambient:

- *Reflection losses:* a part of the radiation is not absorbed even if the pipes' surfaces are coated with a high absorptivity paint that minimizes this loss. This phenomenon happens because part of the light coming from the heliostats is reflected by the receiver surface, and may increase throughout the lifespan of the latter, due to the degradation of the coating itself.
- *Radiative losses:* Stefan-Boltzmann equation says that each body at a temperature greater than 0 K emits energy in the form of electromagnetic radiation. The receiver is subjected to high temperature due to the strong energy incoming from the field and thus loses energy emitting radiations in the infrared and visible light. Cavity receivers present less radiative losses in respect to the external one because they have a smaller view factor.
- *Convection losses:* some of the energy is lost because the air close to the receiver surface is heated and natural circulation phenomena occur. Depending on the geometry of the receiver and its orientation, the contribution of the wind may be also taken into account, in a form of a forced convection increasing the dissipations. In the PS10 case, the receiver aperture is on the north side of the tower and the average wind direction is south-west, so the action of the wind can be neglected.

Losses through the interior of the tower:

- *Conduction losses:* even if the entire structural part and the back surface of the receiver are well insulated, a small amount of energy is lost due to conduction phenomena.
- *Radiation losses:* in order to reduce these losses, a sheet of insulating material coated with a very high reflectivity metal sheet covers the part of the pipe not

subjected to the solar irradiation. This obviously reduces the thermal losses and increases the efficiency of the heat exchange.

The amount of the losses through the interior in a concrete tower is very low compared to the external ones; therefore, for sake of simplicity they are not taken into account in the studied model.

5.2.2 Energy Balance in a flux unit

The thermal model is implemented in Matlab and computes the energy flux entering in the pipes and the relative losses for each single flux unit. An iterative process it has been set up in order to find the external temperature of the receiver.

The amount of energy that the working fluid receives is described by the following energy balance and moreover it is shown in figure 5.4

$$q_{trans} = q_{field} - q_{loss_{rad}} - q_{loss_{conv}} - q_{loss_{refl}} \quad (1)$$

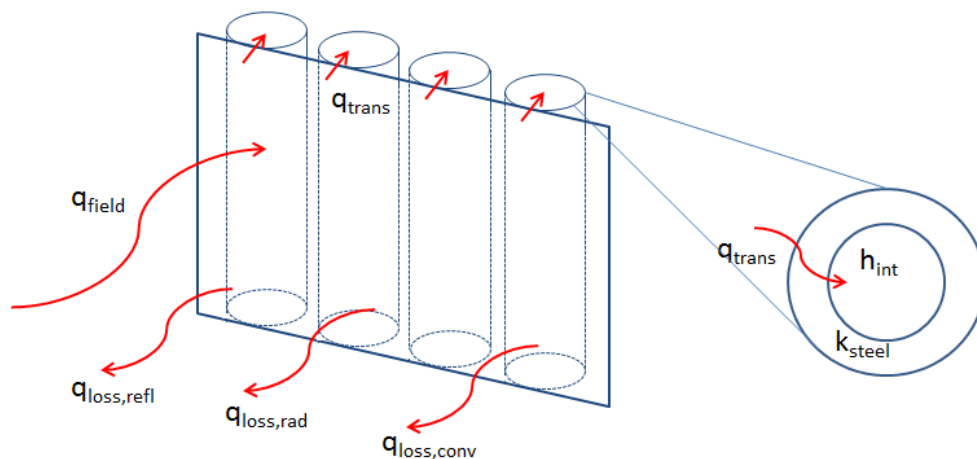


Figure 5. 4. Thermal balance in a single flux unit. In the representation only 4 of the 14 pipes are represented, in order not to overload the figure.

“ q_{field} ” is the heat flux reaching the external surface of the receiver. It is the amount of solar energy that the field actually reflects towards the solar receiver, considering the losses described in chapter 1.5.

“ q_{trans} ” is the amount of energy transferred to the fluid. Obviously it directly depends on the solar radiation and from the losses that the receiver experiences. The q_{trans} of each flux unit is transferred to a group of 14 pipes, so in order to know the amount of energy that reaches a single pipe it is necessary to divide q_{trans} by 14.

“ $q_{loss_{rad}}$ ” is the amount of energy lost by radiation towards the ambient and it is described by formula (2)

$$q_{loss_{rad}} = A \sigma \varepsilon (T_{wallExt}^4 - T_{sky-ground}^4) F \quad (2)$$

As Stefan-Boltzmann law says, the emittance of a body is proportional to the 4th power of the temperature of the body itself. “ σ ” is the Stefan-Boltzmann constant; “ $T_{wallExt}$ ” is the external surface temperature of the receiver that has to be computed, while “ $T_{sky-ground}$ ” is a mean between the temperature of the sky and the temperature of the ground. This is because the receiver cavity does not face only the sky. “ A ” is the area of the flux unit taken into account for the calculation. Due to the fact that the studied element is not behaving like a black body, also a value of emittance “ ε ” different from 1 has to be evaluated. The latter is found in literature [40] and it is the value that a selective surface of a solar receiver typically has. “ F ” is the view factor: it is a geometrical parameter that explains the reciprocal orientation of the receiver surface in respect to the cavity. Typical designs have an aperture area of about one-third to one-half of the internal absorbing surface area [41], therefore typical values of the view factor go from 0.3 to 0.5. The central panels (1e, 1w) have obviously higher view factors than the lateral ones (2e, 2w). This can be explained by looking at the different angles of the panels respect to the normal cavity’s aperture plan. The smaller this angle is, the less will be the view factor. In table 5.3 it is possible to see the different values considered.

“ $q_{loss_{conv}}$ ” is the amount of energy dissipated to the ambient due to the motion of air. The driving force of this movement is the difference in density of the air due to the different temperature.

$$q_{loss_{conv}} = A h_{conv} (T_{wallExt} - T_{amb}) \quad (3)$$

Only natural convection is taken into account because cavity receivers are thought to reduce the effects of forced convection. Moreover, in the case study, the wind is coming from south west, while the aperture faces north. This further reduces its effects.

In order to compute the heat transfer coefficient for the natural convection it has been chosen to use Churchill & Chu correlation [42].

$$Nu_L = 0,68 + \left(\frac{0,67 Ra^{0,25}}{\left(1 + \left(\frac{0,492}{Pr}\right)^{\frac{9}{16}}\right)^{\frac{4}{9}}} \right) \quad (4)$$

$$h_{conv} = \left(\frac{Nu_L k_{air}}{L} \right) \quad (5)$$

“ L ” is the characteristic length of the pipe (the height of the flux unit) and “ k_{air} ” is the thermal conductivity of air. “ Ra ” is the Raleigh number and is defined as

$$Ra = GrPr \quad (6)$$

$$Gr = \frac{g L^3 \beta (\overline{T_f} - T_{\infty})}{\nu_{air}^2} \quad (7)$$

$$Pr = \frac{\mu c_p}{k} \quad (8)$$

“ Gr ”, the Grashof number, describes the ratio between floating forces and viscous friction forces in a fluid; it characterizes the heat transmission for natural convection. Meanwhile, “ Pr ”, the Prandtl number, identifies the rate between cinematic and thermal diffusivity. “ g ” is the gravitational acceleration at ground level (9.81 m/s^2). All the thermo-physical properties are calculated at a mean film temperature \bar{T}_f of the entire receiver, result of an arithmetic mean of all the T_f of each flux unit. This approximation is done for sake of simplicity, due to the fact that the difference between the T_f is quite small and the properties do not change significantly. At $\bar{T}_f = 440.17 \text{ K}$, these properties are:

ρ_{air} [Kg/m ³]	μ_{air} [Pa*s]	ν_{air} [m ² /s]	$c_{p,air}$ [J/KgK]	k_{air} [W/mK]	$\beta = 1/\bar{T}_f$ [1/K]
0.8071	0.0000246	0.00003068	1020	0.03592	0.0023

Table 5. 2. Thermo-physical properties of air at $\bar{T}_f=440.17 \text{ K}$.

Reflection losses are described by formula (9): they depends on the reflectivity of the receiver “ ρ ” found in literature [38].

$$q_{loss_{refl}} = q_{field} \rho F \quad (9)$$

In order to find the external surface temperature of the receiver closing the iterative process, the Newton formula (10) is used: it says that the amount of heat exchanged between two bodies is proportional to the temperature difference.

$$T_{wallExt} = T_{sat} + \left(\frac{q_{trans}}{A U} \right) \quad (10)$$

“ U ” is the overall heat transfer coefficient and it is defined as

$$U = \left(\frac{1}{R_{tot}} \right) \quad (11)$$

$$R_{tot} = R_{cond} + R_{conv} \quad (12)$$

R_{tot} is the sum of the thermal resistances both due to conduction and to convection of the studied process. It can be explained by looking at figure 5.5 in which it is possible to see the electrical analogy of the heat transfer process. The Newton formula (10) describes the heat flow between the external wall surface and the internal boiling fluid. In fact it appears “ $T_{wallExt}$ ” and “ T_{sat} ”. The latter is the saturation temperature of the fluid that is constant due to the occurring phase change.

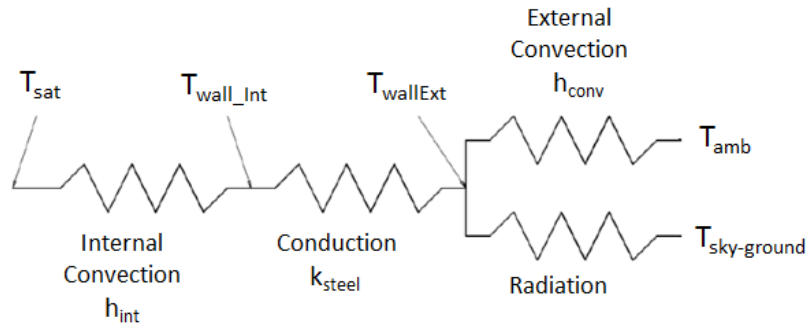


Figure 5. 5. Electric analogy of the heat transfer process.

“ R_{cond} ” calculation is shown in formula (13) and it describes the behavior of a cylindrical wall with an internal radius “ r_{int} ” and an external one “ r_{ext} ”.

“ k_{steel} ” is the thermal conductivity of the material of the pipes.

$$R_{cond} = \left(\frac{r_{int}}{k_{steel} \ln\left(\frac{r_{ext}}{r_{int}}\right)} \right) \quad (13)$$

On the other hand, the computation of “ R_{conv} ” is more complicated because it has to be taken into account an empirical correlation that describes the behavior of the forced flow boiling conditions in pipes.

$$R_{conv} = \left(\frac{1}{h_{int}} \right) \quad (14)$$

“ h_{int} ” is the heat transfer coefficient of water inside the pipes and it is defined by Kandlikar correlation [43], for a Nucleate Boiling Region:

$$h_{int} = h_l (C_1 Co^{C_2} + C_3 Bo^{C_4}) \quad (15)$$

“ C_1 ”, “ C_2 ”, “ C_3 ” and “ C_4 ” are constants which values are shown in table 5.3, while “ h_l ” is the convective coefficient of the fluid in liquid phase and it is explained by the following formulas (properties calculated at T_{sat}):

$$h_l = \left(\frac{Nu_l K_l}{D_{int}} \right) \quad (16)$$

$$Nu_l = 0.023 Re_l^{0,8} Pr_l^{0,4} \quad (17)$$

$$Pr_l = \frac{\mu_l C_{p_l}}{k_l} \quad (18)$$

$$Re_l = \frac{m_l * D_{int}}{A_{pipe} \mu_l} \quad (19)$$

“ Nu ” is the Nusselt number and it describes the ratio between the heat exchanged by convection and the one by conduction. The adopted correlation, developed by *Dittus-Boelter*, is largely used in literature [42]. The condition described by the latter is fully developed turbulent flow and heating process of the internal fluid. “ Re_l ” and “ Pr_l ” describe respectively the state of motion of the fluid and the ratio between cinematic and

thermal diffusivity. “ μ_l ”, “ Cp_l ” and “ k_l ” are the viscosity, the heat capacity and the thermal conductivity of the water in liquid state while “ D_{int} ” and “ A_{pipe} ” are the internal diameter and the cross sectional area of the pipe.

$$Bo = \left(\frac{q_{trans}}{m_{in} \Delta h_{lv}} \right) \quad (20)$$

Correlation (20) is called *boiling number* and at the numerator it is possible to see the heat transferred to the fluid “ q_{trans} ” and at the denominator there are the mass flow rate in each pipe “ m_{in} ” and the enthalpy of evaporation of the water “ Δh_{lv} ”

$$Co = \left(\frac{1-x}{x} \right)^{0,8} \left(\frac{\rho_s}{\rho_l} \right)^{0,5} \quad (21)$$

Formula (21) is the *convection number* correlation and it relates the density of the steam “ ρ_s ” and the one of the water “ ρ_l ”. Moreover, it appears also the steam quality “ x_s ”. In this way, it is possible to take into account the amount of convection due to the mixed flow condition.

To define all the properties of the water in the pipes it has been used *XSteam*, a function of Matlab.

Further constants used in the model are shown in the following table:

A_{ij}	[m ²]	0.3857	r_{int}	[m]	0.0246
σ	[W/m ² K ⁴]	5.6704e-08	$T_{sky-ground}$	[K]	300
ε		0.4	T_{amb}	[K]	298.15
ρ		0.02	T_{sat}	[K]	523.51
$F_{2e,2w}$		0.3	Δh_{lv}	[W/K]	1.7135e+06
$F_{1e,1w}$		0.45	C_1		0.6683
k_{steel}	[W/mK]	16	C_2		-0.2
A_{pipe}	[m ²]	0.0019	C_3		1058
r_{ext}	[m]	0.0302	C_4		0.7

Table 5. 3. Some constants taken into account in the thermal model.

5.2.3 Mathematical Iterative Process

As already explained in the previous paragraph, the thermal model is implemented in Matlab and follows a standard guideline of an iterative process.

The entire receiver is divided in 672 flux units (168 for each panel), organized in 24 columns (6 for each panel) of 28 elements. The Matlab code calculates the $T_{wallExt}$ of each flux unit separately by two nested “*for*” loops: the first loop is for the 24 columns, the second one is for the 28 rows of each column. Each column presents 28 flux units; as a consequence, 29 knots have to be considered in order to univocally define each unit. In each knot, thermo-physical properties of the working fluid are calculated using the Matlab function *XSteam*; whereas in each flux unit the model obtains the non-dimensional numbers, the velocity of the fluid and $T_{wallExt}$. Moreover, a third nested “*for*” loop is

included, in order to make possible the determination of the temperature map of the receiver for each time-step.

Once defined the energy balance in each flux unit (see 5.2.2) the T_{wallExt} is initialized at the value of the T_{sat} for the entire receiver and all the properties of the saturated water at the inlet are calculated; after that, the iterative process begins. Firstly, the incident thermal power coming from the field is taken from the heat flux map defined in chapter 4 (q_{field}) and also the thermal losses $q_{\text{loss,rad}}$, $q_{\text{loss,conv}}$ and $q_{\text{loss,refl}}$, respectively with (2), (3) and (9). Then, the thermal power that reaches the working fluid, q_{trans} , is obtained with (1). Afterwards, thermo-physical properties and non-dimensional numbers are calculated, and T_{wallExt} is obtained with (10), once determinate the overall heat transfer coefficient inside the pipe (formulas from (11) to (21)). At the end, the new T_{wallExt} is compared with the old one: if the percentage error is lower than the pre-defined one (10^{-3}), the T_{wallExt} for the considered flux unit is finally obtained.

Once the model has calculated the value of the T_{wallExt} for all the flux units, the temperature map for the entire receiver is achieved for each time step, and further studies are therefore attainable.

5.3 Graphical Results

The thermal model provides a series of graphs, which simplify the comprehension of the thermal behavior of the PS10 receiver, and the correspondent numerical results, by which is possible to achieve conclusions about the thermal stresses affecting the receiver itself.

The most important graphical results are:

- *External wall temperature* graph: a first graph plotted by the model is the *surf* map of the T_{wallExt} for the entire receiver. A strong similarity with the surf map of the heat flux can be observed.

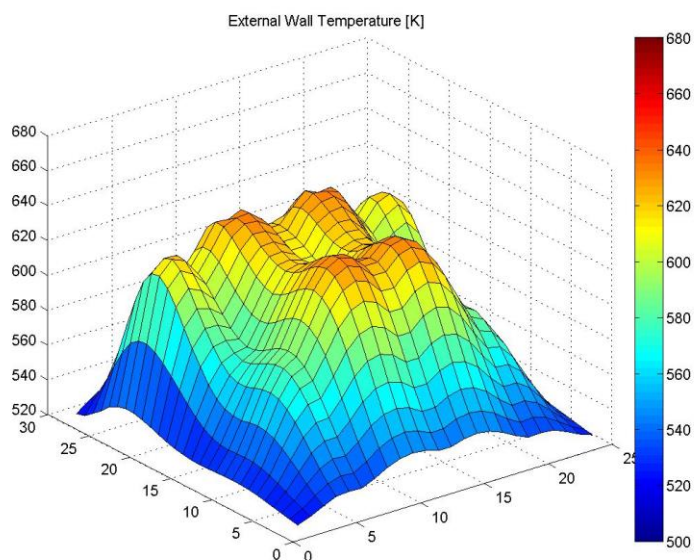


Figure 5. 6. External wall temperature surf map (21th June, 12 a.m., aiming strategy 6).

- *Thermal mixed plot* graph: in order to allow a simultaneous evaluation of the temperature distribution and the temperature gradient on the receiver, a *thermal mixed plot* is produced. This graph consists of two *contour* graphs (see figure 5.7), it indicates the location of the peak temperatures and peak gradients and can be particularly useful in the understanding of some peculiarities of the thermal behavior of the receiver (see chapter 6).

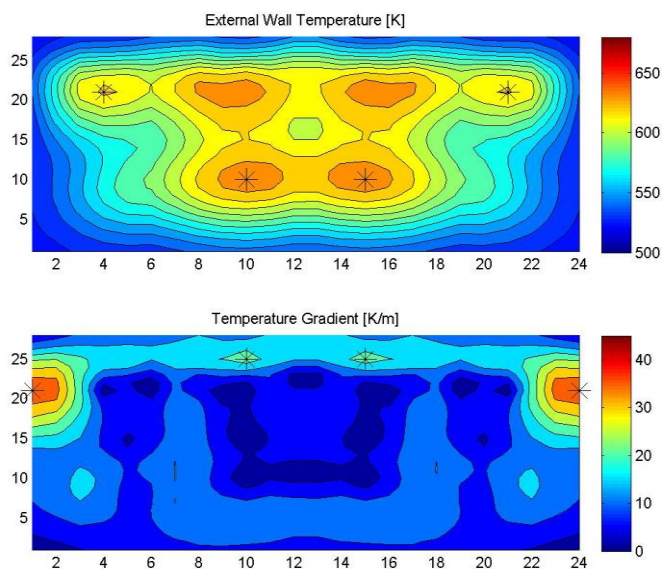


Figure 5. 7. Thermal mixed plot graph at same conditions of figure 5.6.

- *Steam quality* graph: finally, a surf map of the steam quality is produced. In this graph it can be perfectly observed the x_s distribution along each column and among the whole receiver, concurring with the explanation given in 6.1.

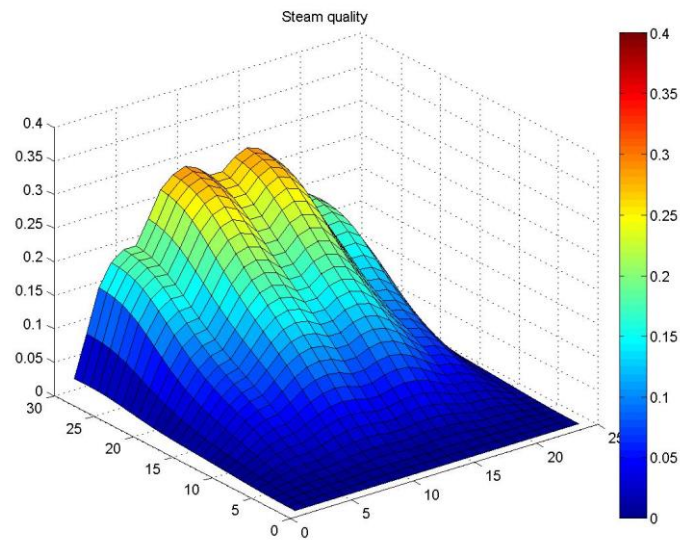


Figure 5. 8. Steam quality graph at same conditions of figure 5.6.

Moreover, the model produces a series of numerical results, discussed in chapter 6, which permit to come to conclusions about the thermal behavior of the receiver. These results are mainly the steam mass flow and quality, the receiver efficiency and some characteristics of the temperature distribution, such as the peak temperatures, the temperature gradients and the temporal variation of the peak temperature.

Chapter 6

Discussion of the results

In the present chapter the results obtained with the two codes are analyzed. Firstly, the analysis of the outcomes of the code explained in chapter 4 is performed, along with further considerations about the optical performance of the solar field; secondly, the results obtained with the thermal model are discussed, in order to confirm the conclusions previously done.

6.1 PS10

6.1.1 Heliostats efficiency and characteristics of the field

The graphical results of the program *Solar_Tool_5* are also particularly useful to understand several characteristics of the field of the PS10.

The graph *Solar field by heliostats* (figures 6.1 and 6.2) allow the user to have an idea of the global behavior of the field at different hours and days during the years, by observing the efficiency of each heliostat. As explained in the paragraph 4.2.1, this graph represents the global efficiency of the heliostats, which takes into account several factors, already explained in the chapter 1.

Firstly, it can be observed how the efficiencies change during the year, due to the cosine effect. Globally speaking, in June the efficiency is lower than in March and December, due to the fact that the sun is higher in the sky, and the heliostats must be oriented in an incommodious way to focus at the receiver (North-field). Nevertheless, the DNI in June is higher, so the difference in terms of overall power produced and peak flux in each panel is not excessively pronounced. Due to the different elevation of the sun also different shadows of the tower are produced: in December the shadow affects a significant part of the field, especially in the morning and in the afternoon, but also at noon; in March this effect is less important and it disappears completely in June.

The elevation of the sun during morning and afternoon also produces a global reduction of the efficiency of the heliostats located respectively in the east and west side of the field. In other words, the right half of the field (east) presents lower efficiencies in the morning and higher ones in the afternoon, compared with the left half (west), due to the cosine effect. This circumstance results to be stronger in March, on the other hand in June the field appears more homogeneous.

The spillage losses and the attenuation caused by atmospheric transmittances can be perfectly observed: the heliostats located in the last rows, furthest from the tower, present efficiencies considerably lower than the nearest ones. All of these features can be observed in the figures 6.1 and 6.2.

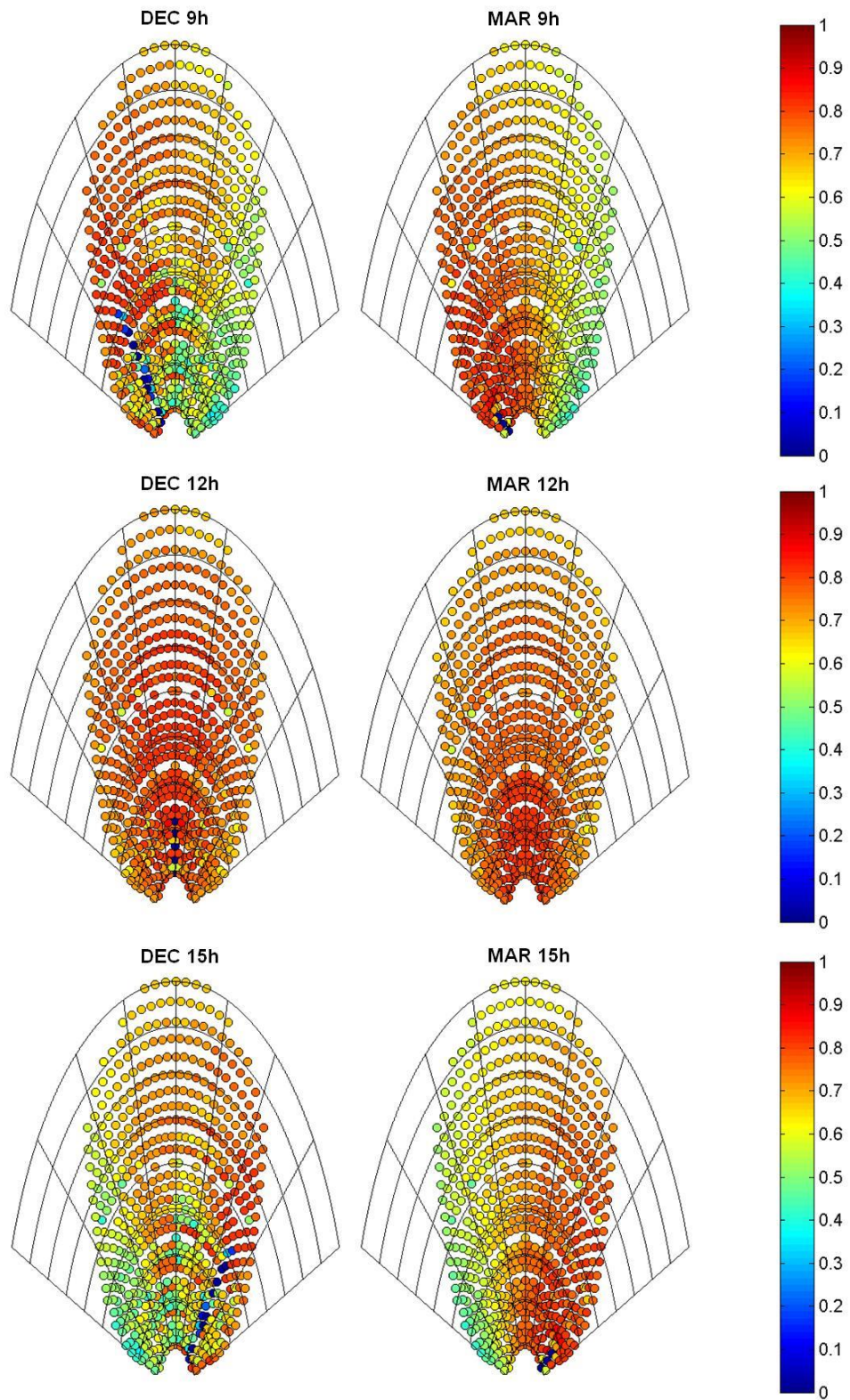


Figure 6. 1. Solar field by heliostats graph for September and March at 9h, 12h and 15h.

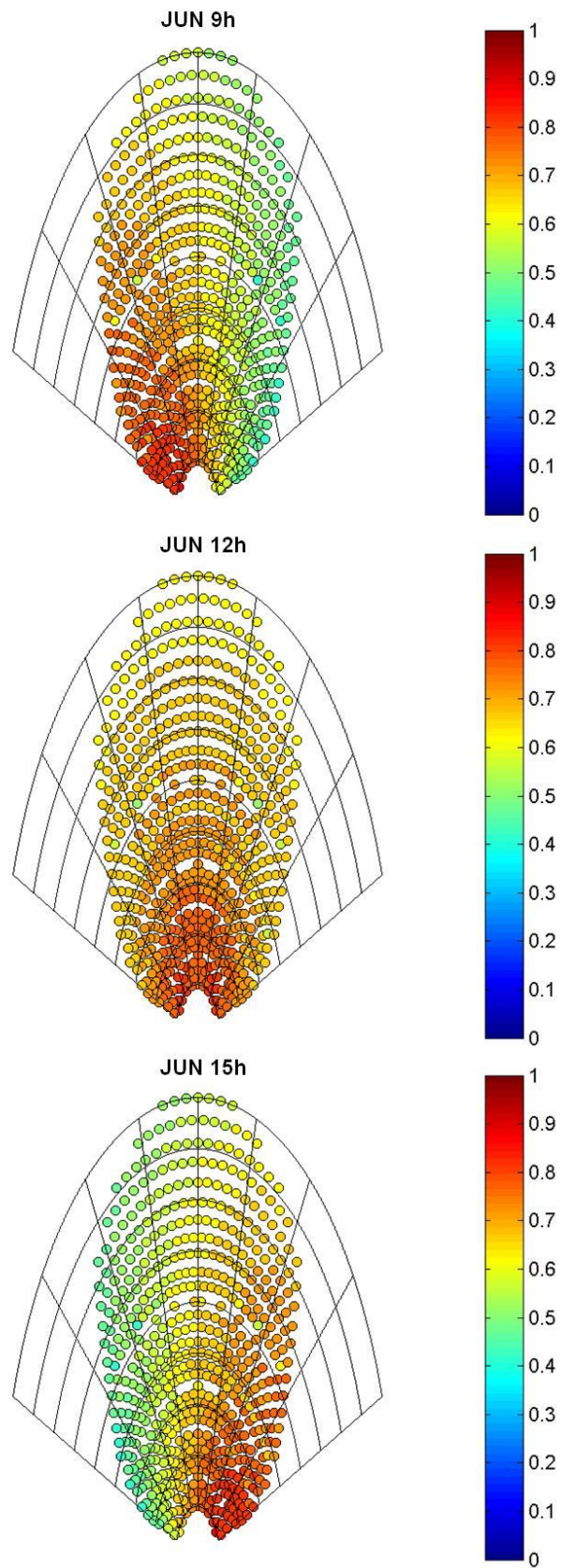


Figure 6. 2.Solar field by heliostats graph for June at 9h, 12h and 15h.

Further information can be obtained from the *Solar field by zones*, as shown in figure 6.3. At noon, the zones that contribute the most to the heat flux are the ones located in the first half of the field, in central position. The reason is not only the good efficiencies of the correspondent heliostats; also its greater “heliostats density” has to be considered. At morning and afternoon the situation is similar, with the difference that these zones are located respectively in the left part and in the right part, in an almost symmetrical way. This circumstance, observing the figure 6.3, seems to be lightly different, especially for the graph obtained at 12h. The reason of the incongruity is that the field of the PS10 is not perfectly symmetric and with the approximation made to develop the division in zones (annulus, see chapter 2) some zones could contain few more heliostats than in the reality. This fact also explains the difference between the zones located next to the center, i.e. zones 4-5, 12-13, 20-21, 28-29 and so on. Theoretically they would have to produce a very similar heat flux, but in the graph seems to be quite different: it can be explained assuming that the heliostats located exactly in the center line are assigned to the right zone by Matlab (possible improvement discussed in chapter 7).

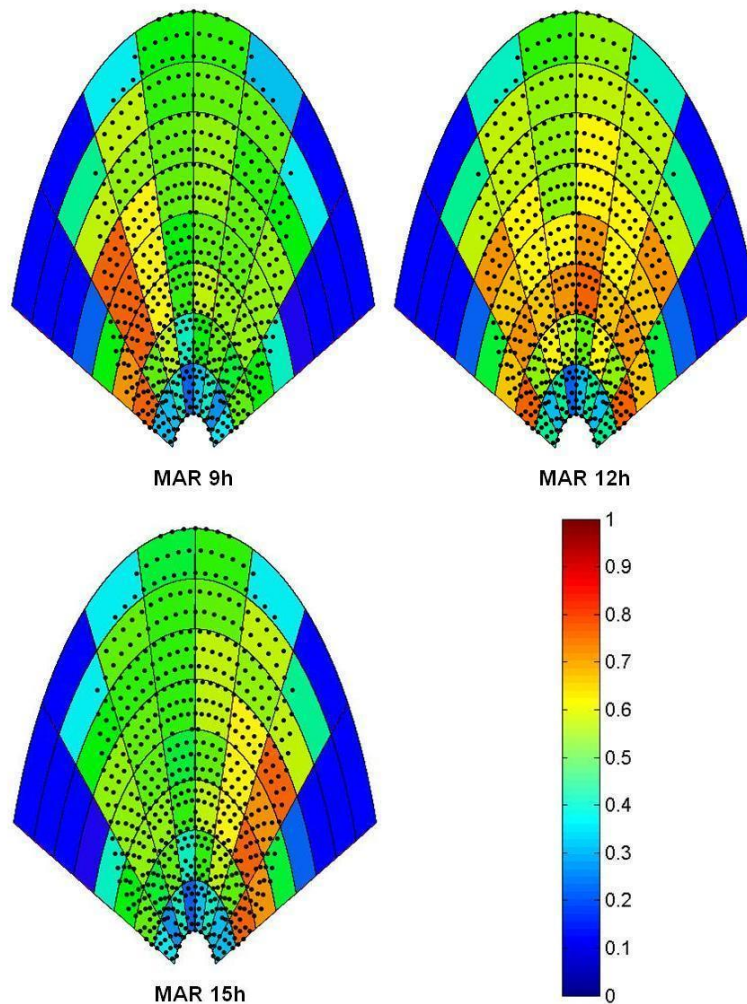


Figure 6. 3.Solar field by zones graph for March at 9h, 12h and 15h.

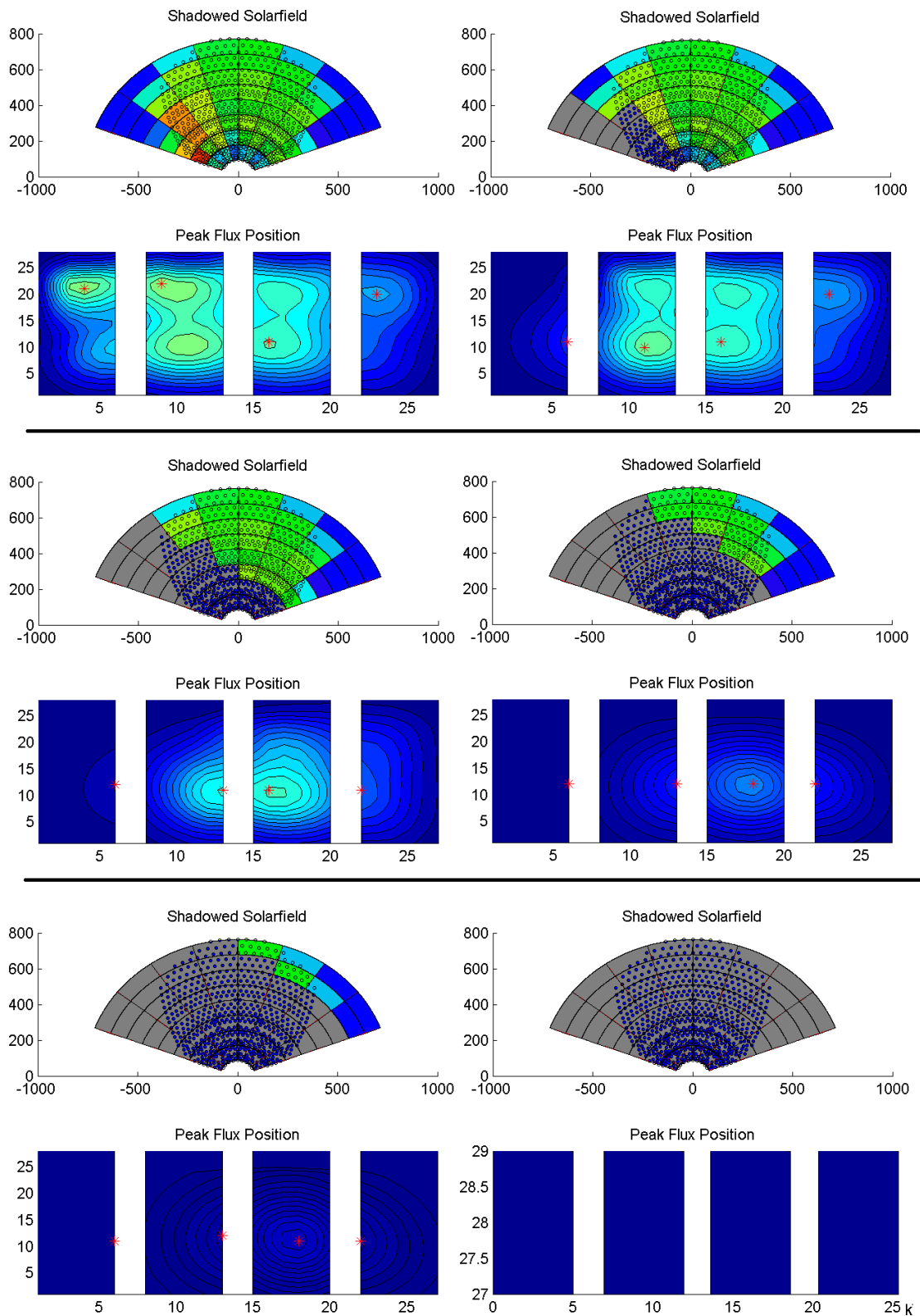


Figure 6. 4. Move of Peak Flux during the covering of the field (Jun 9 a.m., aiming strategy 6, Mixed plot graph)

In the figure 6.4 a representation of the *mixed plot* of the first 6 successive time steps is provided, with a total shadow covering the field. It can perfectly be observed the move of the peak flux in each moment, due to the change of the incoming radiation. Since the first 4 rows of the field are aiming to point 2 or 8 and the other to point 5 (aiming strategy 6), the peak flux goes down towards the middle of the panel, when the zones aiming to point 2 are being covered.

Moreover, it can be seen how the sectors of the field contributes to each panel of the receiver in a really intuitive way (figures 6.4 and 2.9).

6.1.2 Numerical results

The variables taken into account in the study of the numerical results are:

- *Peak flux*: it is the maximum value of the heat flux on the receiver, evaluated separately for each panel. Indeed, tracking a profile of this variable for the whole receiver would be useless in transient condition, due to the fact that the peak flux repeatedly changes its location from one panel to another: the study of the possible thermal stresses would lose importance, physically speaking. Therefore, the value of the peak flux and its position are calculated for each panel. An explicatory example is shown in the figure 6.5, and a representation of the change of the flux map during the passage of a big cloud covering the entire solar field is provided in 6.6.

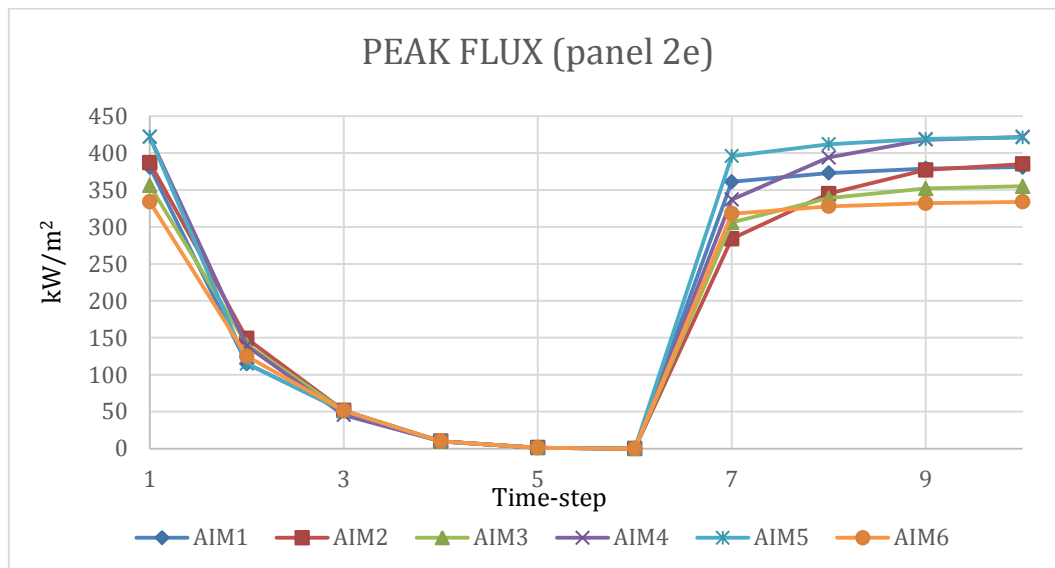


Figure 6. 5. Trend of the peak flux for the panel 2e during the passage of a big cloud covering the entire the solar field (March 12h).

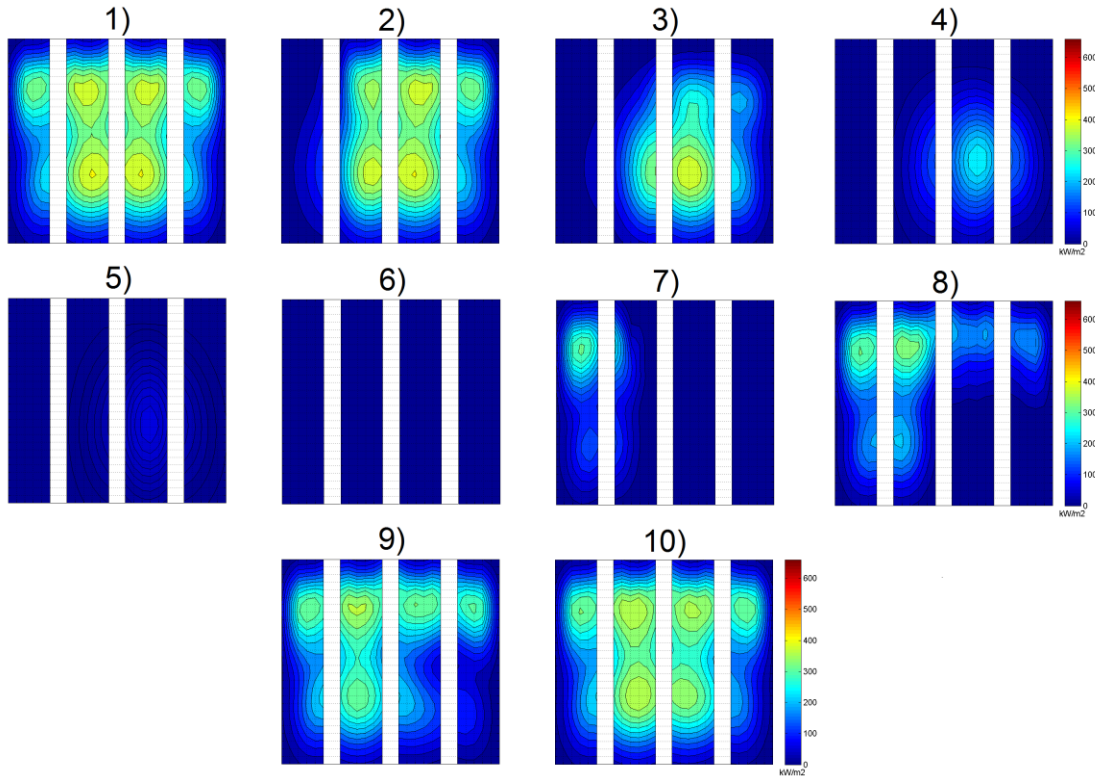


Figure 6.6. Representation of the change of the flux map during the passage of a big cloud covering the entire solar field for the same situation described in figure 6.7, using strategy 6.

- *Punctual Variation of the heat flux*: the maximum value of the peak flux, despite its importance, is not enough to consider in a proper way the possible thermal stresses suffered by the receiver. Another important aspect to take into account is the temporal variation of the heat flux during the process of covering/uncovering of the solar field, later simply called “delta peak flux”. A great variation of the latter could possibly be more dangerous for the coating material of the receiver than a high value of the peak flux [44].

For each time step, the difference between the value of the heat flux and its value in the previous step is calculated, for each point of the receiver. The maximum value is therefore charted, as it can be observed in the next figure. One thing is to be noticed: as this variable consists in a difference between two consequent time steps, in this diagram only nine points are evaluated. In the point 1 the difference between the second and the first time step is represented, and so on.

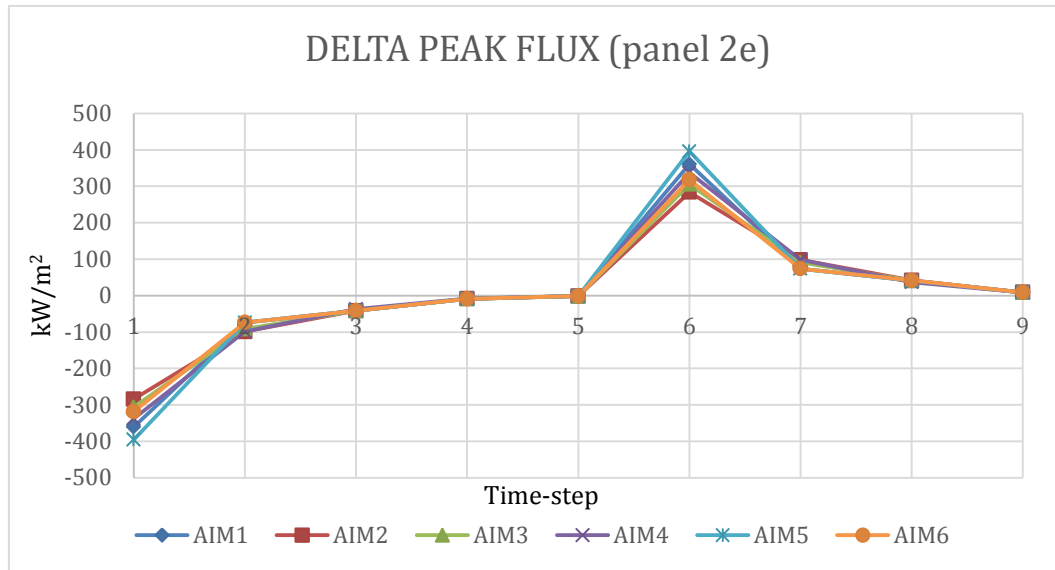


Figure 6. 7. Trend of the Punctual variation of the heat flux for the same situation described in figure 6.5.

- *Maximum gradient (in units $(kW/m^2)/m$):* This variable has been taken into account in order to consider another aspect of this study. A great value of the spatial gradient of the heat flux could possibly indicate an area of the receiver affected by thermal stresses, so a zone to be taken into account to avoid premature failure of the component. The spatial gradient of the heat flux is calculated for each point (see *Gradient Map*, in the previous paragraph) and its maximum value is charted for each time step (an example in figure 6.8).

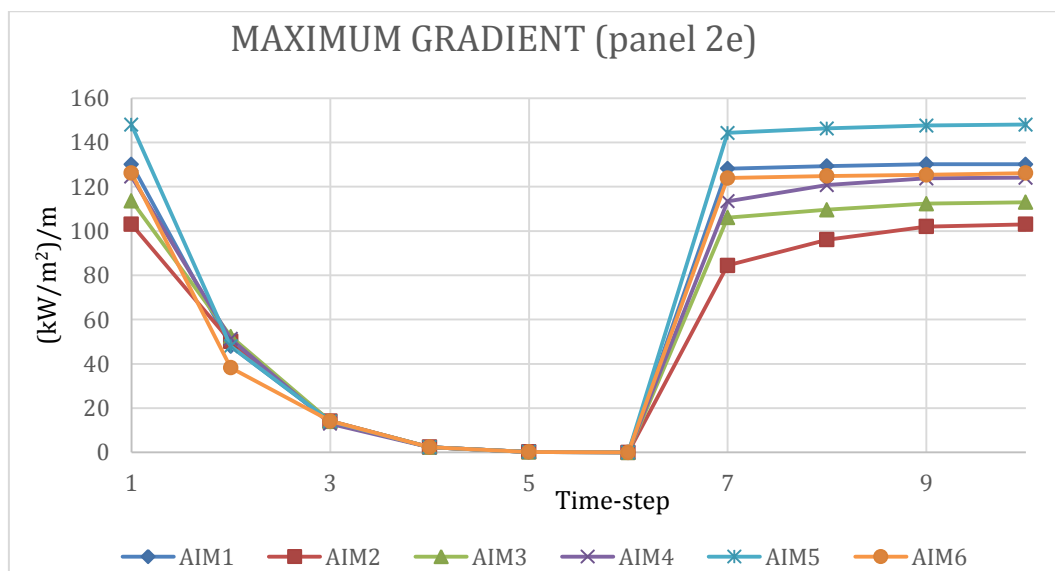


Figure 6. 8. Trend of the Maximum Gradient for the same situation described in figure 6.5.

- *Overall power*: it is the gross power onto the whole receiver, and its value is obtained directly from the output of Delsol, in MWth. This variable is not strictly connected with the possible thermal stresses of the receiver, but it has been decided to consider it in order to take into account also the production of thermal power. The idea is that the selection of the best aiming strategy in a transient condition it is not only a matter of avoiding great stresses due to quick variations of the incident heat flux (and the consequent variations of the temperature of the receiver). Due to the fact that an existing power plant is the object of this study, the real production of power is certainly a crucial factor: on equal terms regarding the further variables, the solution with the highest overall power obviously has to be chosen.

In the figure 6.9 a typical profile of the overall power for the passage of a big cloud covering the entire solar field can be seen.

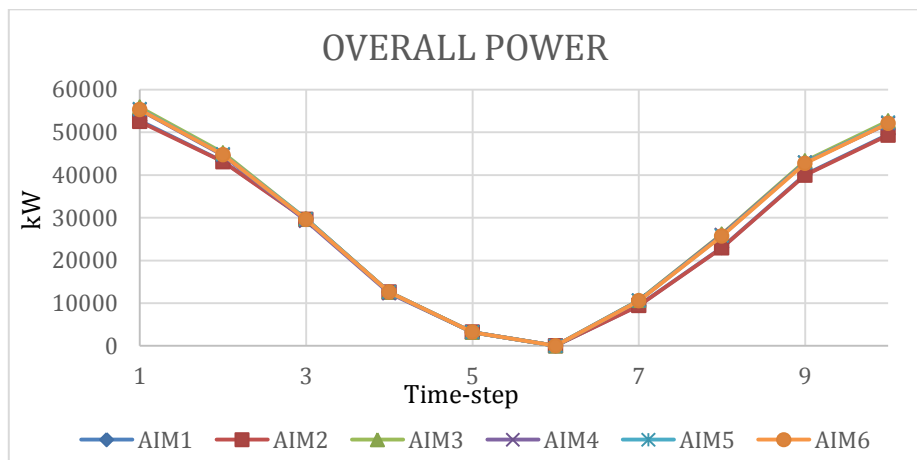


Figure 6. 9. Trend of the Overall Power during the passage of a big cloud covering the entire solar field (June 12h).

6.1.3 Worst conditions analysis

In order to identify the worst cloud, the obtained results have been synthesized with histograms and the maximum delta peak flux has been chosen as the most significant parameter. Starting from the analysis of the delta peak flux graphs (figure 6.7) for all the possible combinations of clouds/strategies, the maximum punctual variations of the peak flux, during the entire shadowing process, have been selected. In this way, the histograms are representative of the step-by-step sudden variations of the incident peak flux and they can be used to analyze the worst off-design condition.

As it is possible to see in the figures 6.10 and 6.11, the maximum delta peak flux varies a lot with different type of clouds and for different inputs. Comparing the graphs, it is possible to notice that the ratio between the maximum delta peak flux values, for two selected clouds, is almost the same for different days at the same hour. For this reason the graphs of March are not reported here. The histograms regarding the aiming strategy 6 are representative of the other ones, which show similar trends with different magnitudes.

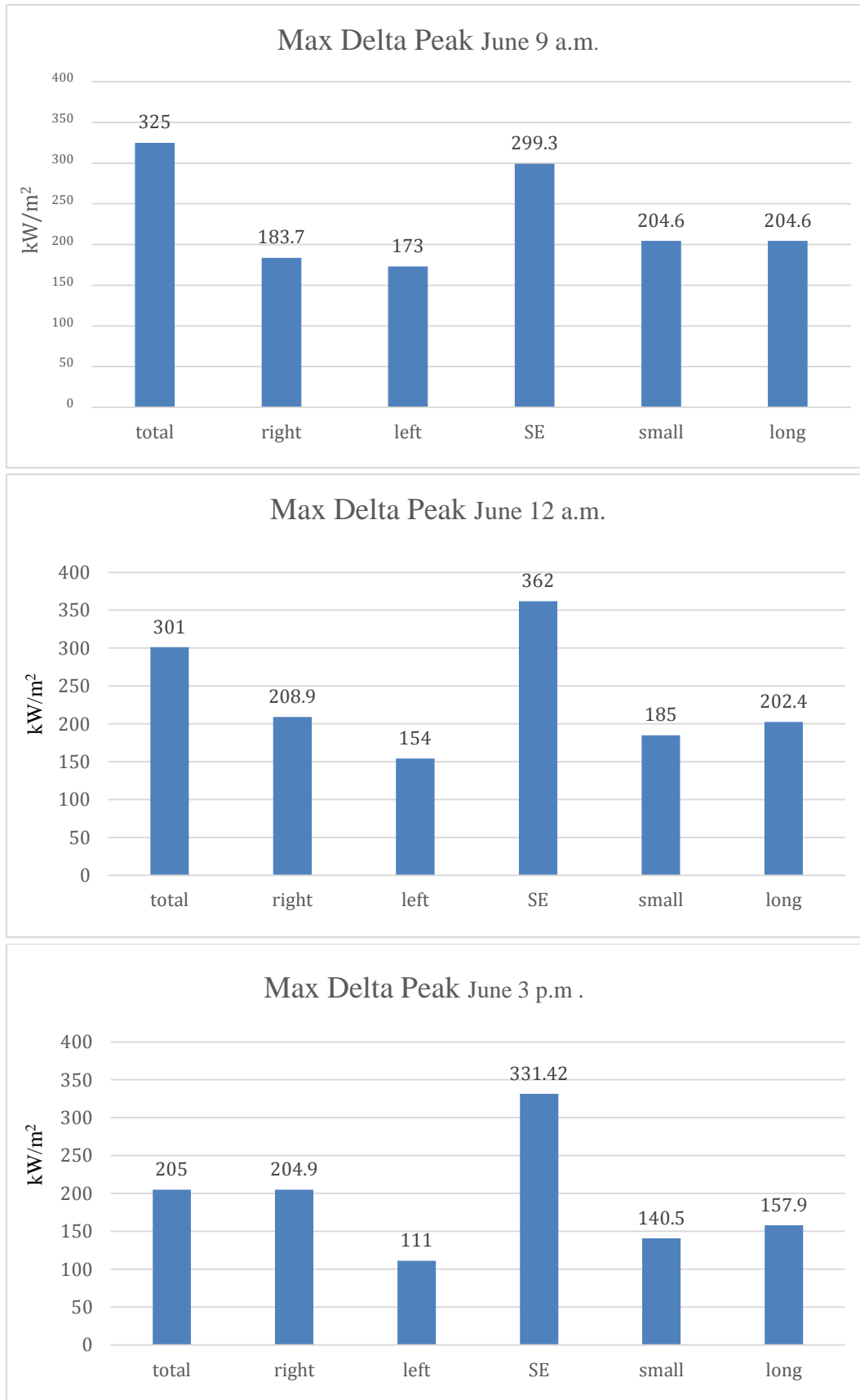


Figure 6. 10. Maximum delta peak flux value on 21th June, at 9 a.m., 12 a.m. and 3 p.m., using aiming strategy 6.

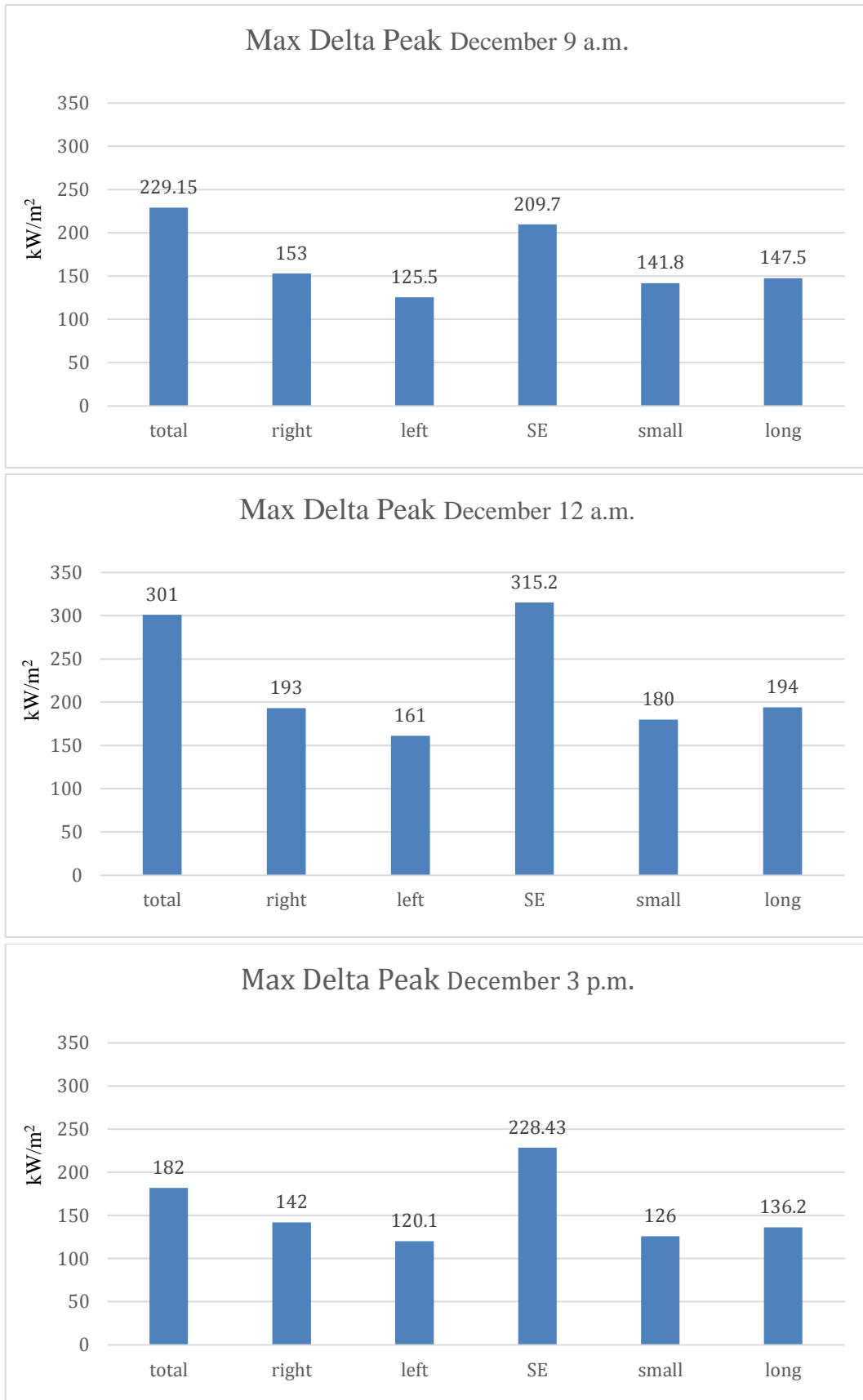


Figure 6. 11. Maximum delta peak flux value on 21th December, at 9 a.m., 12 a.m. and 3 p.m., using aiming strategy 6.

The largest delta peak flux values are found, obviously, for the clouds in which the entire solar field is shadowed. However, it is possible to notice that small and long cloud cases are worse than left cloud, even if the latter cover a bigger part of the field.

Delta peak fluxes for right cloud are very similar to the long cloud ones. This is a clear confirmation that the amount of shadowed heliostats is not the only relevant parameter for this kind of analysis. This is due to the initial characterization of the clouds (chapter 2): long cloud shadows the central part of the field, whereas the right one shadows half of it. In the first case a smaller amount of heliostats is shadowed, but they are the most efficient.

Another outcome is the difference between the two total shadows: at 12 a.m. and 3 p.m. the cloud coming from S-E presents greater values of delta peak flux, meanwhile the S-W cloud shows greater value in the morning. The difference is due to the location of the highest efficiency heliostats during the day. However, it would be expected an identical behavior at mid-day: this discrepancy is due to the not symmetrical choice of the wind direction in respect to the North-South direction.

In conclusion, the worst cloudy day conditions are not always the ones with big clouds. The way in which a cloud crosses the field is a crucial factor: a small cloud passing in the middle could be worse than a big one covering half of the field.

6.1.4 Selection of the best aiming

Subsequently to the interpretation of the clouds behavior, a deep study has been done on the best aiming strategy option. In order to select it, three different criterions have been evaluated: maximum peak flux value, maximum delta peak flux value and maximum gradient value. Moreover, also the total gross power has been taken into account. These three parameters have been already explained in 6.1.2, and the related excel graph are showed below:

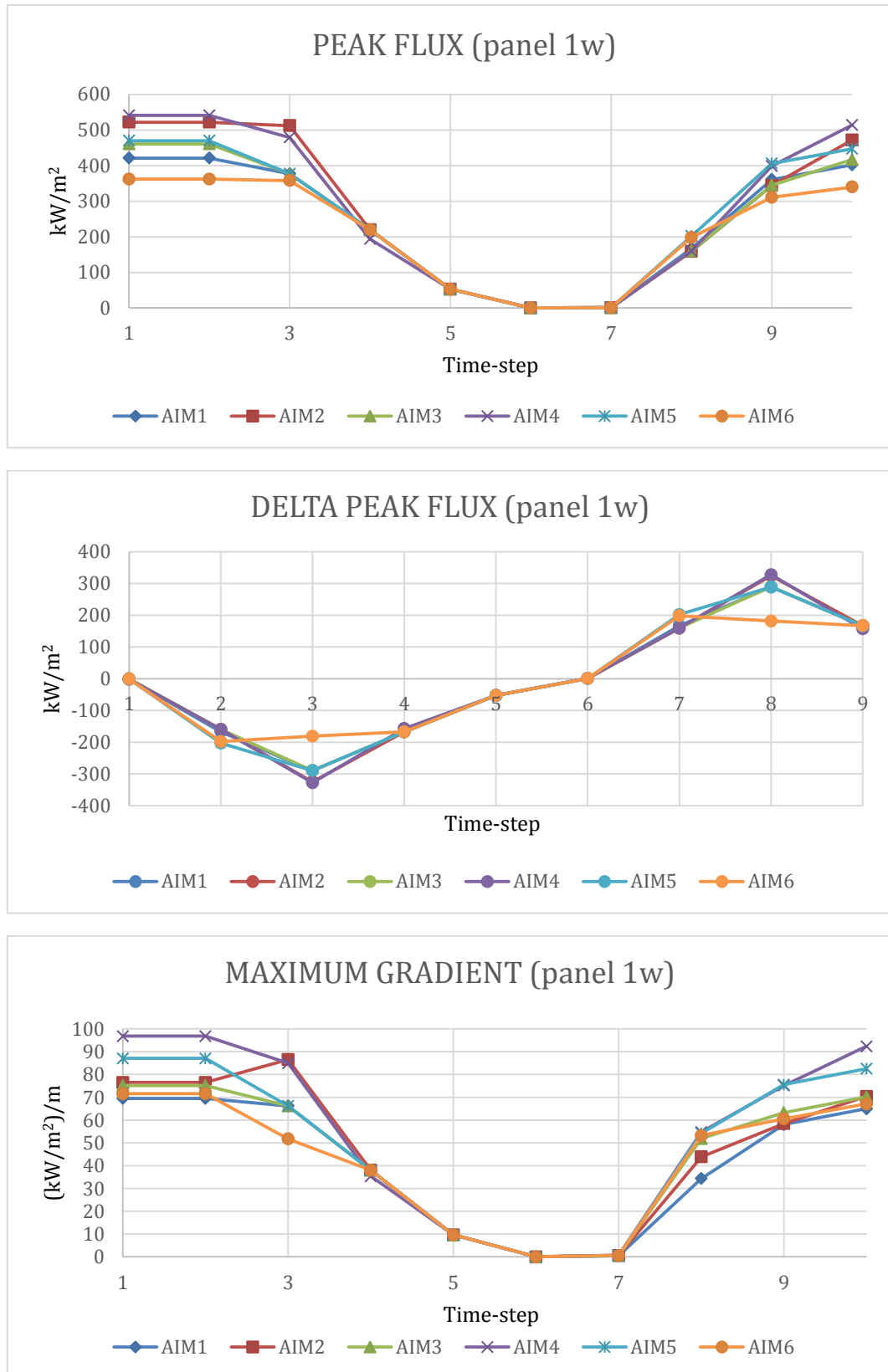


Figure 6. 12. Peak Flux, Delta Peak Flux and Maximum Gradient values of panel 1w on 21th June, at noon, in case of total shadow.

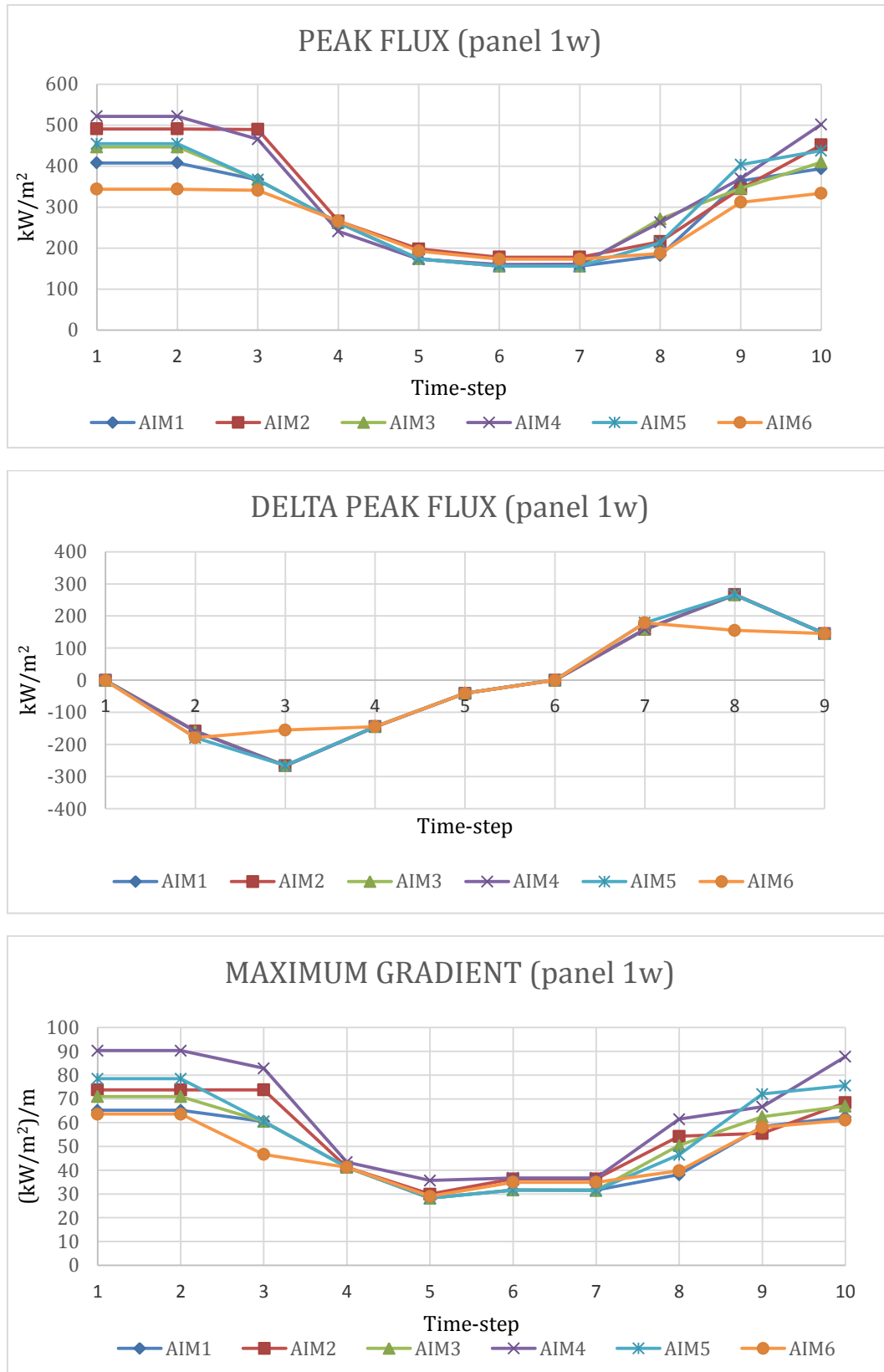


Figure 6. 13. Peak Flux, Delta Peak Flux and Maximum Gradient values of panel 1w on 21th June, at 3 p.m., in case of a big cloud covering only the right half of the field.

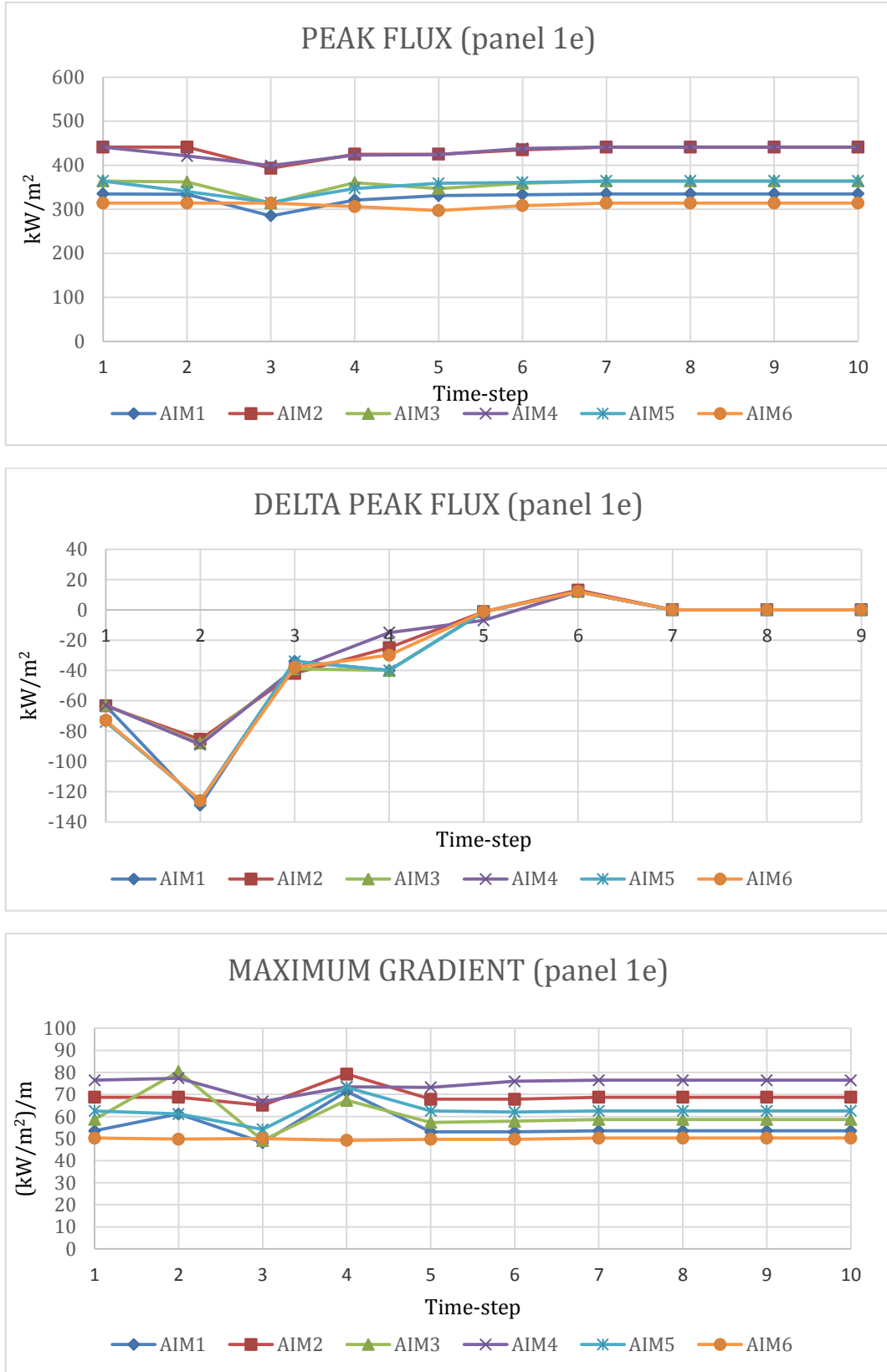


Figure 6. 14. Peak Flux, Delta Peak Flux and Maximum Gradient values of panel 1e on 21th December, at 3 p.m., in case of small cloud.

It have been selected the most representative graphs; these show the clear success of aiming strategy 6. In all the aspects studied, it has shown a better behavior and also the power reduction is not significant respect to the results achieved (see chapter 2).

Only in the case of small cloud, the strategy 4 showed a lesser value of delta peak flux due to aiming strategy itself, which focuses 4 rows (3, 4, 5 and 6) on the point 2. But, due to the fact that the gross power output is smaller than aiming 6 and the max peak flux value is grater, it is definitively possible to say that the best aiming strategy is the number 6.

This is a very important achievement because it shows that the best aiming strategy found by De Giorgi for the on-design conditions it is also the best for a transient working operation.

6.2 Gemasolar

6.2.1 Heliostats efficiency and characteristics of the field

The efficiency of Gemasolar solar field for the three days considered in the present work is showed in figure 6.15. Comparing figure 6.15 (Gemasolar) and figure 6.1 (PS10), it can be noticed that surrounding field shows the best efficiency (e.g. average efficiency) in June, while north field during the solstice of winter. These contrasting results can be explained considering the contribution of the cosine effect. The two plants are located in the same region, so the latitude does not change and thus does not affect. Observing only the north part of the surrounding field (figure 6.15) it is possible to see that its highest efficiency occurs on 21th December, but the situation changes when the whole field is considered. The reason is due to the more unfavorable position of the mirror respect to the tower during winter. In June, the sun has a higher azimuth angle and this allows a better reflection of the incoming radiation by the southern heliostats. This aspect increases the average efficiency of the whole field. In table 6.1 it is possible to see a resume of the maximum and the average whole efficiency of the mirrors for the three different days taken into account.

	21 th March	21 th June	21 th December
Max Efficiency [%]	90,90	89,80	89,80
Average Efficiency [%]	62,55	64,43	56,13

Table 6. 1. Resume of the efficiencies of the field for different days, at noon.

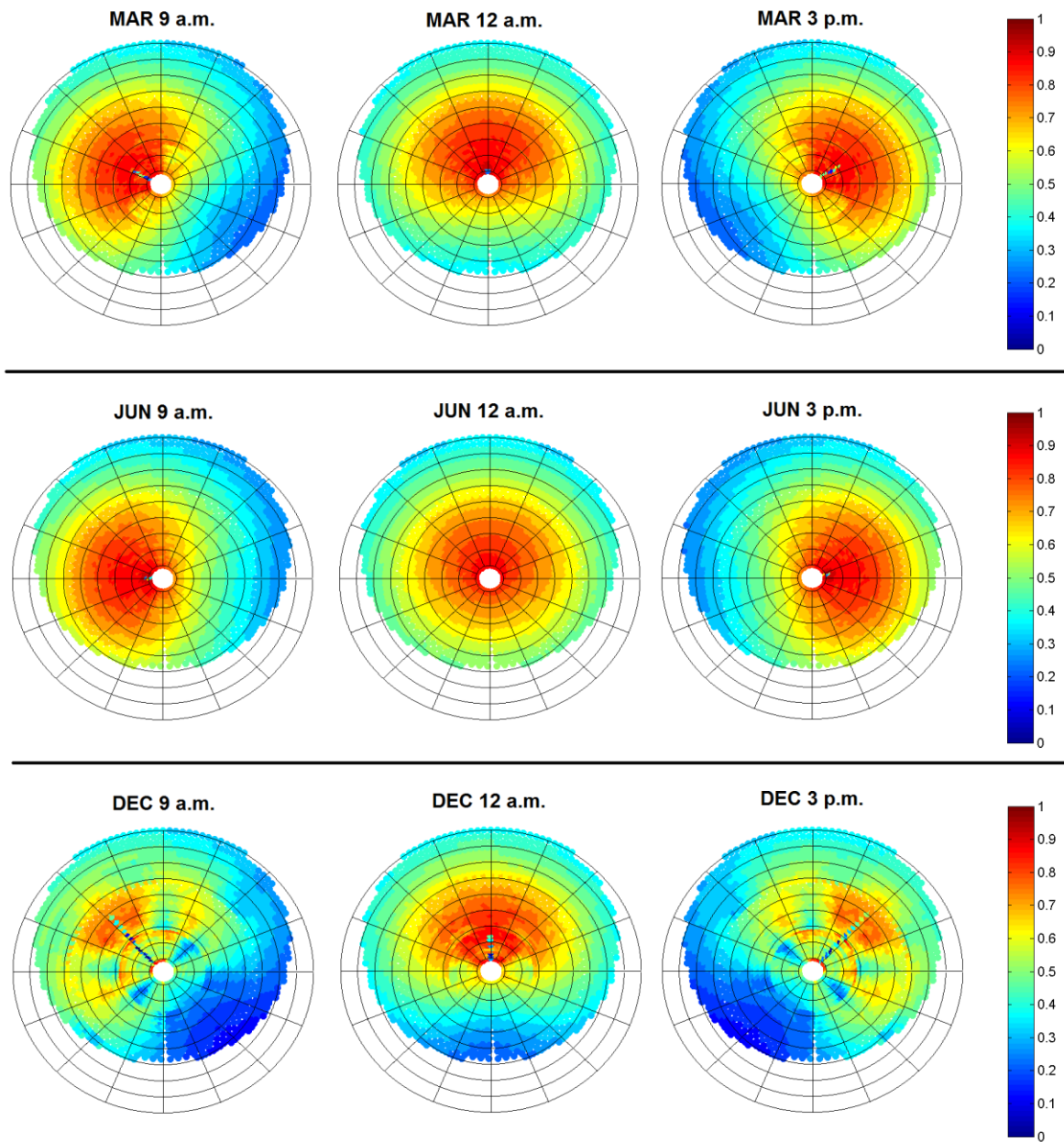


Figure 6. 15. Solar field by heliostats graph for different hours and inputs.

In order to explain the different contributes that take part to the whole efficiency value, previously explicated in chapter 1.5, the five different effects of each single loss are showed in figure 6.16. For the sake of clarity, value of 1 (red) means no losses, value of 0 (blue) means that no reflected radiation can reach the receiver. Here follows brief descriptions of each contribute:

a) *Total efficiency:*

It is the results of the sum of the other contributes and is the one represented by the *Solar field by heliostats* graph.

b) *Cosine effect:*

The pattern of this particular image is due to the fact that at 9 o'clock the sun is just raised almost in the east direction. For this reasons the lesser efficiency heliostats are the one located in the southwest positions. The cosine effect results to be one of the most important losses of the plant and it changes both during the year and during the day.

c) *Shadowing effect:*

Depending on the position of the sun can happen that some of the mirrors shadow partially other heliostats, stopping the radiation coming from the sun. As it possible to see from the image also the tower has a great shadowing effect.

d) *Atmospheric attenuation:*

This effect grows with the distance from the tower, due to the obvious fact that the greater is the latter, the greater is the amount of radiation absorbed by the atmosphere. The particular feature of this effect is that it remains the same for the whole year, at each hour.

e) *Blocking:*

It can happen, depending on the actual azimuth and elevation of the sun, that not all the radiation leaving a heliostat reaches the tower because another mirror blocks the radiation. From figure 6.16 it is possible to see that the contribution of this effect is very spread in the whole field mainly because the sun is low in the sky.

f) *Spillage:*

According to chapter 1.5, the heliostats affected the most by this effect are the furthest ones; but it is possible to notice that also the mirrors situated close to the tower in the south east position are affected by this loss. This is due to the unfavorable position of the sun in the morning for these heliostats (cosine effect). It is not possible to focus the entire image of each heliostat on the tower for a view angle issue; for this reason only a part of the radiation leaving the mirror reaches the receiver.

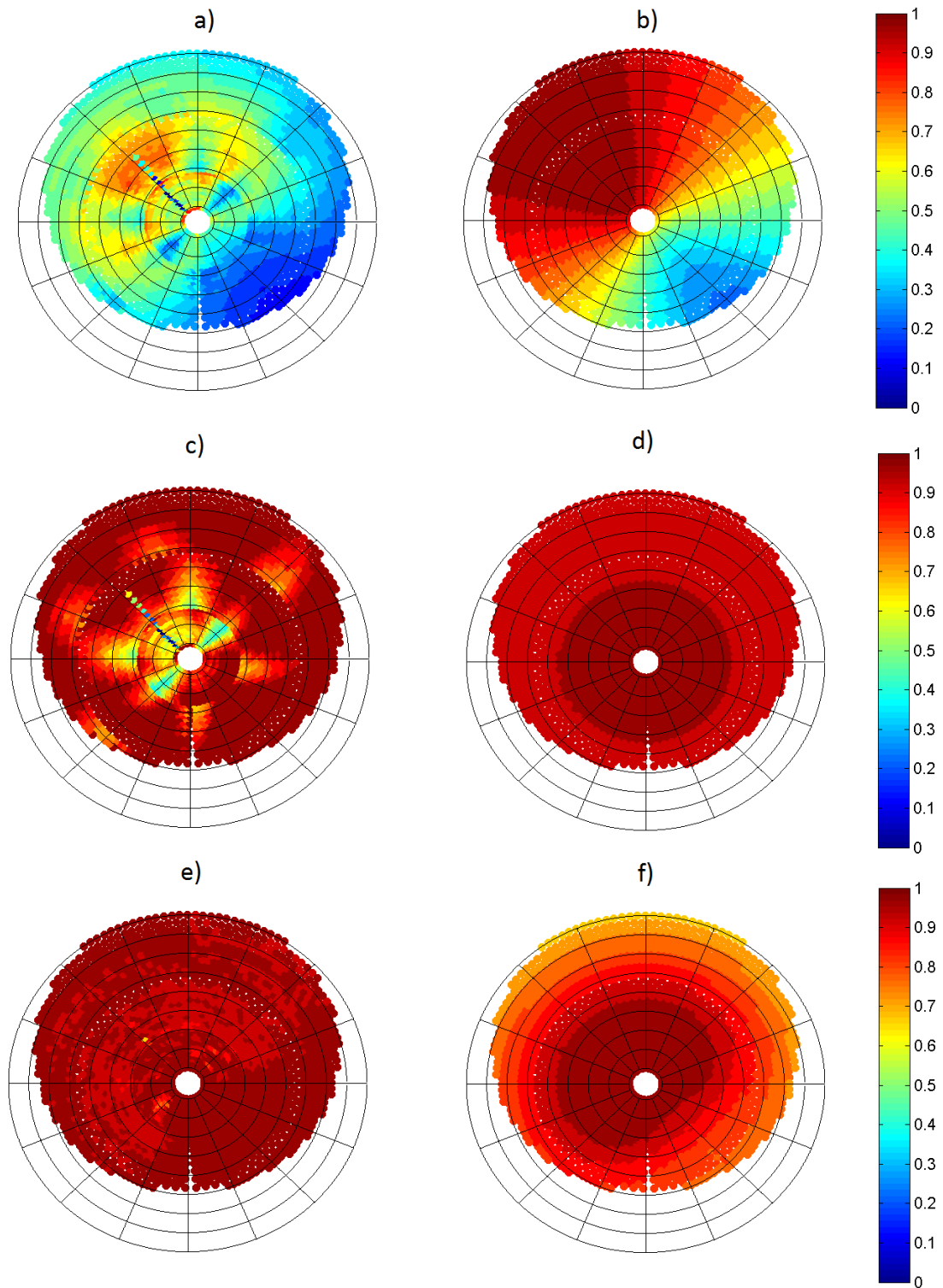


Figure 6. 16. Representation of the different contributes of the heliostats efficiency (21th December, 9 a.m.).
Letters refer to the previous page.

Further information can be obtained with *Solar field by zones* and *Mixed plot* graphs, respectively in figure 6.17 and 6.18. The achievable conclusions are similar to the ones obtained for the PS10 plant in chapter 5.1.1: the amount of energy provided by each zone depends both on the heliostats density and their efficiencies. In figure 6.17 it can be observed the presence of more incisive zones, located in the first half of the field, in central position (in the north part) at noon; considering morning and afternoon, these zones obviously change their location according to the sun's position, and they are almost symmetrical. Slight irregularities of this trend are due to Delsol and Matlab zone subdivisions criteria, as explained in chapter 6.1.1.

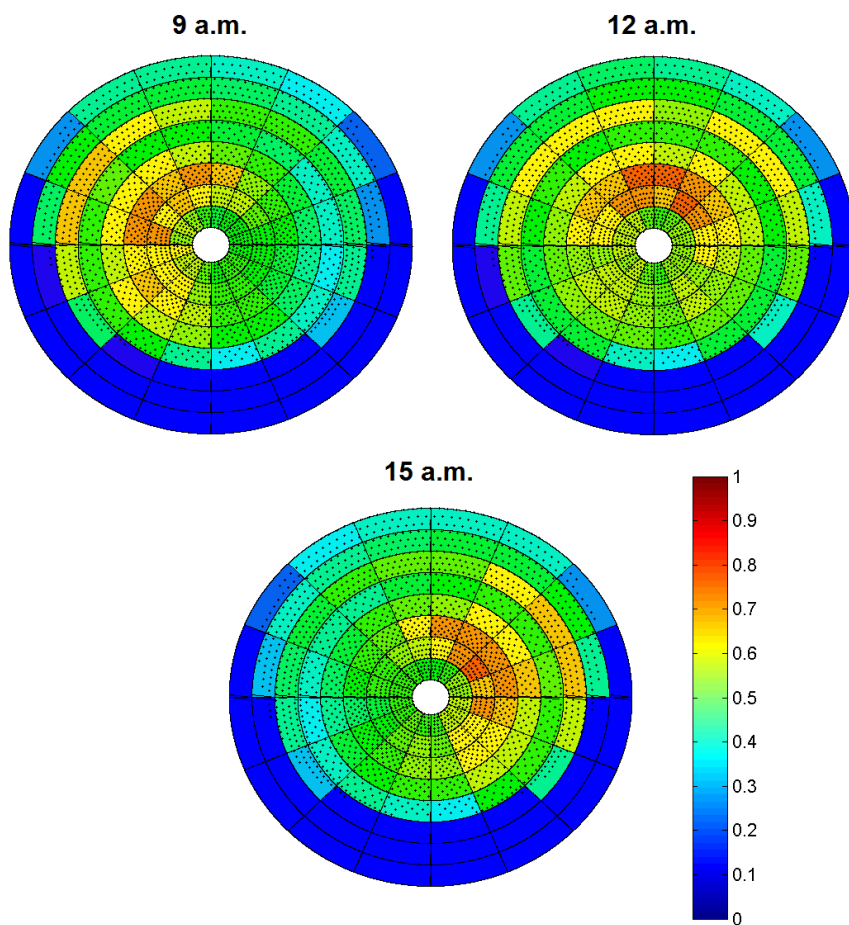


Figure 6. 17. Solar field by zones graph for 21th June, at 9 a.m., 12a.m. and 3 p.m.

In figure 6.18, in the same way as figure 6.4, the *Mixed plots* for 6 time steps are shown. Identical conclusions can be obtained, considering that this time the move of the peak flux is slightly weakened by the southern part of the surrounding field, nonexistent in the PS10, which provides an additional amount of energy.

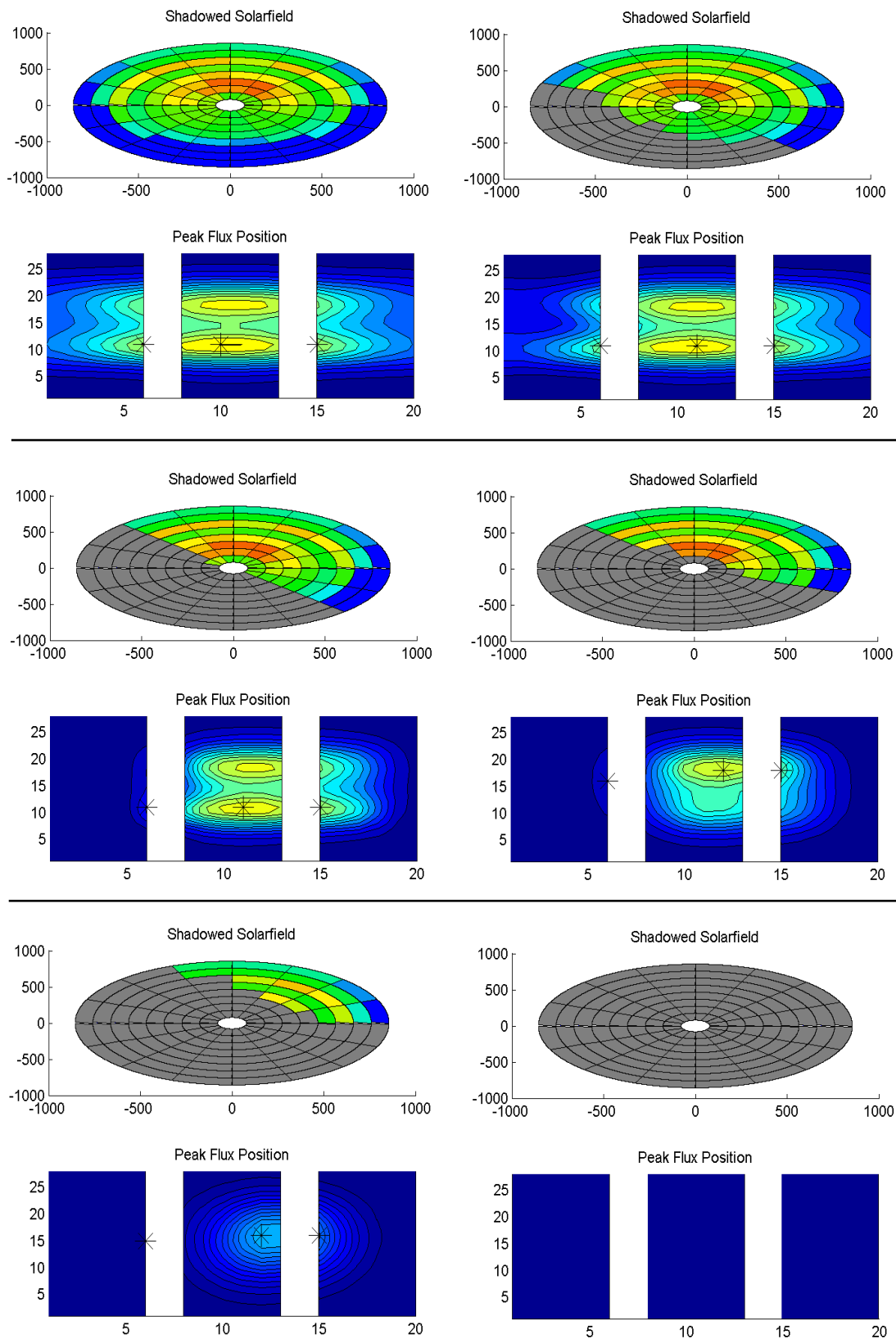


Figure 6. 18. Move of Peak Flux during the covering of the field (March 12 a.m., aiming strategy 6, Mixed plot graph)

6.2.2 Worst conditions analysis

For each input, the most significant parameters are plotted, and they are the same used to analyze the PS10 transient behavior: maximum peak flux value, maximum delta peak flux value and maximum gradient value.

In order to understand the most critical transient situations that lead to sudden changes in heat flux and thus to thermo-mechanical stresses, histograms are used to synthesize the results. The most significant ones are the delta peak flux. By looking at them, it is possible to understand how each clouds affect the solar radiation. Moreover, it is possible to understand why the plant is behaving in this way by looking at figures 6.16(a), 2.5 and 2.6. Comparing these three figures, it is possible to see which heliostats are affected by each cloud.

For example, looking at figure 6.19 it is possible to see that small cloud has a very low impact at 9 a.m., while the same cloud at 3 p.m. has much more influence. This happen because the cloud, in every simulation, pass always on the same mirrors, but those change efficiency during the day due to the above seen effect.

Another significant result is the difference between “*small cloud*” and “*two small clouds*” in December at noon (figure 6.20). It is possible to see that due to the efficiency of the heliostats and due to the path of the clouds, the first case has much more influence on the delta peak flux even if the area covered is almost an half of the case with two small clouds.

Therefore, it is possible to explain the different behaviors of the cloud by looking at the efficiencies of the shadowed heliostats. The results obtained from the study of the transient of PS10 case are confirmed: size does not always matter. In fact, the crucial factor is not only the size of cloud, but its position in the field.

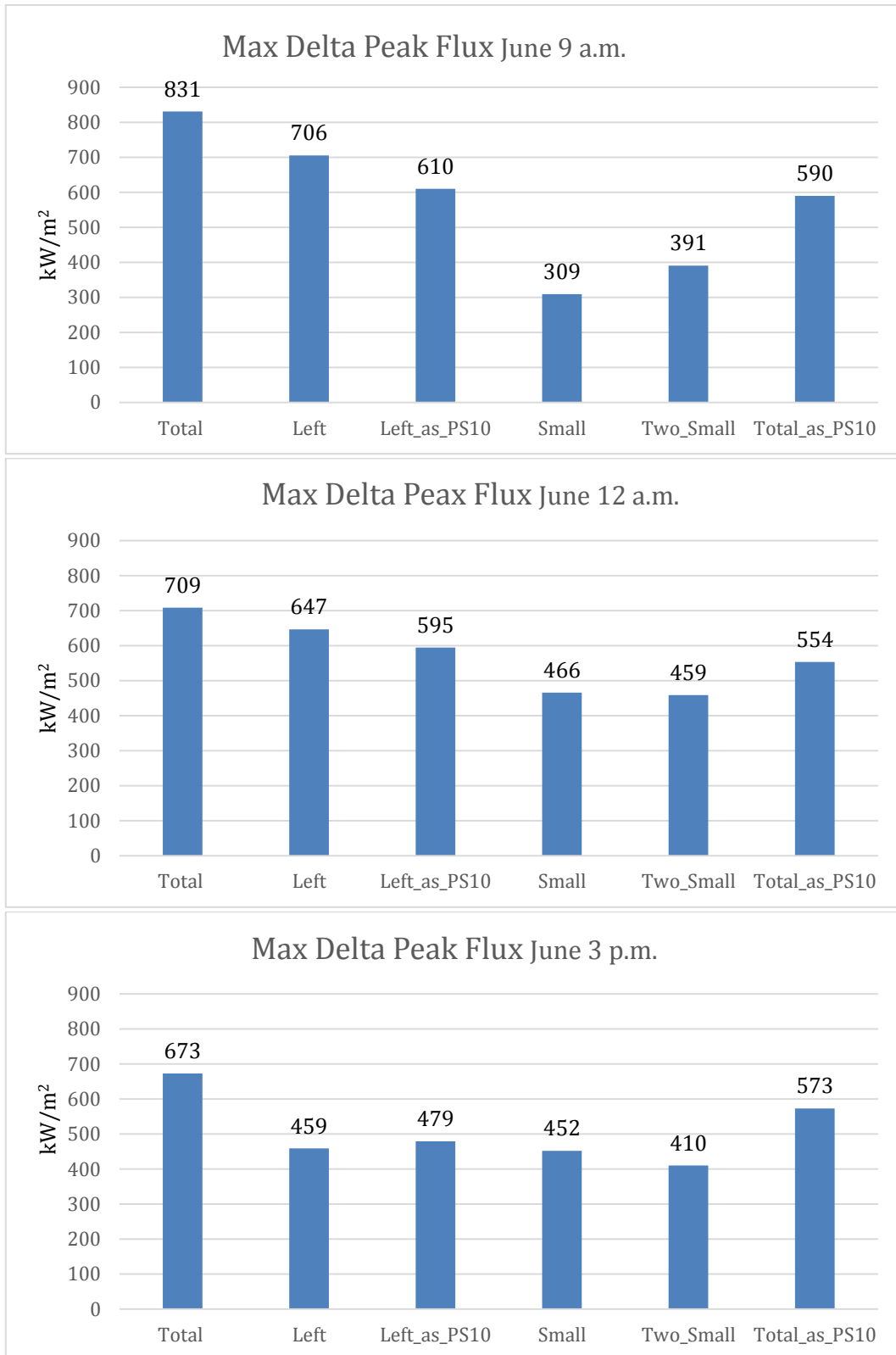


Figure 6. 19. Maximum delta peak flux value on 21th June, at 9 a.m., 12 a.m. and 3 p.m.

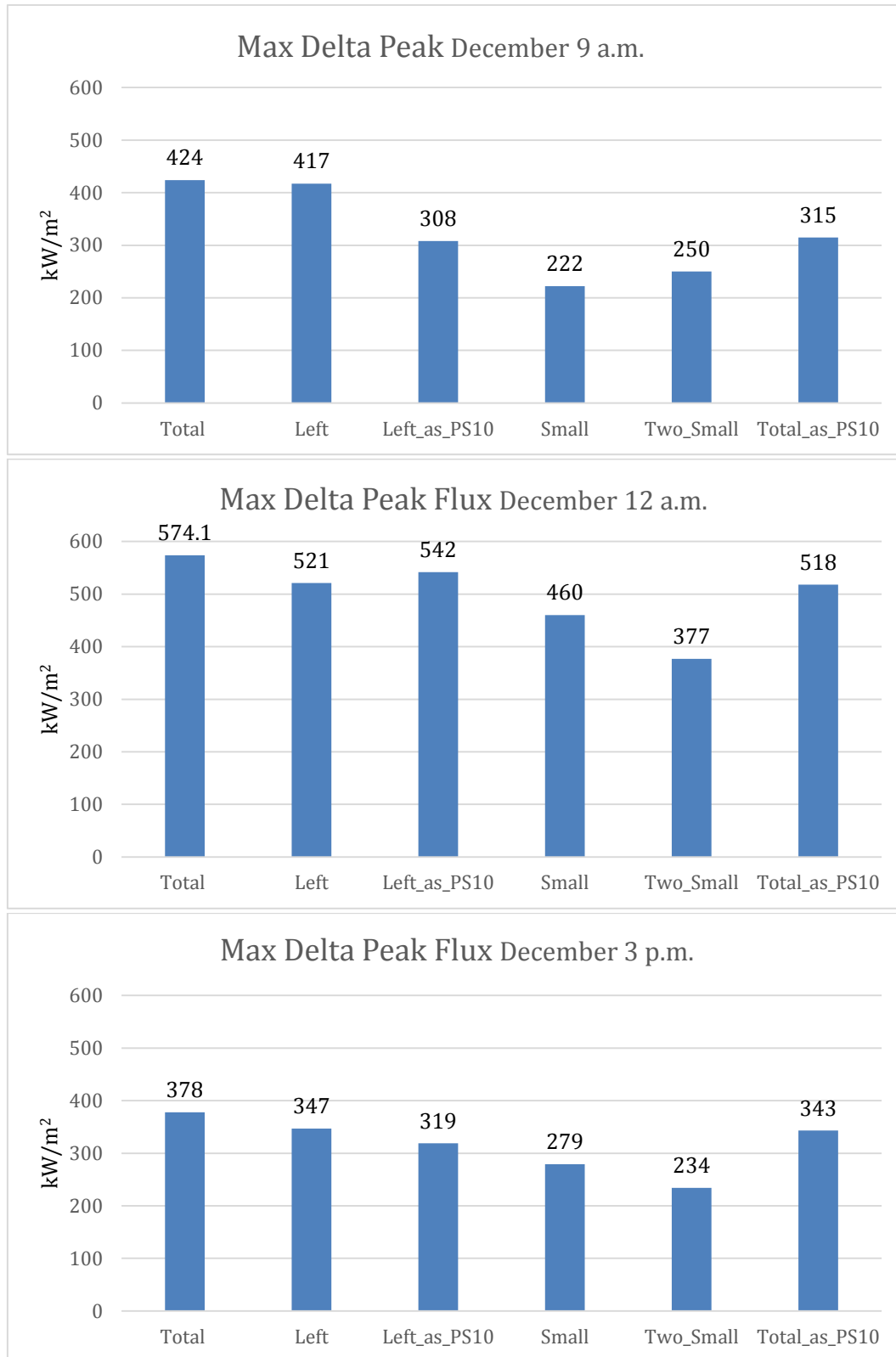


Figure 6. 20. Maximum delta peak flux value on 21th December, at 9 a.m., 12 a.m. and 3 p.m.

6.2.3 Selection of the best aiming

The criteria used to identify the best aiming strategy for Gemasolar working in transient conditions are the same used for PS10 and already described above. In figures 6.21, 6.22, 6.23 and 6.24 it is possible to observe the most relevant graphs, showing that the aiming strategy 6 continues to be the best one. Indeed, in the three types of graph, the selected best strategy is the one that shows the minimum values of peak flux, delta peak flux and maximum gradient. Moreover, the overall power does not decrease significantly in respect to the base case.

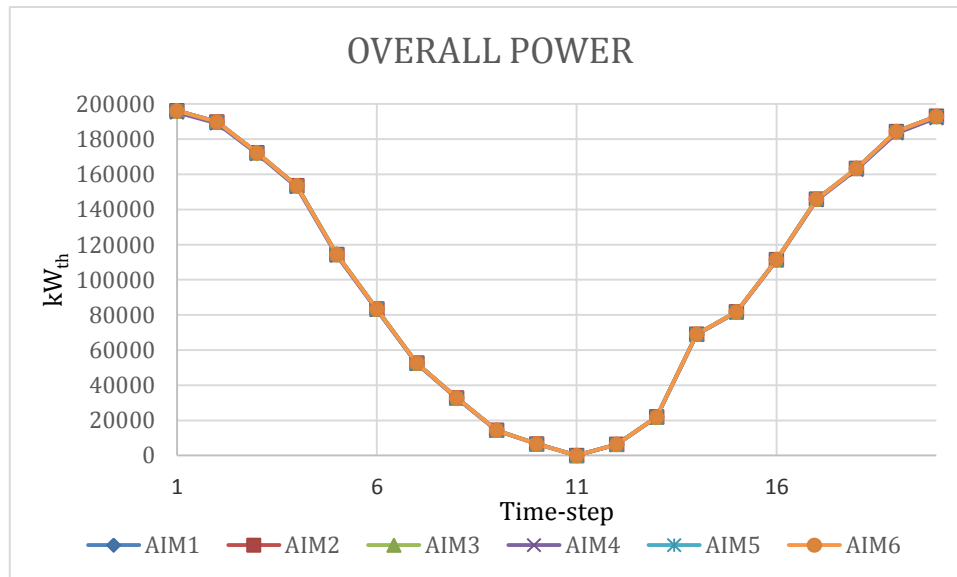


Figure 6. 21. Power variation of the incoming radiation as the cloud is passing over the field on 21th June at 3 p.m. in case of total shadow.

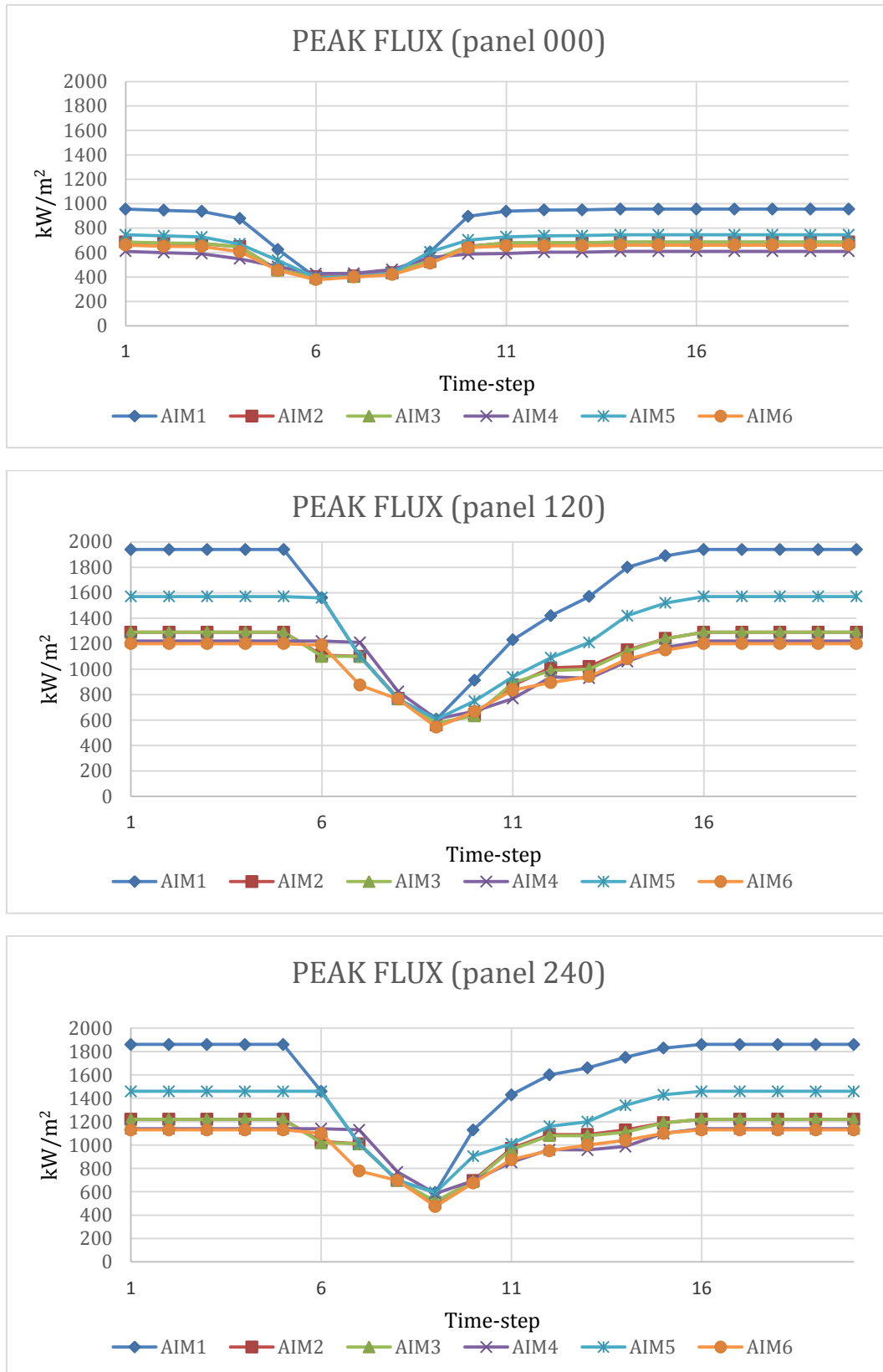


Figure 6. 22. Delta Peak Flux values for the three panels on 21th March, at 3 p.m., in case of total shadow as PS10.

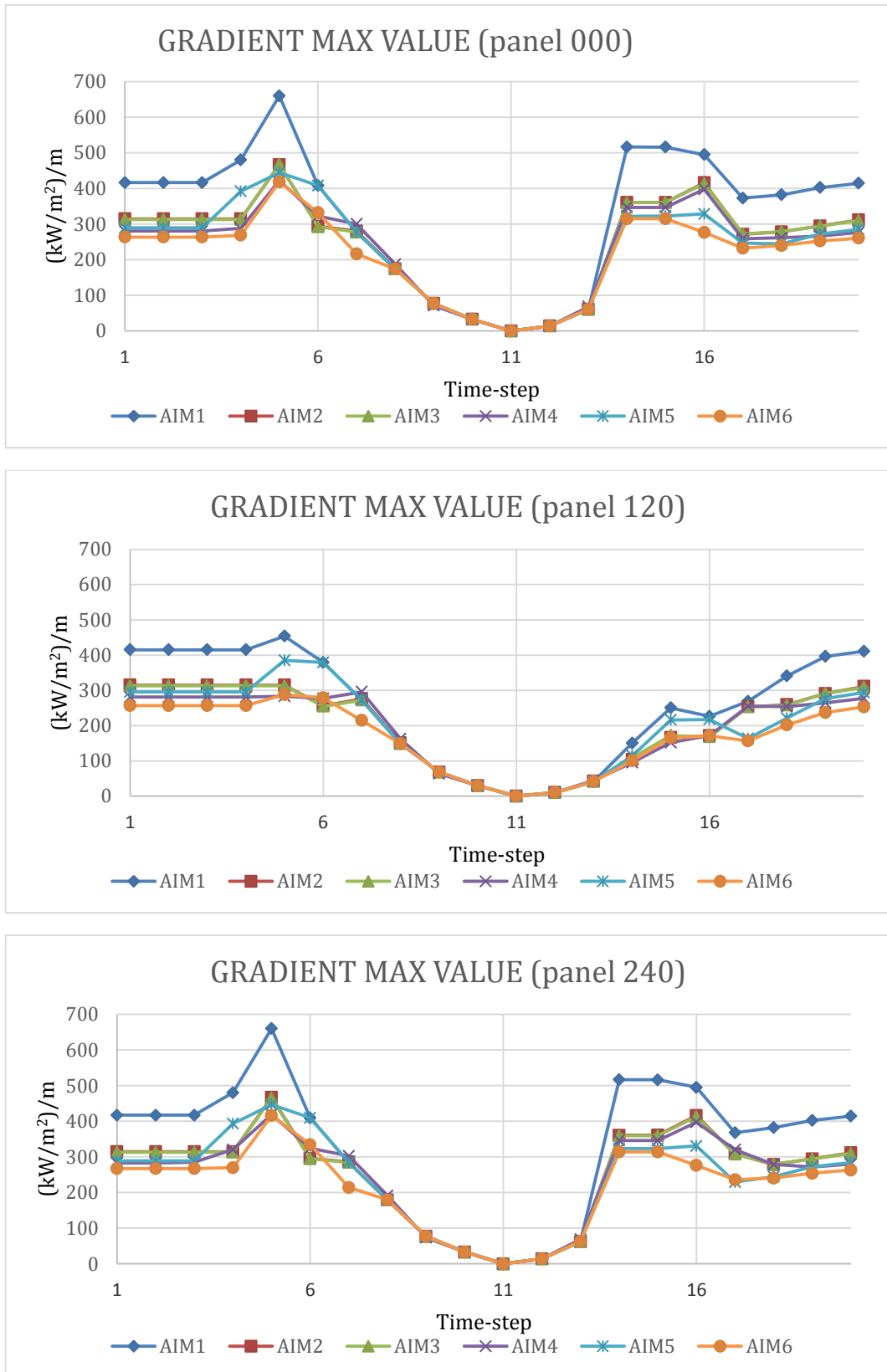


Figure 6. 23. Maximum Gradient values for the three panels on 21th June, at 3 p.m., in case of total shadow.

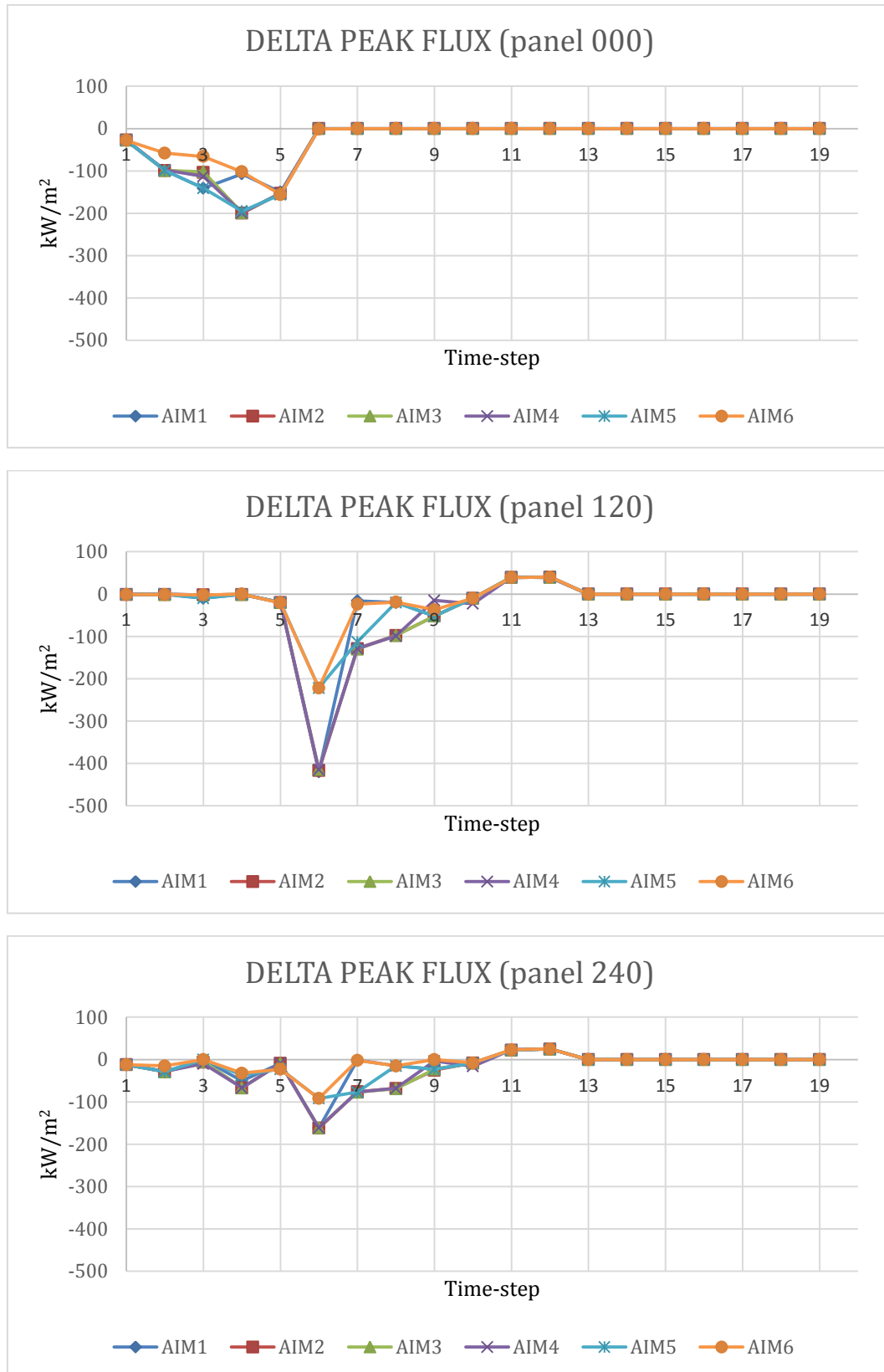


Figure 6. 24. Peak Flux values for the three panels on 21th December, at 9 a.m., in case of small cloud coming.

6.3 Numerical results of the Thermal model

From the results achieved with the first code, it has been possible to observe that the cloud that most affects the performance of the solar plant is the total cloud, and that the aiming strategy 6 results to be the best one, also in off-design conditions. In order to confirm these conclusions, a cross-check between different clouds and different strategies needs to be made. Firstly, assuming total cloud, the six aiming strategies are analyzed together and the results charted. In the figure 6.25, an overview of the thermal behavior of the panel 1e is provided, and the following observations can be made: the peak temperatures for the different strategies (a) nearly follow a common trend, but the number 6 presents lower values during almost the entire shadowing process; the same can be said about the temporal variation of the peak temperature (b): its absolute value should be as low as possible in order to avoid sudden changes of T that can lead to thermal stresses. Finally, the maximum gradient (c) presents dissimilarities for the different strategies, but the number 6 continues to have the best trend, with lower values of the gradient in almost every time step. The graphs correspondent to panels 1w and 2w show similar tendencies, which could directly lead to the conclusion that the aiming strategy 6 continues to be the better solution in off-design conditions, also considering the real thermal behavior. Nevertheless, as shown in figure 6.27, the trend of the maximum gradient for the panel 2e shows an incongruity: in the final time steps, the aiming strategy 2 presents values lower, with difference, than the other strategies. Although this result could be a proof against the primacy of the strategy 6, two circumstances have to be considered: firstly, the figure 6.27 presents almost the only coincidence in which the strategy 2 shows better performance, in the further ones the aiming 6 is the best one; secondly, as it can be observed in figure 6.26, using these two strategies similar efficiencies of the receiver are obtained, but higher values of the steam quality at the inlet of the steam drum (and of the steam mass flow) characterize the use of aiming strategy 6. In conclusion, the strategy number 6 finally shows a better thermal behavior during the passage of a total cloud almost for the entire receiver, and therefore continues to guarantee the best performance: for the time being, the results obtained in chapter 5 are confirmed. In order to explain the incongruity detected in figure 6.27, an analysis of the thermal mixed plots comparing strategies 2 and 6 is made in figure 6.31. The peak temperatures produced by strategy 2 are strongly higher than the strategy 6 ones, but the spatial distribution of the first presents more gradual and homogenous changes, especially in the horizontal direction: therefore, the temperature gradient obtained with strategy 2, and obviously its maximum value, have to be lower.

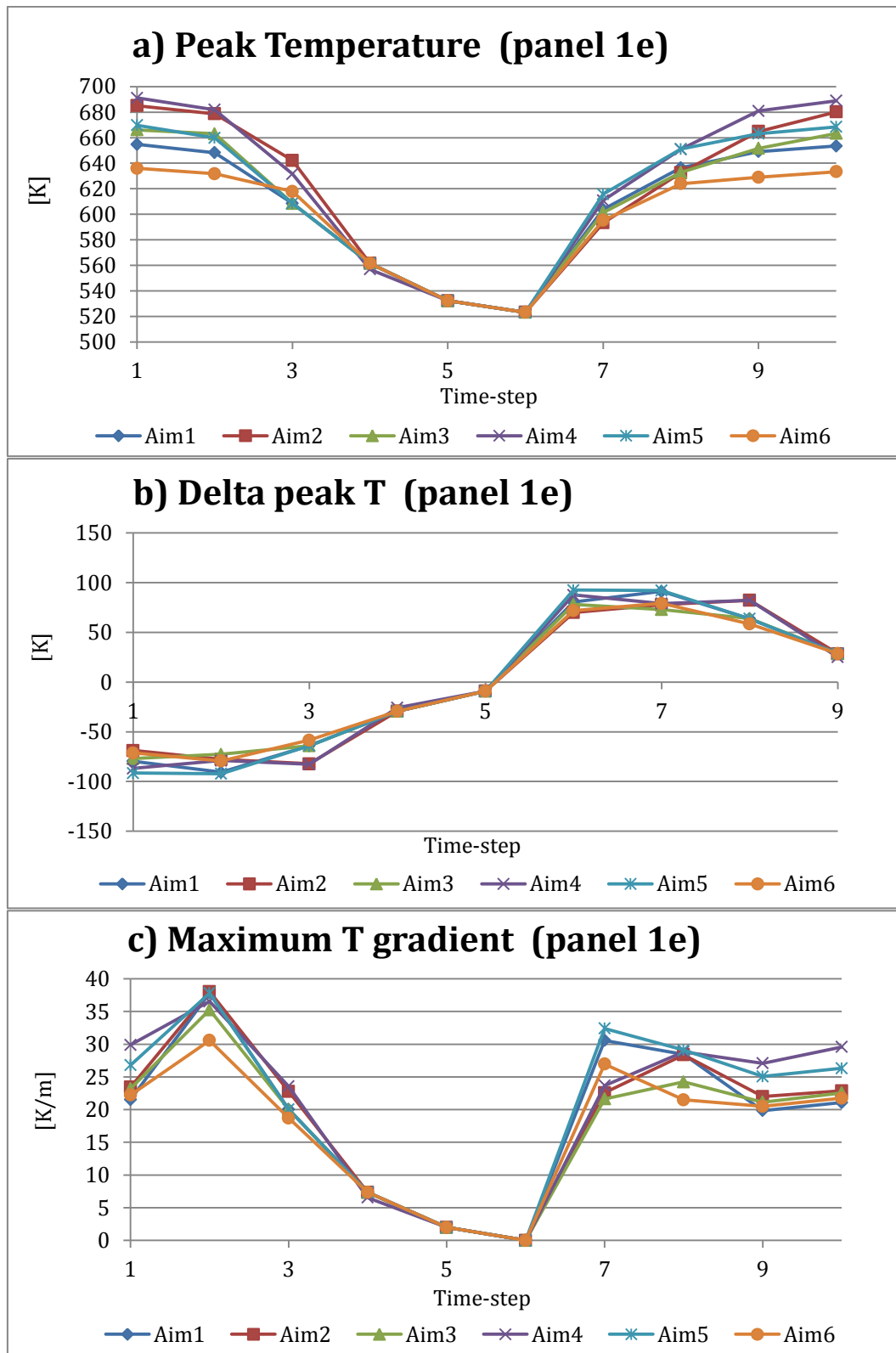


Figure 6. 25. Peak temperature, temporal variation of the peak temperature and maximum gradient (panel 1e) for the six aiming strategies during the passage of total cloud (21th June, 12a.m.).

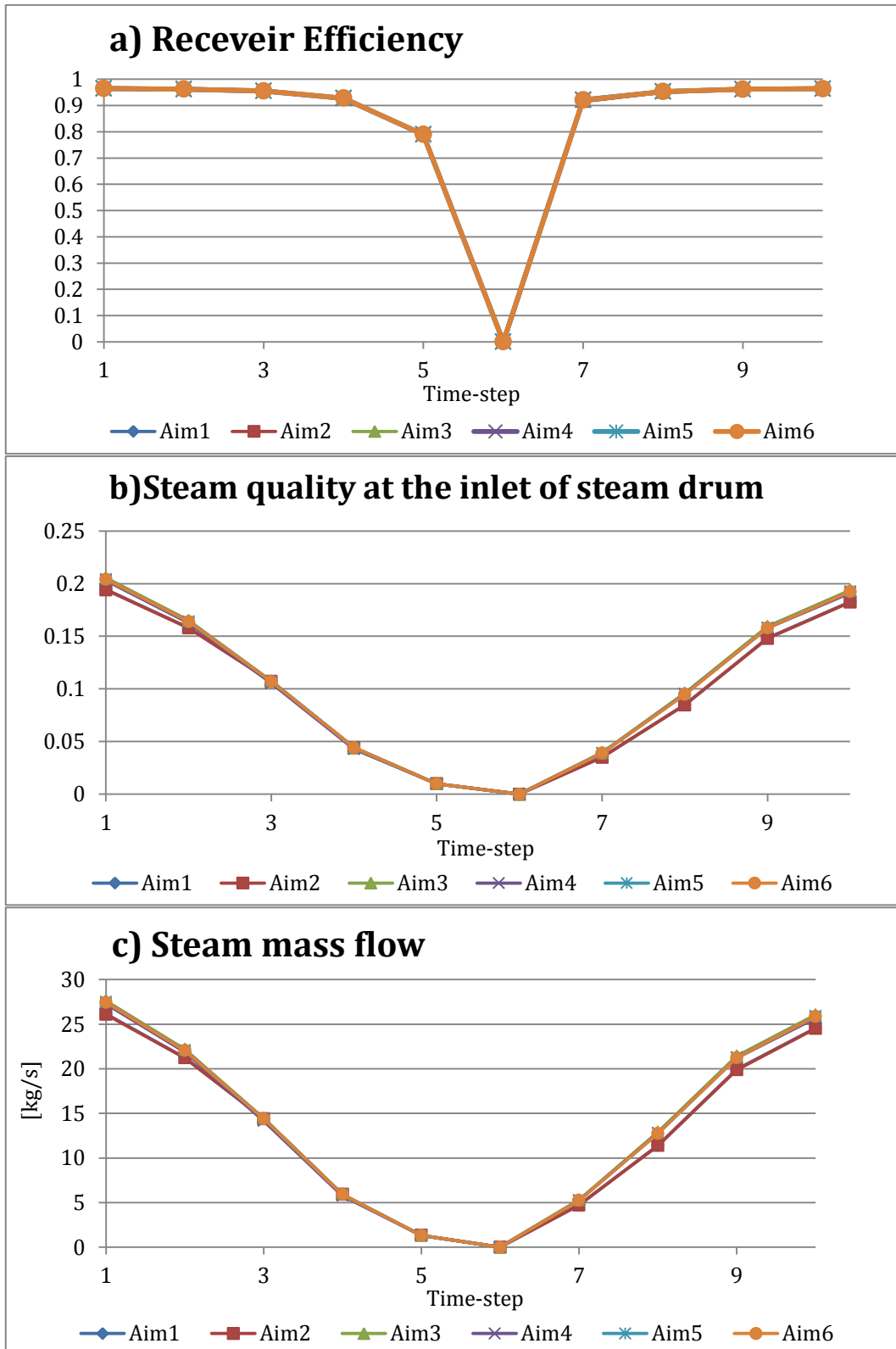


Figure 6. 26. Receiver efficiency, steam quality at the inlet of steam drum and steam mass flow for the six aiming strategies during the passage of a total cloud (21th June, 12 a.m.).

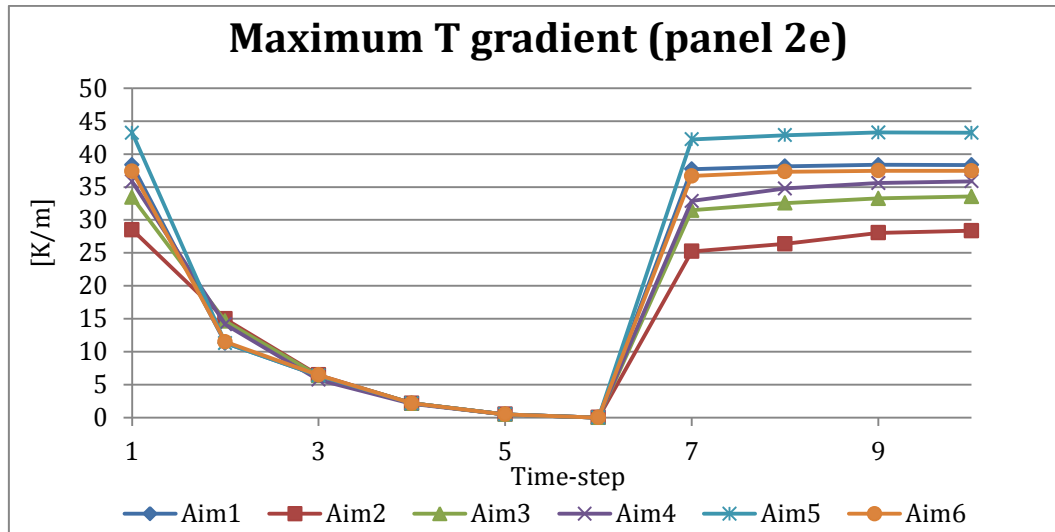


Figure 6. 27. Maximum Temperature gradient for the panel 2e for the six aiming strategies during the passage of a total cloud (21th June, 12 a.m.).

Afterwards, the validation of second stage of the cross-check is needed. In order to verify if the passage of a total cloud actually leads to the worst off-design condition studied, the six types of clouds are analyzed together, using the aiming strategy 6. Observing the figure 6.28, it seems clear that the two clouds that entail the worst performances of the receiver are the two total clouds: the efficiency, the steam quality and steam production are strongly reduced. The total cloud coming from south-east appears to be even worse in a few time-steps, but due to its low probability of appearance (see the wind profile in figure 2.2) the other total cloud can be considered as the worst one. Nevertheless, the study of thermal stresses of the receiver results to be more complicated. Observing the trends of the temporal variation of the peak temperature, the total cloud continues to be the worst one, globally speaking (figure 6.29; panel 1e is representative of the entire receiver); whereas considering the maximum gradient a univocal conclusion is not easily achievable. Looking at the figure 6.30, it is possible to observe the trends of the maximum gradient in the four panels. In the panels 2e and 2w the maximum gradients always stay below the on-design condition values, determined by the time-step 1. The two total clouds present a strong reduction of the maximum gradient, whereas the one of the small and the long cloud is almost constant. This does not result to be a problem, because it is due to way in which the clouds are covering the solar field, and does not entail additional thermal stresses for the receiver. Nonetheless, in the panels 1e and 1w the situation is different: maximum gradient values greater than the nominal one emerge, especially for the total cloud (panel 1e), the right cloud (panel 1e) and the long cloud (panel 1w). These circumstances could effectively produce additional stresses, which might be dangerous for the receiver itself.

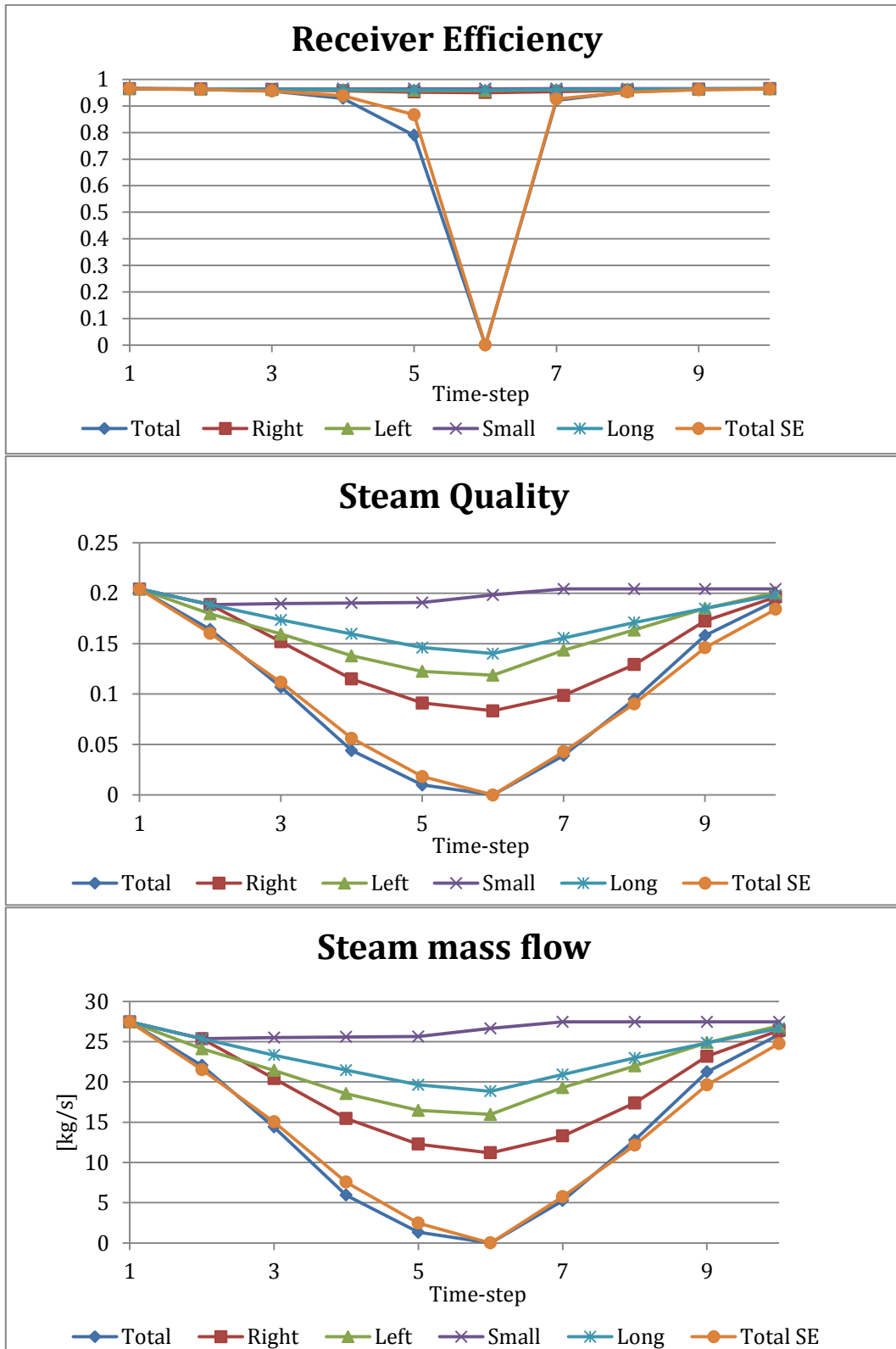


Figure 6. 28. Receiver efficiency, steam quality at the inlet of steam drum and steam mass flow for the aiming strategy 6 during the passage of the six clouds (21th June, 12 a.m.).

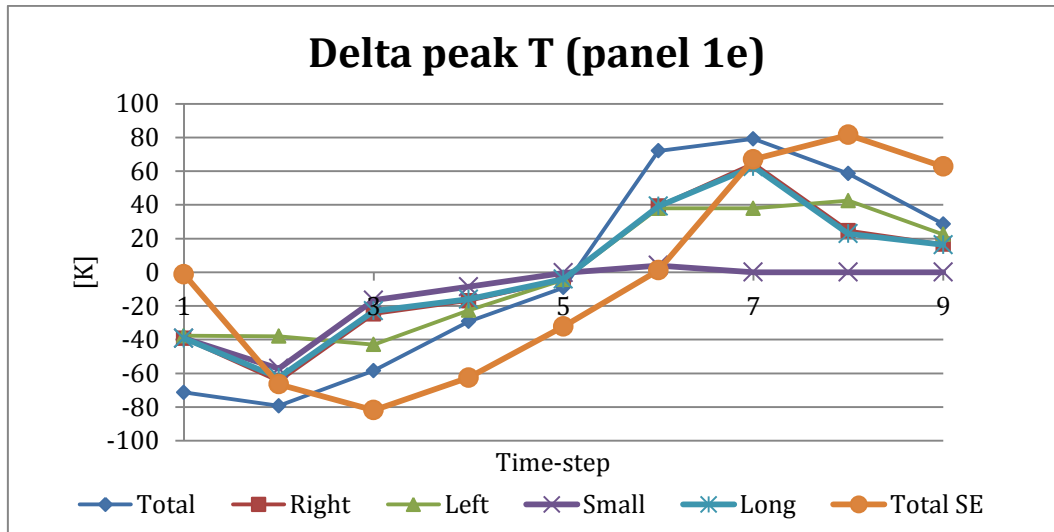


Figure 6. 29. Temporal variation of the peak temperature for the panel 1e, depending on the type of cloud, using aiming strategy 6 (21th June, 12 a.m.).

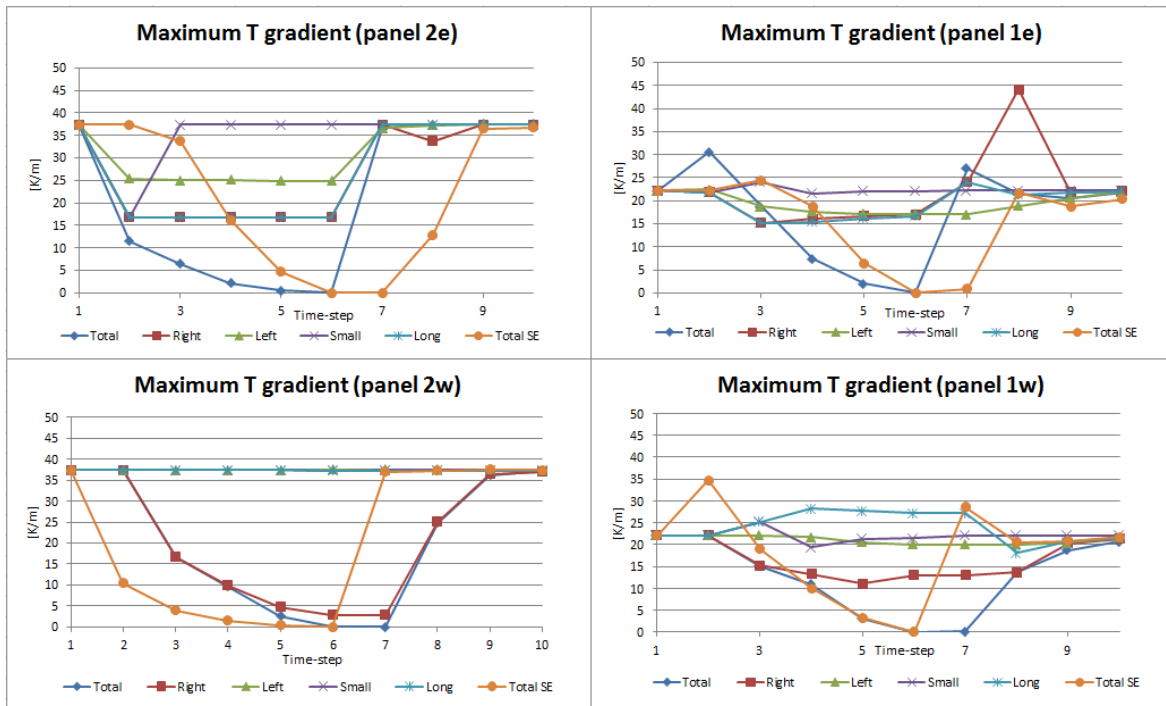


Figure 6. 30. Maximum temperature gradient for the four panels of the receiver, depending on the type of cloud, using aiming strategy 6 (21th June, 12a.m.).

A deeper study of the thermal stresses due to the temperature gradient would be recommended, in order to evaluate in particular the effects produced in the panel 1e by the passage of the Right Cloud. Nevertheless, in an overall scenario the Total Cloud continues to lead to the worst conditions studied, so the conclusions previously achieved are finally confirmed.

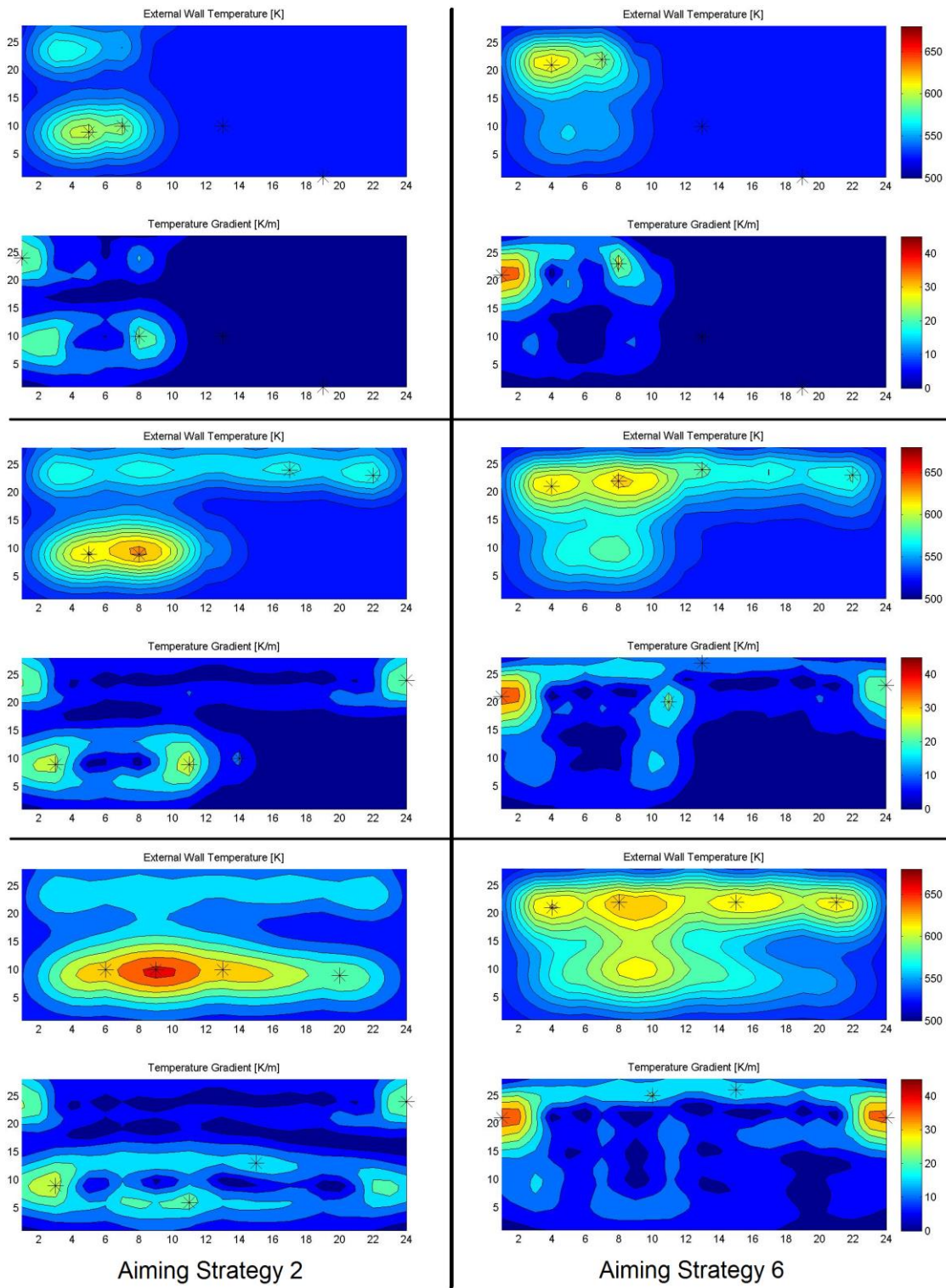


Figure 6. 31. Comparative analysis of the maximum temperature gradient in the panel 2e, during the final time-steps, using aiming strategies 2 and 6 (21th June, 12 a.m.).

Chapter 7

Future developments

The topic studied in this thesis is so wide that a great number of different issues could have been developed since the beginning. In this chapter are discussed all the subjects that are not being analyzed in this work for matter of time, and some hints are given for future works related to the optimization of solar power tower plants, in particular to the transient analysis of both optical and thermal aspects.

7.1 Software improvements

In chapter 4, a software able to simulate the optical behavior of the field of the PS10 and Gemasolar Solar Power plants has been developed and some slight modifications can improve its potentials:

- New aiming strategies approach

To increase the accuracy of the focusing process and to reduce some undesired effects, the choice of a different aiming strategy for each panel can be adopted. In the present version of the software, the field is divided in 4 sectors (3 for Gemasolar), each one aiming only to one panel (see figure 2.9). Nevertheless, the code only allows to set a global aiming strategy for the entire receiver: in other words, the 4 sectors are aiming to different panels, but with the same default pattern of pointing points (figure 2.8). A possible improvement would be separate the aiming strategy of each sector, making them independent from each other. In this way, it would be possible to edit new aiming strategies trying to solve punctual problems identified in already existing ones.

- Clouds characterization improvement

Clouds simulation can be further improved, mainly considering two aspects:

- Increase the discretization of the field subdividing the field in more zones, in order to have a more defined shape of the clouds and thus define a more precise trajectory of the latter. Moreover, increasing the number of time-steps, the accuracy of the simulation will increase.
- In this thesis, when a cloud passes over a mirror, the DNI sudden drops to zero. In reality, depending on its nature, a cloud leads to a variable reduction of DNI. For this reason, it is suggested to implement the code considering also the case in which a cloud reduces only partially the solar radiation. This increases for sure the precision of the simulation.

- New criteria for zone definition

The heliostats zone division defined in the program described in chapter 2 is based on a geometrical subdivision of the field and it does not take into account the difference in heliostats density. The zones layout results in a regular shape because only geometrical aspects are considered in sectors definition. To increase the accuracy of the aiming strategies, it is possible to develop a zone division based on the number of

heliostats in each zone. The present code shows a radial division characterized by 8 equally-spaced annuluses. A possible improvement would be to take into account variable radius-step values, which imply the increase of the size of the zones along with the distance from the tower. In this way, each zone will include the same number of mirrors allowing a better distribution of the heat flux on the receiver.

- Sensitivity analysis

As it is showed in chapter 5, PS10 and Gemasolar behave in a different way when their fields are covered by the same cloud. This is mainly due to the different sizes of the two plants, and therefore to the capacity of the cloud to completely shadow the high efficiency zones of the field. For this reason, it is important understand how a plant behaves in a cloudy day depending on its size, in order to facilitate the design phase for future plants. A sensitivity analysis could highlight the importance of the field size in off-design working conditions. This feature could be developed in the present code basically in two ways: by adding existing field layouts (for example the PS20 for the north fields or the Ivanpah for surrounding fields), or by creating new fields layout with specific software.

7.2 Thermal model improvements

In chapter 6, a simplified thermal model of the receiver of the PS10 is provided, to have a first view of the real thermal behavior of this component. In the following paragraphs, some hints are proposed in order to improve the accuracy of the model itself:

- Thermal losses

In paragraph 6.2.1, some of the minor thermal losses are not taken into account, such as the ones through tower interior and the one of forced convection due to the wind. A deep study of the contribution of these losses would probably improve the precision of the model.

- Receiver Geometry

Another possible upgrade could be done in the receiver geometry, especially for the layout of the pipes. In the present thermal model a simplified straight pipes layout is considered, but the study of the real pipes' configuration can be useful to comprehend the real thermal behavior of the receiver in off-design working conditions.

- Inertias and real transient conditions

The thermal model described in chapter 6 is a steady-state approximation of the transient behavior of a solar receiver. To increase the accuracy of the process, thermal inertias have to be modeled and the time dependence of each variable has to be included. Moreover, the insertion of the thermal model inside of a global code that consider the real behavior of the steam drum and the steam turbine will increase the precision of the simulation.

- Pressure drops and inlet conditions

Several other aspects could be taken into account to enhance the heat exchange simulation, for example pressure drops in receiver pipes and in the risers and down-comers pipes. The presence of these drops modifies the conditions at the inlet of the receiver, contradicting the assumption of saturated water, made in the present model. Therefore, a first improvement would be to consider subcooled water entering in the receiver, and consequently modify the thermal correlations used for the internal heat exchange process. Secondly, it is suggested to differentiate the water mass flow in each pipe, to better fit the considered flux map, enhancing the thermal performance.

- Thermal stresses evaluation

A program to compute heat flux maps and related thermal maps is been developed in this work. A step forward in the evaluation of the impact that a transient process has on a solar receiver, is to study the real thermal stresses produced. Thermal gradient values and local peak flux variations are not enough to appreciate the receiver response; a deep study on the material properties subjected to high temperatures has to be done and later implemented in the model.

Conclusions

The work presented in this thesis is the analysis of two commercial Solar Tower power plants (PS10 and Gemasolar) working in off-design conditions due to cloudy weather. The starting point was a previous thesis that analyzed different aiming strategies of the heliostats in normal working operation. The main result of this thesis was a strategy able to reduce the peak fluxes on the receiver, without a strong reduction of the overall thermal power. Therefore, the first aim of the present study was to verify if this aiming strategy was able to face off-design variable conditions. As a consequence, a group of possible clouds scenarios affecting the solar field was simulated, and a series of different aiming strategies was taken into account. A study of the different possible combinations showed which strategy was capable to provide a reduction of the parameters that most affect the premature ageing of the solar receiver. In order to do this, a great amount of simulations of the Solar Tower performance was required. Delsol3, software developed by Sandia National Laboratories, was chosen, and a Matlab interface was created to simplify the communication with it. In this section an analysis of peak values, maximum gradients and temporal variations of the incident heat flux was done, and it evidenced the primacy of a specific aiming strategy. The latter, called *Aiming Strategy 6*, showed positive behaviors in all the considered parameters. During the passage of a big cloud covering the entire solar field (worst off-design conditions), this strategy compared with the other ones gave the following results: 14÷33% reduction of the peak flux, 13÷19% reduction of the maximum gradient and 8.5÷28% reduction of the temporal variation of the peak flux. On the other hand, the overall thermal power was not reduced. These are average values, calculated on the entire covering/uncovering process: punctual aberrations could be observed, but they are only slightly significant and not able to modify the average trend.

Secondly, in order to confirm the results obtained in the first part of the work, a thermal model of the receiver of the PS10 was developed with Matlab. The aim of the code was to simulate the heat exchange process and to produce temperature maps of the external wall of the receiver, starting from the heat flux maps obtained in the first part. In this way, a study of the thermal stresses could be feasible. As previously done for the heat flux analysis, also the peak values, maximum gradients and temporal variations of the receiver temperature were studied. In order to verify the conclusions achieved with the first study, a cross-check between different clouds and aiming strategies was performed. Assuming the worst cloud condition, the behaviors of the six strategies were analyzed, and vice versa with the best aiming strategy and the different types of clouds. Once again *aiming strategy 6* showed the best performances: up to 8% reduction of the peak temperature, up to 35% of the maximum gradient and up to 29% of the temporal variation of the peak temperature. Therefore, this strategy was confirmed as the best available one, both in on-design and off-design operation. On the other hand, the study of thermal behavior of the receiver for the worst cloud condition resulted to be more difficult and it was not possible to achieve a completely univocal verdict. Observing the temporal variation of the temperature, the receiver efficiency and the production of steam, the big cloud covering the entire field (total cloud) explicitly led to the worst working conditions, but analyzing the trends of the maximum temperature gradients a few irregularities were found. Values above the nominal ones appeared during the passage of the total cloud itself, but also with other two types: a big cloud covering only the right half and a long cloud passing in the middle of it.

Nevertheless, globally speaking the total cloud could be confirmed as the worst cloud condition, due to its peculiarities and the relative slight importance of the detected aberrations. Finally, as a future proposal, a deeper study of the real thermal stresses is recommended, to better understand the true thermal behavior of the receiver and possibly the meaning of those incongruities.

Figures Index

Figure 1. 1. Concentrating solar collectors (adapted from [2]).	13
Figure 1. 2. Sun motion in the sky (azimuth-elevation angles variation) during a day, for solstices and equinoxes.	14
Figure 1. 3. Pressurized air cycles (adapted from [16])	15
Figure 1. 4. Atmospheric air-based cycle (Jülich solar tower, adapted from [19]).	15
Figure 1. 5. Molten salt cycle plant [21].	16
Figure 1. 6. Direct steam cycle plant (PS10, adapted from [23]).	16
Figure 1. 7. Steel lattice vs Concrete Tower. a) Ivanpah, b) Gemasolar.	17
Figure 1. 8. a) Cavity receiver, b) External receiver	18
Figure 1. 9. Map of Heliostat fields worldwide, with DNI (adapted from [24]).	19
Figure 1. 10. The cosine effect for two heliostats in opposite directions from the tower. Heliostat A in the north field has much greater cosine efficiency than heliostat B (at noon). [25].	21
Figure 1. 11. Shadowing and blocking loss [25].	22
Figure 1. 12. PS10 Solar Tower Power Plant.	23
Figure 1. 13. Gemasolar Solar Tower Power Plant.	24
Figure 2. 1. Clouds classification by altitude of occurrence, adapted from [28].	26
Figure 2. 2. Wind profile measured in the meteorological station of the Seville airport. This diagram takes into account both frequency distribution and Average wind intensity. Scale in percentage point compared to the maximum. [33].	27
Figure 2. 3. Evolution of the shadowing on the solar field for different clouds. From left to right respectively: total shadow S-W, right shadow, left shadow.	30
Figure 2. 4. Evolution of the shadowing on the solar field for different clouds. From left to right respectively: small shadow, long shadow, total shadow S-E.	31
Figure 2. 5. Evolution of the shadowing on the Gemasolar solar field for different clouds. From left to right respectively: total shadow S-W, left shadow, left shadow as PS10.	34
Figure 2. 6. Evolution of the shadowing on the Gemasolar solar field for different clouds. From left to right respectively: small cloud, two small clouds, total shadow as PS10.	35
Figure 2. 7. Zone division and numeration of the PS10 solar field.	36
Figure 2. 8. Representation of the aiming points of the panels of the receiver.	37
Figure 2. 9. Explication of the aiming distribution of the field.	37
Figure 2. 10. Visualization of influence of the azimuthal zone position in the field on the image position on the receiver [34].	38
Figure 2. 11. Visualization of influence of the radial zone position in the field on the image position on the receiver [34].	38
Figure 2. 12. Default aiming flux maps on the receiver of the PS10 on March 21st at noon. [34].	39
Figure 2. 13. Flux map on the receiver of the PS10, on March 21st at 12h, obtained with: a) aiming strategy 1, b) 2, c) 3, d) 4, e) 5 and f) 6.	41
Figure 2. 14. Results obtained with the traditional aiming (base) and the Aiming Strategies.	42
Figure 2. 15. Zone division and numeration of the Gemasolar solar field.	43

Figure 2. 16. Default aiming flux maps on the receiver of Gemasolar on March 21st at noon. [34].....	44
Figure 2. 17. Flux map on the receiver of Gemasolar, on March 21st at 12h, obtained with: a) aiming strategy 1, b) 2, c) 3, d) 4, e) 5 and f) 6.	46
Figure 2. 18. Results obtained with the traditional aiming (base) and the Aiming Strategies, for Gemasolar.....	47
Figure 2. 19. Trend of steels' strength as temperature changes.	47
Figure 3. 1. Extract from an input text file of Delsol.....	50
Figure 3. 2. Extract from an output text file of Delsol.	50
Figure 3. 3. Macros operation scheme.	52
Figure 3. 4. Main De Giorgi's GUI.	53
Figure 3. 5. GUI for input parameters modification.	54
Figure 3. 6. GUI for setting aiming strategy and field layout subdivision.....	55
Figure 3. 7. GUI for graphically display output.	56
Figure 4. 1. Principal interface of Solar Tool 5.....	59
Figure 4. 2. Image of the New Aiming Strategy GUI for PS10.	61
Figure 4. 3. Image of the New Aiming Strategy GUI for Gemasolar.	61
Figure 4. 4. Surf Map of the 7th time step of the passage of a big cloud covering only the right half of the solar field (aiming strategy 4, June 12h). The panel 2w is completely devoid of irradiance, the peak flux is located in the 1e.	63
Figure 4. 5. Contour Map of the same situation of figure 4.3. The different approach of the two graphs is perfectly understandable.	64
Figure 4. 6. Contour Map of the same situation of figure 4.4, except for the aiming strategy (here it is used the number 6).....	64
Figure 4. 7. Gradient Map of June 12h using the aiming strategy 5 in on-design conditions.	65
Figure 4. 8. Solar field by zones graph for the input path June 9h in on-design conditions.	66
Figure 4. 9. Extract from the output of Delsol.	66
Figure 4. 10. Solar field by heliostats graph for the input path June 9h in on-design conditions.....	67
Figure 4. 11. Mixed plot graph for the input path June 9h using aiming strategy 6 in on-design conditions.	68
Figure 5. 1. Flow regime and heat exchange coefficient for a forced convection boiling flow in a pipe.....	70
Figure 5. 2. Vertical pipes layout used in the thermal model.....	71
Figure 5. 3. External thermal losses for the PS10 cavity receiver.	72
Figure 5. 4. Thermal balance in a single flux unit. In the representation only 4 of the 14 pipes are represented, in order not to overload the figure.....	73
Figure 5. 5. Electric analogy of the heat transfer process.	76
Figure 5. 6. External wall temperature surf map (21th June, 12 a.m., aiming strategy 6)..	79
Figure 5. 7. Thermal mixed plot graph at same conditions of figure 5.6.	79
Figure 5. 8. Steam quality graph at same conditions of figure 5.6.....	80
Figure 6. 1. Solar field by heliostats graph for September and March at 9h, 12h and 15h.	82
Figure 6. 2.Solar field by heliostats graph for June at 9h, 12h and 15h.....	83

Figure 6. 3. Solar field by zones graph for March at 9h, 12h and 15h.	84
Figure 6. 4. Move of Peak Flux during the covering of the field (Jun 9 a.m., aiming strategy 6, Mixed plot graph)	85
Figure 6. 5. Trend of the peak flux for the panel 2e during the passage of a big cloud covering the entire the solar field (March 12h)....	86
Figure 6. 6. Representation of the change of the flux map during the passage of a big cloud covering the entire solar field for the same situation described in figure 6.7, using strategy 6.	87
Figure 6. 7. Trend of the Punctual variation of the heat flux for the same situation described in figure 6.5.	88
Figure 6. 8. Trend of the Maximum Gradient for the same situation described in figure 6.5.	88
Figure 6. 9. Trend of the Overall Power during the passage of a big cloud covering the entire solar field (June 12h).....	89
Figure 6. 10. Maximum delta peak flux value on 21th June, at 9 a.m., 12 a.m. and 3 p.m., using aiming strategy 6.	90
Figure 6. 11. Maximum delta peak flux value on 21th December, at 9 a.m., 12 a.m. and 3 p.m., using aiming strategy 6.	91
Figure 6. 12. Peak Flux, Delta Peak Flux and Maximum Gradient values of panel 1w on 21th June, at noon, in case of total shadow.	93
Figure 6. 13. Peak Flux, Delta Peak Flux and Maximum Gradient values of panel 1w on 21th June, at 3 p.m., in case of a big cloud covering only the right half of the field. ..	94
Figure 6. 14. Peak Flux, Delta Peak Flux and Maximum Gradient values of panel 1e on 21th December, at 3 p.m., in case of small cloud.	95
Figure 6. 15. Solar field by heliostats graph for different hours and inputs.	97
Figure 6. 16. Representation of the different contributes of the heliostats efficiency (21th December, 9 a.m.). Letters refer to the previous page.	99
Figure 6. 17. Solar field by zones graph for 21th June, at 9 a.m., 12a.m. and 3 p.m.	100
Figure 6. 18. Move of Peak Flux during the covering of the field (March 12 a.m., aiming strategy 6, Mixed plot graph)	101
Figure 6. 19. Maximum delta peak flux value on 21th June, at 9 a.m., 12 a.m. and 3 p.m.	103
Figure 6. 20. Maximum delta peak flux value on 21th December, at 9 a.m., 12 a.m. and 3 p.m.	104
Figure 6. 21. Power variation of the incoming radiation as the cloud is passing over the field on 21th June at 3 p.m. in case of total shadow.	105
Figure 6. 22. Delta Peak Flux values for the three panels on 21th March, at 3 p.m., in case of total shadow as PS10.	106
Figure 6. 23. Maximum Gradient values for the three panels on 21th June, at 3 p.m., in case of total shadow.	107
Figure 6. 24. Peak Flux values for the three panels on 21th December, at 9 a.m., in case of small cloud coming.	108
Figure 6. 25. Peak temperature, temporal variation of the peak temperature and maximum gradient (panel 1e) for the six aiming strategies during the passage of total cloud (21th June, 12a.m.).	110

Figure 6. 26. Receiver efficiency, steam quality at the inlet of steam drum and steam mass flow for the six aiming strategies during the passage of a total cloud (21th June, 12 a.m.).	111
Figure 6. 27. Maximum Temperature gradient for the panel 2e for the six aiming strategies during the passage of a total cloud (21th June, 12 a.m.).	112
Figure 6. 28. Receiver efficiency, steam quality at the inlet of steam drum and steam mass flow for the aiming strategy 6 during the passage of the six clouds (21th June, 12 a.m.).	113
Figure 6. 29. Temporal variation of the peak temperature for the panel 1e, depending on the type of cloud, using aiming strategy 6 (21th June, 12 a.m.).	114
Figure 6. 30. Maximum temperature gradient for the four panels of the receiver, depending on the type of cloud, using aiming strategy 6 (21th June, 12a.m.).	114
Figure 6. 31. Comparative analysis of the maximum temperature gradient in the panel 2e, during the final time-steps, using aiming strategies 2 and 6 (21th June, 12 a.m.).	115

Tables Index

Table 1. 1. Concentrating solar collectors (adapted from [6]).....	13
Table 2. 1. Resume of the 6 aiming strategies. The row 1 contains the zones from 1 to 8, the row 2 from 9 to 16 and so on.....	40
Table 2. 2. Resume of the 6 aiming strategies for Gemasolar. The row 1 contains the zones from 1 to 8, the row 2 from 9 to 16 and so on.....	45
Table 4. 1. Resume of UDAY and UTIME parameters for the different inputs	60
Table 5. 1. Values of the steam quality for different mass flows, using a standard size of pipe. Input used: June 12 a.m., aiming strategy 6.	70
Table 5. 2. Thermo-phsycal properties of air at $T_f=440.17$ K.	75
Table 5. 3. Some constants taken into account in the thermal model.....	777
Table 6. 1. Resume of the efficiencies of the field for different days, at noon.	96

Nomenclature and acronyms index

In order of appearance:

DNI	Direct Normal Irradiance	[J/m ²]
O&M	Operation and Maintenance	[-]
λ	Wavelength	[m]
CSP	Concentrating Solar Power	[-]
A_C	Collecting Area	[-]
A_A	Absorbing Area	[-]
C_R	Concentration Ratio	[-]
STE	solar thermal electricity	[-]
PDC	parabolic dish collectors	[-]
LFC	linear Fresnel collectors	[-]
CRS	central tower systems	[-]
PTC	parabolic trough collectors	[-]
DoE	U.S. Department of Energy	[-]
LEC	Levelized Energy Cost	[-]
USA	United States of America	[-]
W-E	West-East direction	[-]
S-N	South-North direction	[-]
S-E	South-East direction	[-]
S-W	South-west direction	[-]
$v_{w(H)}$	Wind velocity at the height “H”	[m/s]
H	Height	[m]
v_{10}	Wind velocity at 10 meters	[m/s]
a	Hellman exponent	[-]
ε_i	Thermal strain	[-]
α	Coefficient of thermal expansion	[K ⁻¹]
T	Temperature	[K]
RTS	Resistance to thermal shock	[W/m]
σ_r	Thermal stress	[N/m ²]
E	Young’s modulus	[N/m ²]
k	Thermal conductivity	[W/mK]
VBA	Visual basic for applications	[-]
GUI	Graphical User Interface	[-]
ISO	International Organization for Standardization	[-]
DN	Nominal Diameter	[-]
x_s	Steam quality	[-]
A_{ij}	Area of a flux unit	[m ²]
A	Area of the entire receiver	[m ²]
A_{pipe}	Section of the pipe	[m ²]
q	Thermal flux	[W]
σ	Stefan-Boltzmann constant	[W/m ² K ⁴]
ε	Emissivity	[-]
ρ	Reflectivity	[-]
F	View Factor	[-]
h	Heat transfer coefficient	[W/(m ² K)]

Nu	Nusselt number	[-]
Re	Reynolds number	[-]
Pr	Prandtl number	[-]
Ra	Rayleigh number	[-]
Gr	Grashof number	[-]
L	Characteristic length	[m]
g	Gravitational acceleration	[m/s ²]
ρ_{air}	Air Volumetric mass density	[kg/m ³]
ρ_s	Steam Volumetric mass density	[kg/m ³]
ρ_l	Saturated liquid Volumetric mass density	[kg/m ³]
Δh_{lv}	Enthalpy of vaporization	[J/kg]
μ	Dynamic viscosity	[Pa*s]
ν	Kinematic viscosity	[m ² /s]
c_p	Specific heat at constant pressure	[J/kgK]
\bar{T}_f	Mean film temperature	[K]
β	Volumetric thermal expansion coefficient	[K ⁻¹]
U	Overall heat transfer coefficient	[W/m ² K]
R	Thermal resistance	[m ² K/W]
r	Radius	[m]
D	Diameter	[m]
Co	Convection number	[-]
Bo	Boiling number	[-]
C_1, C_2, C_3, C_4	Kandlikar correlation coefficients	[-]
\dot{m}	Mass flow	[kg/s]

Sub-indexes:

L	Characteristic length
s	Steam
l	Saturated liquid
sat	Saturation conditions
wallExt	External wall
sky-ground	Mean sky-ground
conv	Convective
cond	Conductive
rad	Radiative
air	Air
f	Film
∞	Free stream
steel	Steel
ext	External
int	Internal
amb	Ambient condition
loss	Losses
refl	Reflection
trans	Transmitted

References

- [1] IRENA, «Renewable Technologies: Cost Analysis Series - Concentrating Solar Power. Technical Report 2, International Renewable Energy Agency,» C67 Office Building, Khanlidayah (32nd) street. P.O. 236, Abu Dhabi, Unites Arab Emirates, 2012.
- [2] SolarPACES, «Concentrating Solar Power - Global Outlook 09 - Why Renewale Energy is Hot. Technical report,» SolarPACES, 2009.
- [3] G. Kolb, D. Alpert e C. Lopez, «Insights from the operation of Solar One and their implications for future central receiver plants.,» *Solar Energy*,, p. 47(1):39–47., 1991.
- [4] NREL, «SunShot Vision Study.,» Technical Report February, National Renewable Energy Laboratory, U.S. Department of Energy, Office of Energy Efficiency and Renewable Energy., 2012.
- [5] G. Augsburger, «Thermo-economic optimisation of large solar tower power plants,» *PHD thesis from ÉCOLE POLYTECHNIQUE FÉDÉRALE DE LAUSANNE*, 2013.
- [6] K. S., «Solar Energy Engineering - Processes and Systems.,» *Academic Press*, 2009.
- [7] Solugas, « Solar Up-scale Gas Turbine System.,» 2012.
- [8] DLR, « Concentrating Solar Power for the Mediterranean Region,» Technical report, Systems Analysis and Technology Assessment, Institute of Technical Thermodynamics, Deutsches Zentrum für Luft- und Raumfahrt e.V. (DLR), Pfaffenwaldring 38-40, D-70569 Stuttgart, Germany., 2005.
- [9] Torresol, « Gemasolar, the world’s first solar thermal plant consisting of central tower technology and salts receiver,» Technical report, Torresol Energy Investments,, S.A., A4 p.k. 475, 41420 Fuentes de Andalucía, Seville - Spain., 2011.
- [10] Abengoa, «PS10, the first solar power tower worldwide report, Abengoa Solar,» Technical, S.A., C/ de la Energía Solar, Palmas Altas, 41014 - Sevilla., 2007.
- [11] Abengoa, «PS20, the largest solar power tower worldwide,» Technical report, Abengoa Solar, S.A., C/ de la Energía Solar, Palmas Altas, 41014 - Sevilla., 2009.
- [12] ESolar, « Sierra SunTower,» Technical report, Inc., 3355 W. Empire, eSolar Avenue, Suite 200, Burbank, CA 91504., 2009.
- [13] BrightSource, «Coalinga Chevron/BrightSource Solar-to-Steam Demonstration Facility,» Technical report, BrightSource Energy, 1999 Harrison Street, Suite 2150, Oakland, CA 94612., 2011.
- [14] R. Buck, T. Bräuning, T. Denk, M. Pfänder, P. Schwarzbözl e F. and Tellez, « Solar-Hybrid Gas Turbine-based Power Tower Systems (REFOS),» *Journal of Solar Energy Engineering*, p.

124(1):2., 2002.

- [15] T. Strand, J. Spelling, L. R. K. Nilsson e H. Hansson, «An Innovative Hybrid Solar Gas-Turbine Power Plant Based on the Topcycle Concept,» in *In Submission to the Proceedings of the SolarPACES 2012 Conference on Concentrating Solar Power and Chemical Energy Systems*, Marrakesh, Morocco., 2012.
- [16] P. Poživil, V. Aga, A. Zagorskiy e A. Steinfeld, «A pressurized air receiver for solar-driven gas turbines,» *SolarPACES*, 2013.
- [17] B. Hoffschmidt, F. Téllez, A. Valverde e J. Fernandez, « Performance Evaluation of the 200-kW[sub th] HiTRec-II Open Volumetric Air Receiver,» *Journal of Solar Energy Engineering*, p. 125(1):87., 2003.
- [18] H. Singh, R. Saini e J. Saini, « A review on packed bed solar energy storage systems,» *Renewable and Sustainable Energy Reviews*, p. 14(3):1059–1069., 2010.
- [19] DLR, « Der Solarturm Jülich,» Technical report Deutsches Zentrum für Luft und Raumfahrt, Institut für Solarforschung, Linder Höhe, 51147 Köln..
- [20] J. W. Raade, B. Elkin e J. Vaughn, « Novel 700 °C Molten Salt for Solar Thermal Power Generation with Supercritical Steam Turbines.,» in *In Submission to the Proceedings of the SolarPACES 2012 Conference on Concentrating Solar Power and Chemical Energy Systems*, volume 001, Marrakesh, Morocco..
- [21] J. Ignacio, J. Burgaleta e M. Félix, «Central Receiver System Solar Power Plant Using Molten Salt as Heat Transfer Fluid,» *Journal of Solar Energy Engineering*, 2008.
- [22] A. Garmendia, R. Gilaberte, J. B. Jiménez e M. Méndez, « Description of Abengoa Solar Tower Solution with Superheated Steam Technology.,» in *In Submission to the Proceedings of the SolarPACES 2012 Conference on Concentrating Solar Power and Chemical Energy Systems*, Marrakesh, Morocco, 2012.
- [23] Solúcar, «10 MW Solar Thermal Power Plant for Southern Spain,» Technical Report November 2006, 2005.
- [24] Solargis, GeoModelSolar, world map of direct normal irradiation, <http://solargis.info>, 2014.
- [25] PowerFromTheSun, «The cosine effect for two heliostats in opposite directions from the tower,» available: *Powerfromthesun.net*, [on line].
- [26] E. commission, «Concentrating solar power from research to implementation,» in available: *ec.europa.eu.*, [on line].
- [27] R. Penrose, «Meteorology at the Millennium,» *Academic Press*, 2002.
- [28] E. Britannica, Different types of clouds form at different heights, 2012.
- [29] T. Teolan e H. Maire, «Dynamic properties of clouds Cumulus humilis and Cumulus fractus

- extracted by solar radiation Measurements,» *Springer*, 2011.
- [30] B. Timothy e C. Judith, «Characteristics of small tropical cumulus clouds and their impact on the environment,» *Journal of Geophysical Research*, vol. 103, pp. 28,753-28,767, 1998.
- [31] K. Hisashi, «The Horizontal Movement Speed of Cumulus Clouds in a Shear Flow: A Two-Dimensional Numerical Experiment,» *Hokkaido University*, 1981.
- [32] V. m. Manuel, «Análisis de las direcciones de los vientos en Andalucía,» *Nimbus*, n. 1, pp. 153-168, 1998.
- [33] Wind profile chart, available : aviador.es, [on line].
- [34] P. De Giorgi, «Software analysis and development for aiming strategies optimization in Solar Tower power plants,» *Master Thesis in Energy Engineering, Politecnico di Milano*, 2014.
- [35] K. Clifford, «Software and Codes for Analysis of Concentrating Solar Power Technologies,» SANDIA NATIONAL LABORATORIES, 2008.
- [36] B. L. Kistler, «A User's Manual for DELSOL3: A Computer Code for Calculating the Optical Performance and Optimal System Design for Solar Thermal Central Receiver Plants,» 1986.
- [37] X. Py, N. Calvet, R. Olives e P. echegut, «THERMAL STORAGE FOR SOLAR POWER PLANTS BASED ON LOW COST RECYCLED MATERIAL,» 2008.
- [38] F. Colzi e S. Petrucci, «Modeling On/Off – Design performance of solar tower plants,» *Master Thesis, Politecnico di Milano*, 2009.
- [39] Standard Chart 'Steel Pipe Sizes, Weight, Dimension', available: allsteelpipe.com, [on line].
- [40] K. Gregory, H. Clifford, M. Thomas e G. Jesse, «Power Tower Technology Roadmap and Cost Reduction Plan,» SANDIA REPORT , Albuquerque, New Mexico 87185 and Livermore, California 94550 , 2011.
- [41] PowerFromTheSun, Cavity Receiver, view factors, available: powerfromthesun.net, [on line].
- [42] Incropera, DeWitt, Bergman e Lavine, *Fundamentals of Heat and Mass Transfer*, Sixth Edition, 2006.
- [43] L. P. Colombo, Lessons slides on Flow Boiling, Politecnico di Milano, 2012.
- [44] G. Petrucci, «Proprietà dei materiali e prove meccaniche,» in *lezioni di costruzione di macchina*, Università degli Studi di Palermo.

